A STUDY OF CLOUDS USING SATELLITE RADIANCE DATA IN COMPARISON WITH RAINGAGE NETWORK AND RADAR OBSERVATIONS

LP-140

Prepared by:

GERALD M. JURICA AND SHIH-CHENG CHAO
ATMOSPHERIC SCIENCE GROUP
TEXAS TECH UNIVERSITY
LUBBOCK, TEXAS

TECHNICAL REPORT STANDARD TITLE PAGE

1. REPORT NO.	2. GOVERNMENT ACCESSION NO.	3. RECIPIENT'S CATALOG NO.

4. TITLE AND SUBTITLE	5. REPORT DATE
A Study of Clouds Using Satellite Radiance Data in Comparison with Rain-gage Network and Radar Observations	October, 1980
	6. PERFORMING ORGANIZATION CODE
	580/330

7. AUTHOR(S)	8. PERFORMING ORGANIZATION REPORT NO.
Gerald M. Jurica and Shih-Cheng Chao	

9. PERFORMING ORGANIZATION NAME AND ADDRESS	10. WORK UNIT NO.
Texas Department of Water Resources P. O. Box 13087 Capitol Station Austin, Texas 78711	5540
	11. CONTRACT OR GRANT NO.
	IAC(80-81)0890
	13. TYPE OF REPORT AND PERIOD COVERED

12. SPONSORING AGENCY NAME AND ADDRESS	13. TYPE OF REPORT AND PERIOD COVERED
Office of Atmospheric Resources Research Water and Power Resources Service Building 67, Denver Federal Center Denver, Colorado 80225	Technical 1 January 1980 to 30 September 1980
	14. SPONSORING AGENCY CODE

15. SUPPLEMENTARY NOTES

16. ABSTRACT The objective of this study is to use GOES visible and infrared radiance data to determine cloud characteristics, including cloud population, albedo, cloud-top temperature and height, as well as the changes of cloud parameters with time. Verification of the satellite-derived results is achieved by comparison with corresponding raingage network measurements and radar observations. Four cases have been chosen during the 1977 Texas HIPLEX field season.

In the first portion of this study, visible radiance data are used to determine cloud populations, percent cloud cover and cloud albedos, with cloud-top temperatures computed from the infrared data.

The second portion compares the results derived from satellite data with raingage and radar data. Precipitation analyses indicate that two case study days had heavy rain, but the others had little or none. Synoptic, subsynoptic, and small-scale features were investigated to determine the mechanisms of precipitation; on 22 June a squall line, a subsynoptic feature, and on 8 July a cold front, a synoptic feature, triggered the development of a line of convective clouds which produced the observed precipitation.

17. KEY WORDS AND DOCUMENT ANALYSIS

a. DESCRIPTORS--
Weather modification/ convective clouds/ geostationary satellite/meteorological radar/ raingages/precipitation/cloud seeding.

b. IDENTIFIERS-- Texas/High Plains/HIPLEX

c. COSATI Field/Group   COWRR:

18. DISTRIBUTION STATEMENT	19. SECURITY CLASS (THIS REPORT)	21. NO. OF PAGES
Available from the National Technical Information Service. Operations Division. Springfield. Virginia 22161.	UNCLASSIFIED	
	20. SECURITY CLASS (THIS PAGE)	22. PRICE
	UNCLASSIFIED	

A STUDY OF CLOUDS USING SATELLITE RADIANCE DATA

IN COMPARISON WITH

RAINGAGE NETWORK AND RADAR OBSERVATIONS

Gerald M. Jurica
and
Shih-Cheng Chao

Atmospheric Science Group
Texas Tech University
P. O. Box 4320
Lubbock, Texas   79409

January 1981

.

ABSTRACT

The objective of this study is to use GOES visible and
infrared radiance data to determine cloud characteristics,
including cloud population, albedo, cloud-top temperature and
height, as well as the changes of cloud parameters with time.
Verification of the satellite-derived results is achieved by
comparison with corresponding raingage network measurements
and radar observations. Four cases have been chosen during
the 1977 Texas HIPLEX field season.

In the first portion of this study, visible radiance data
are used to determine cloud populations, percent cloud cover
and cloud albedos, with cloud-top temperatures computed from
the infrared data.

The second portion compares the results derived from
satellite data with raingage and radar data. Precipitation
analyses indicate that two case study days had heavy rain,
but the others had little or none. Synoptic, subsynoptic,
and small-scale features were investigated to determine the
mechanisms of precipitation; on 22 June a squall line, a sub-
synoptic feature, and on 8 July a cold front, a synoptic
feature, triggered the development of a line of convective
clouds which produced the observed precipitation.

TABLE OF CONTENTS

LIST OF TABLES

LIST OF FIGURES

vii

ix

CHAPTER 1

INTRODUCTION

The objective of this study is to employ Geostationary Operational Environmental Satellite (GOES) visible and infrared radiance data to determine cloud characteristics, including cloud population, albedo, cloud top temperature and height, as well as the changes of cloud parameters with time. Verification of the satellite-derived results has been achieved by comparing with the corresponding raingage network measurement and observations by radar.

1.1 Historical Background

The successful launch of TIROS I and subsequent meteorological satellites has made it possible to monitor weather conditions from space on a regular basis over most of the world. The Synchronous Meteorological Satellite (SMS) system was designed and built by the National Aeronautics and Space Administration (NASA) to be operated by the National Environmental Satellite Service (NESS). The first of these satellites (SMS-1) was launched from the Kennedy Space Center in May 1974 and the second (SMS-2) in February 1975. In October 1975, NOAA launched GOES-1, the first operational geostationary

satellite, into an orbit, 35,783 km above the equator at 55°W longitude. These satellites were re-named GOES WEST and GOES EAST when SMS-2 was moved to its present location at 135°W as the western operational satellite in December 1975 and GOES-1 was moved to 75°W to replace SMS-1 as the eastern operational satellite in June 1976 (Figure 1-1). On-board equipment consists of a Visible and Infrared Spin-Scan Radiometer (VISSR), a Space Environment Monitor (SEM), a Data Collection System (DCS) and a weather facsimile broadcast system (Dismachek, 1975). Both GOES satellites provide visible and infrared imagery of the entire earth disk each half hour: on the hour and half hour from GOES EAST and every 15 minutes and 45 minutes after the hour from GOES WEST.

NESS has established facilities to build, maintain and operate the ground stations required to calibrate, acquire and process the data obtained by meteorological satellites in support of the applications work. The Direct Readout Ground Station (DRGS) for the GOES has, for the first time, produced data which is adequate in space, time, and spectral scales for detailed application to the solution of mesoscale problems.

Every half hour, the telemetry of the GOES instruments provides digital Visible and Infrared Spin-Scan Radiometer (VISSR) data corresponding to full-earth disk visible and infrared images. The visible full-earth disk
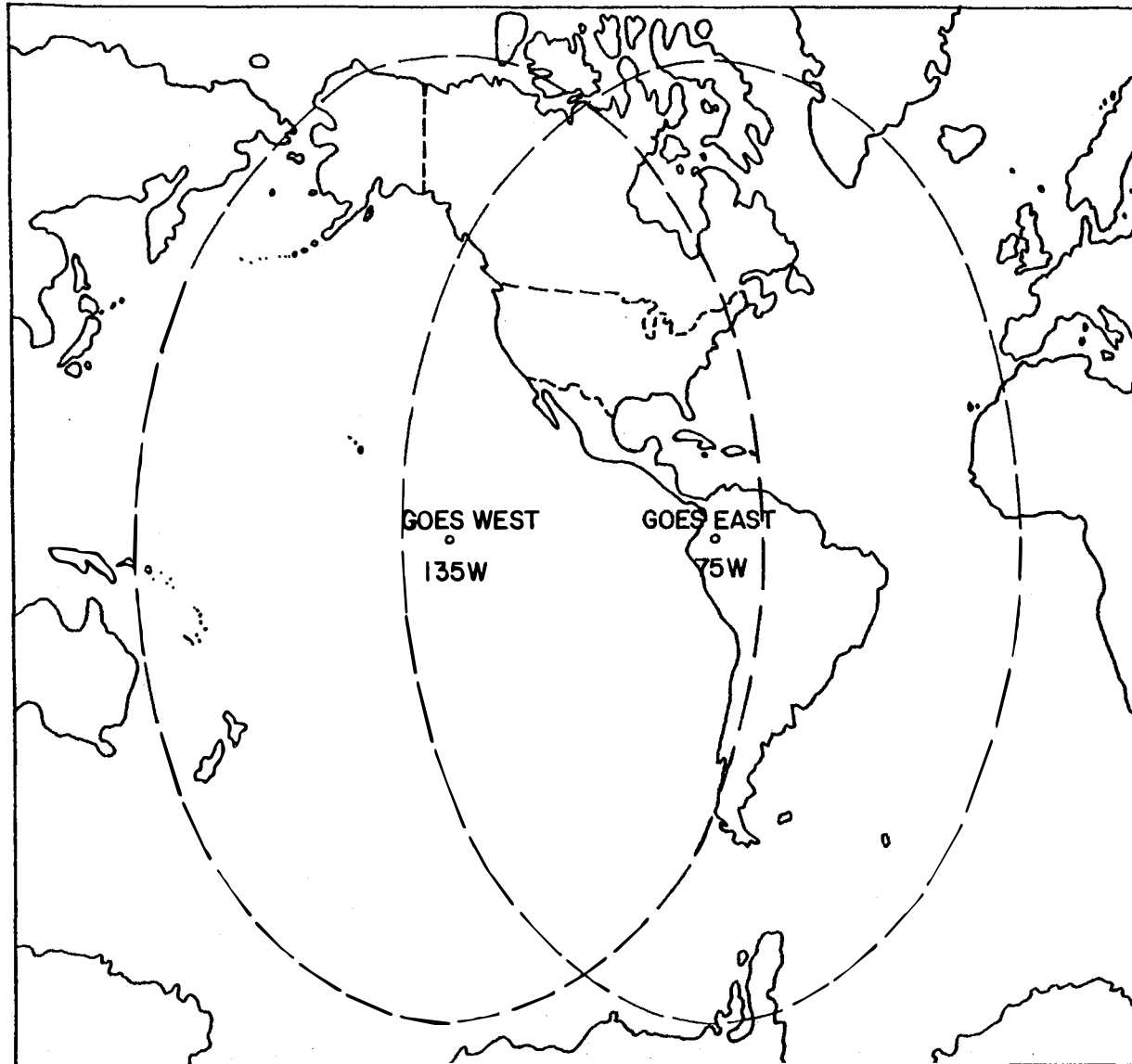
Figure 1-1   Location and approximate operational coverage of the two
satellite data sources.

consists of 14,400 scan lines with 15,288 pixels each; and the infrared full-earth disk consists of 1800 scan lines with 1,911 pixels each (Webb, 1975). The raw digital VISSR data tapes used in this study have been obtained from the Department of Atmospheric Science at Colorado State University (CSU) and have the general format of one record of infrared data followed by eight records of visible data.

The raw data tapes of intermingled visible and infra-red radiances were first processed to separate the visible from infrared data in time sequence before analysis of the measurements was performed. In order to identify the cloud cover region, a critical value of brightness to distinguish cloud from non-cloud background was determined using the ADVISAR (All Digital Video Imaging System for Atmospheric Research) at the Department of Atmospheric Science, CSU. This system is an interactive digital imaging display device producing black and white or color images of any digital type information in a range from 0-255 counts (Reynolds and Morris, 1978).

The target area of this study was a 315 x 315 km area, corresponding to array sizes of 216 x 216 points for visible data and 54 x 27 points for infrared data. Both visible and infrared data sets were centered at Big Spring, Texas. The actual size of a single visible data point in this study area was 1.46 by 1.46 km, while an infrared

data point covered an area equivalent to a 4 by 8 array of
visible data points, or a 5.84 by 11.68 km area.

Because of the location of the GOES WEST satellite
west of the target area in this study, the data were not
in a true north-south direction but were inclined at an
angle of 11.3° clockwise from north, as shown in Figure
1-2. All available satellite imagery photographs have
been collected for the period from 1 June to 15 July 1977,
the operational period of the Texas HIPLEX field program.
Four days, 22, 24 and 27 June and 8 July 1977 were chosen
for this study because of the availability of the following
data sources: visible and infrared images and digital
radiance data, rawinsonde data, raingage network measure-
ments and radar observations. Within these four days,
there were 44 sets of visible and infrared data available
for the cloud properties study.

The raingage network, located from 100.4 to 101.8°W
longitude and 32.0 to 32.9°N latitude, was included within
the target area, and consisted of fifty-nine recording
raingage stations. The raingage network measurements were
obtained for every 15-minute interval from 0000 GMT to
2359 GMT daily (e.g. 96 sets of measurements per day).
The National Weather Service WSR-57 radar observation
records from Midland were available nearly every 10 minutes
and digital radar reflectivities from a M-33 radar operated
by Meteorology Research, Incorporated, (MRI) at Snyder have
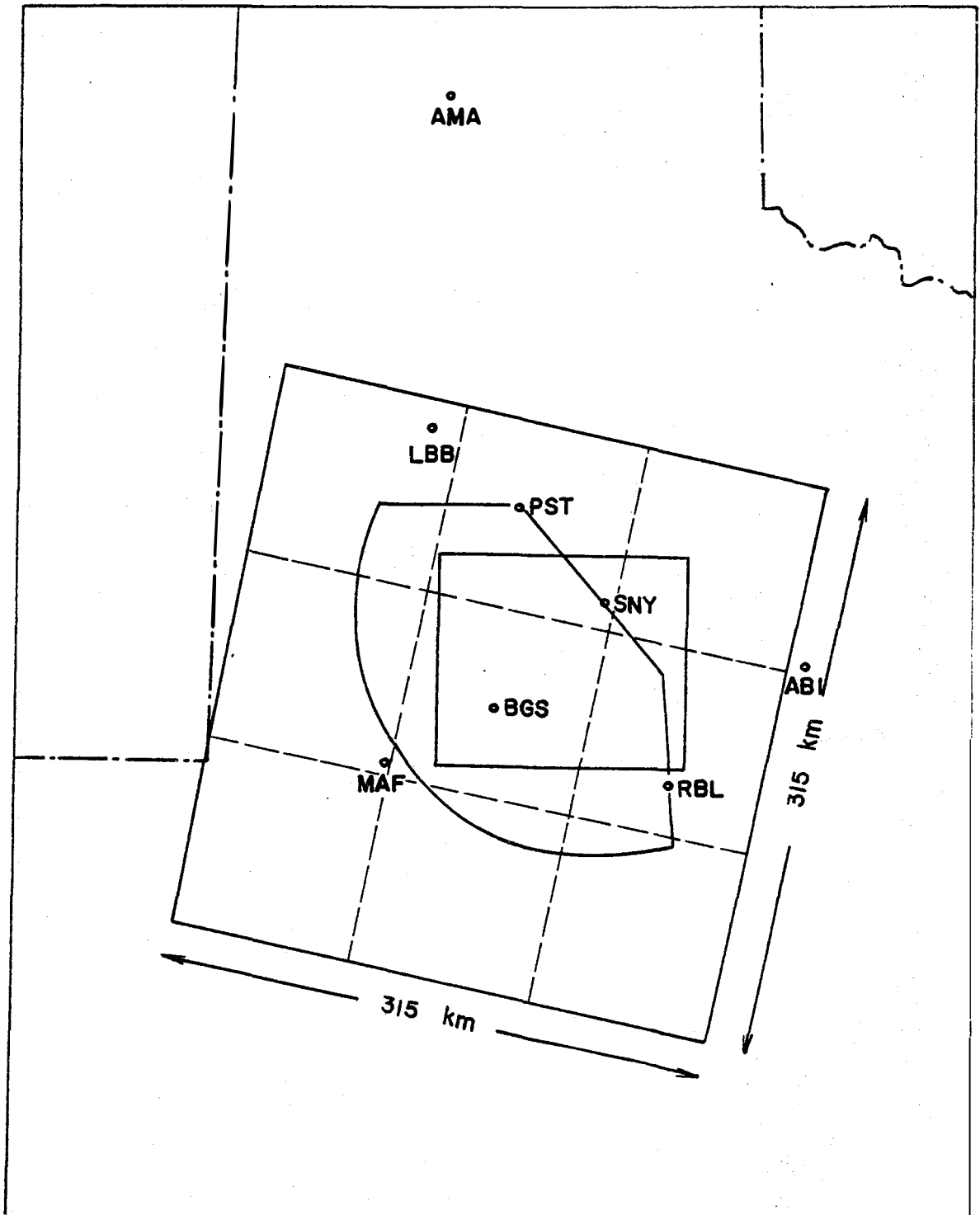
Figure 1-2   The area of study.   The sector at the center
is the Texas HIPLEX study region.   The small
rectangle is the raingage network.

been obtained. A computer program has been developed to display the digital data in both PPI and RHI presentations.

1.2. Survey of Literature

In the late 1940's the first photographs from outer space of the earth and its cloud patterns were taken from research rockets fired at White Sands, New Mexico (Widger, 1966). The area viewed was limited to a radius of about 500 miles from the launch site.

The launches of the TIROS (1960-1965), ESSA (1966-1969), Nimbus (1964-1975) and NOAA (1970-1976) series of satellites have made available cloud cover photographs of the whole earth. In addition, improved visible and infra-red radiance data have become available from satellites for atmospheric study. In recent years there has been much more attention given to the question of remote sensing techniques in order to measure atmospheric proper-ties such as the temperature variation with height (Smith, 1969), cloud albedo (Gruber, 1973; Mosher, 1974; Park, 1974; Charney, et al., 1977), reflected radiance measure-ment (Vonder Haar, 1970), and estimated rainfall from satellite imagery (Scofield, et al., 1977).

Gruber (1973) pointed out that a variety of satellite measurements of the albedo and outgoing long-wave radiation from the earth-atmosphere system exist. Differences in results obtained from different satellites and in different

years as well as differences in results between investigators using the same satellite data have been discussed.

Reynolds and Vonder Haar (1977) developed a technique called the "bispectral method" which determined cloud heights and amounts through the use of simultaneous infrared and visible satellite radiance data from the NOAA satellites to determine the cloud height by comparing cloud top temperature with an upper air sounding. In their opinion, the VISSR data from the GOES series of satellites is probably the best currently available for use with this method.

Ogura and Liou (1979) studied a well-organized squall line which passed through the mesonetwork of the National Severe Storms Laboratory (NSSL) in central Oklahoma on 22 May 1976. The precipitation analysis from the NSSL mesonetwork, PPI echo-contoured displays from the WSR-57 NSSL radar, subsynoptic and small-scale features, such as surface convergence, relative vorticity soundings, vertical motion, temperature, mixing ratio and equivalent potential temperature, were considered in that study.

Leary and Houze (1979) examined the structure and evolution of convection in a double cloud cluster in the trough of an easterly wave that passed over the data network of the Global Atmospheric Research Programs' Atlantic Tropical Experiment (GATE) utilizing both PPI and RHI displays from four quantitative shipboard weather

radars. Six mesoscale precipitation features were identi-
fied in that research, and the processes active in the
formative, intensifying, mature and dissipating stages of
their life cycle were identified.

A technique was developed by Reynolds and Smith
(1979) to digitally integrate satellite and radar imagery
in a common coordinate reference frame. Composite displays
were prepared on CSU's ADVISAR by using GOES visible and
infrared data, 5 cm radar data and recording raingage data.
The usefulness of combining two independent remotely sensed
data sets into a common reference frame was demonstrated by
applying the composite technique to two case studies.

From the literature review, it can be concluded that
the method of determining cloud top heights by comparing
satellite-derived cloud top temperature with the upper air
sounding data is reliable. In addition, verification of
the satellite-derived results obtained by comparison with
radar and rainfall measurements should prove valuable,
because it may become practical to extend satellite-
derived results to regions for which radar and raingage
data are not available. The techniques which have been
developed already, such as determining albedo, cloud top
temperature, cloud height, cloud type and cloud number
(Jurica and Chi, 1979) have been applied to the case study
days mentioned above. The results of this analysis were
then compared with both radar and raingage data, employing
some aspects of the studies described previously.

CHAPTER 2

DETERMINATION OF CLOUD PROPERTIES
FROM SATELLITE DATA

This chapter will discuss the data acquisition systems and data processing techniques for visible and infrared radiance measurements which were employed in subsequent chapters. These methods were then applied to the radiance data on the selected case study days, and the derived results will be presented and discussed.

2.1 Available Data

The satellite system from which the radiance and imagery data was collected in this study is the GOES. The satellites GOES EAST and GOES WEST are in geosynchronous orbits located at 75^OW and 130^OW, respectively, over the equator, viewing the Western Hemisphere (Figure 1-1).

In the Visible and Infrared Spin-Scan radiometer (VISSR), the radiated energy reflected and emitted from the earth's surface and atmosphere is collected by 8 visible channel sensors and 2 infrared sensors. The visible sensors collect energy in the 0.55 to 0.75 μm range, while the infrared radiation is located between 10.5 and 12.5 μm.

The GOES data are received and transmitted by the Data Acquisition and Processing System (DAPS) of NESS. All

data for central processing are acquired in a compressed
format by the two NESS Command and Data Acquisition (CDA)
stations which are located at Wallops Island, Virginia
and Gilmore Great, Alaska (NESS, 1978).

The National Weather Service Forecast Office at
Lubbock received the visible and infrared imagery which
are used in this study.

2.2   Determination of Cloud Properties
      from Visible Radiance Data

The determination of a visible radiance critical value
to distinguish clouds from the underlying non-cloud surface
is a primary goal in the analysis of radiance data for this
study. There are several factors which influence the radi-
ance reflected from a cloud including physical cloud proper-
ties and non-cloud properties. These include the size and
shape of the cloud particles, the number density of scatter-
ing particles in the cloud, cloud thickness, the shape of
the cloud, as well as the zenith angle of the sun and the
satellite (Mosher, 1974). The method used to determine the
critical values for different times of day on the four
case-study days consisted of displaying the visible radi-
ance data on the ADVISAR at CSU.

The intensity of the reflected solar radiance depends
on the albedo of earth and atmosphere and also on the
zenith angle of incoming solar radiation. A different

brightness value will be measured for a given cloud albedo
at different times of day. The primary cause of this vari-
ation is the solar zenith angle, because the larger the
solar zenith angle the smaller will be the visible
brightness value measured for a certain albedo. A larger
solar zenith angle corresponds to a longer path length
through the atmosphere and greater attenuation. Therefore,
the variation in atmospheric attenuation is caused by the
change in solar zenith angle with time. Knowing the zenith
angle of the incoming solar radiation and the reflected
short-wave radiance, the value of albedo corresponding to
a given visible value was obtained for each spot based on
the critical value at that time. The curve of albedo
versus brightness, shown in Figure 2-1, was obtained from
a calibration of the VISSR visible sensors with ground
targets of known albedos (Smith, 1977).

2.3 Determination of Cloud Properties
     from Infrared Radiance Data

The VISSR sensor also gathers radiant flux emitted by
the viewed target in the infrared spectrum, and converts
it into digital counts with a range from 0 to 255. The
infrared values can provide estimates of the earth surface
temperature under clear skies and cloud top temperature
under cloud-cover conditions. A linear correlation between
the infrared counts and temperature has been extracted from
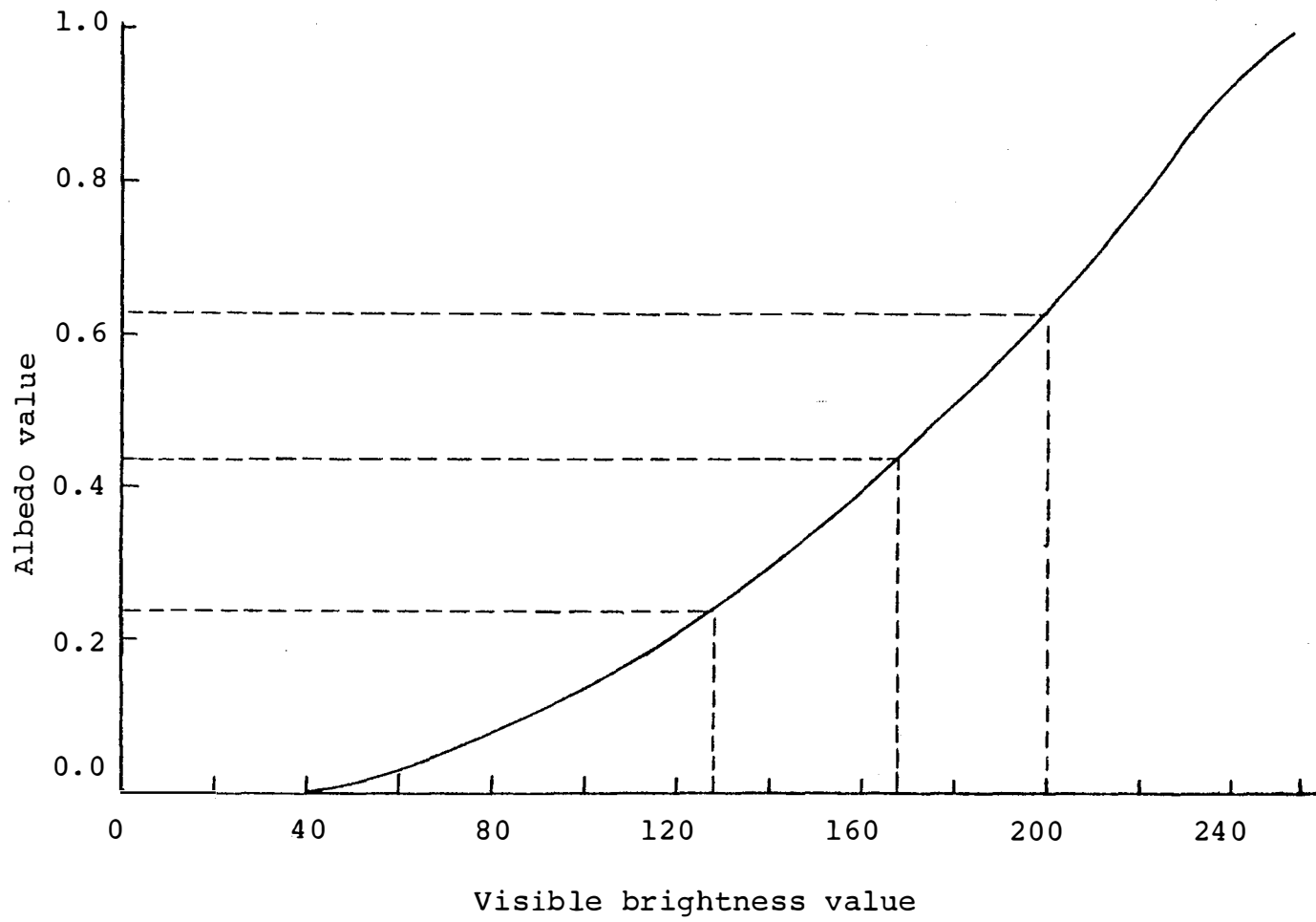
Figure 2-1 Albedo versus visible brightness value
for zero solar zenith angle.

the NESS standard calibration as follows:

$$T = \frac{1}{2} (660 - C) \quad \text{for} \quad 0 \leqq C \leqq 175$$

$$T = 418 - C \quad\quad\quad \text{for } 175 < C \leqq 255$$

where C is the infrared data value and T is absolute temperature (K).

This relation can be represented by two straight lines intersecting at the point for which the infrared value is 175 and temperature is 242.5 K (Figure 2-2). From the two equations above, it can be seen that temperature decreases in steps of 0.5 K from 330 to 242.5 K as the infrared count increases in unit steps from 0 to 175, and decreases by 1 K per unit step to the lowest value of 163 K at an infrared value of 255. Consequently, cold objects (high clouds) appear white in photographs, and warm objects (sea surface) appear dark in accordance with visually observed atmospheric phenomena. Having determined the cloud top temperatures, cloud top height was estimated from temperature sounding data.

In order to derive cloud top heights from cloud top temperatures, a vertical temperature profile must be obtained from sounding data. On each Texas HIPLEX operational day of 1977, sounding data were gathered by Texas A & M University for three-hour intervals at Big Spring, Midland, Post and Robert Lee (Scoggins, 1977). Soundings were available at 1500, 1800, 2100 GMT on each case study
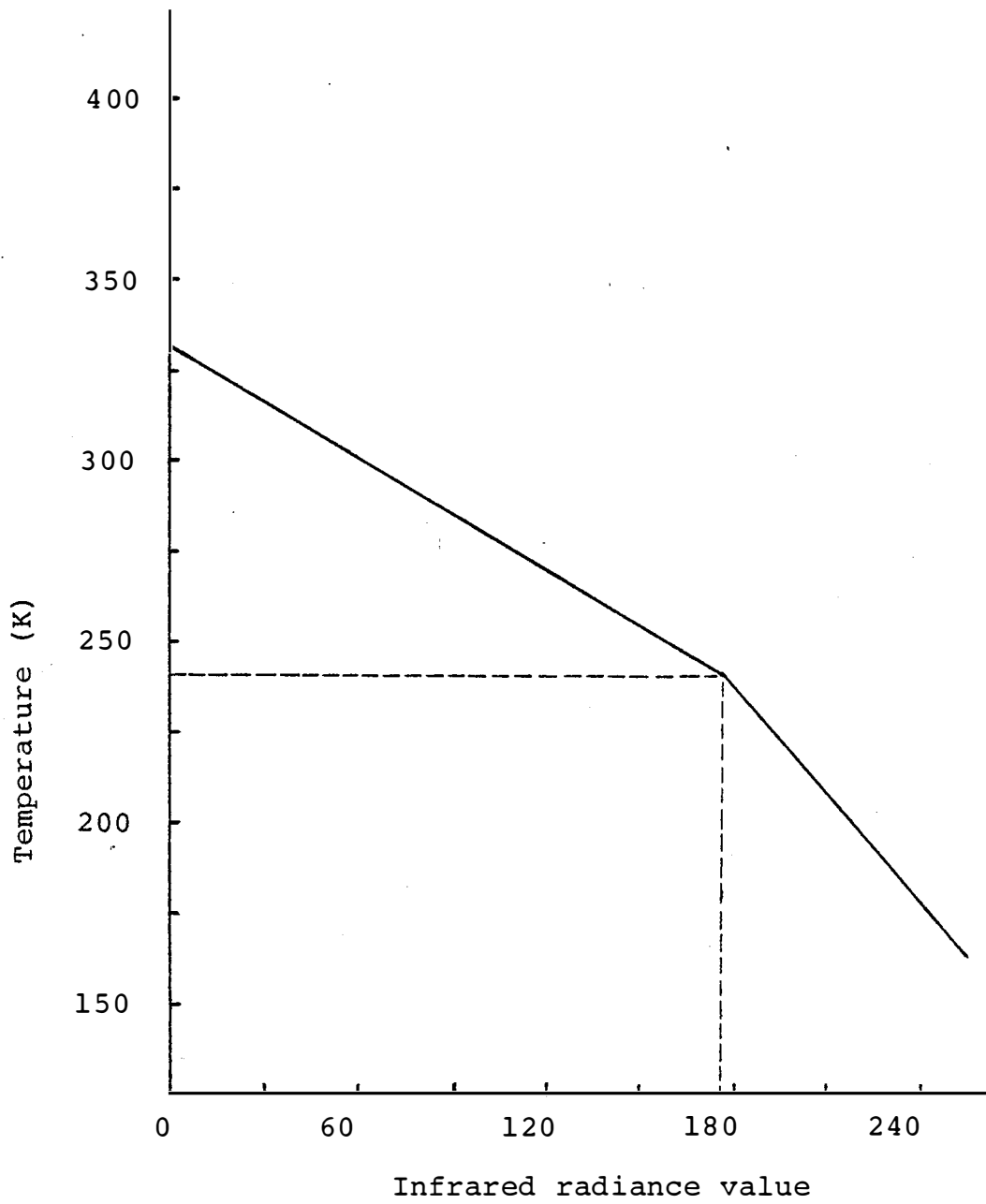
Figure 2-2   NESS standard calibration curve for
             temperature versus infrared radiance
             value.

day and 0000 GMT of the next day. The cross sections of
vertical temperature versus time for the four case study
days at Big Spring are shown in Figures 2-3 to 2-6. From
these four vertical temperature profiles, it was found
that at upper levels the isotherms were nearly horizontal
which indicated that the long-wave radiation escaping
from cloud tops did not vary much with time. The
isotherms of 8 July were more variable at low altitudes
due to the unstable weather conditions at that time. The
rainfall of the 22 June and 8 July cases kept the surface
temperature cooler than that of other cases. Time-
averaged isotherm heights at the four stations on each
case study day are given in Table 2-1. Since the vertical
temperature structures were so similar from station to
station, average sounding curves for the four stations on
the four different days provided an approximate relation
between temperature and cloud-top height for each day.
The time and space averaged soundings are shown in
Figure 2-7. From the heights given in Table 2-1, it can
be seen that the use of an average sounding results in
cloud-top estimates within a few hundred meters of actual
value. This technique of estimating cloud-top height
was applied for verification of the satellite-derived
results, as discussed in Chapter 4.
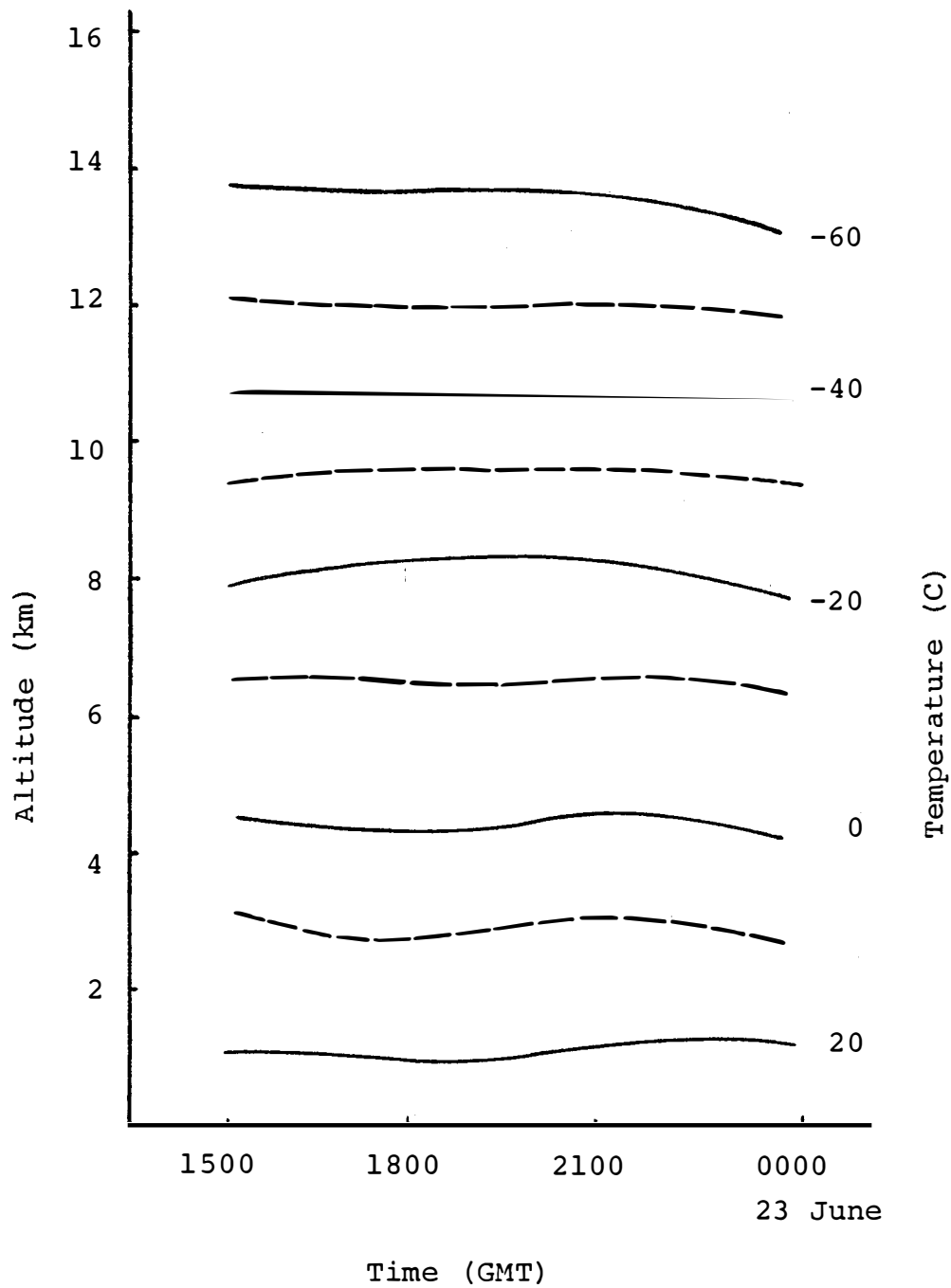
Figure 2-3   Altitude and time variation of temperature
on 22 June 1977 at Big Spring, Texas.
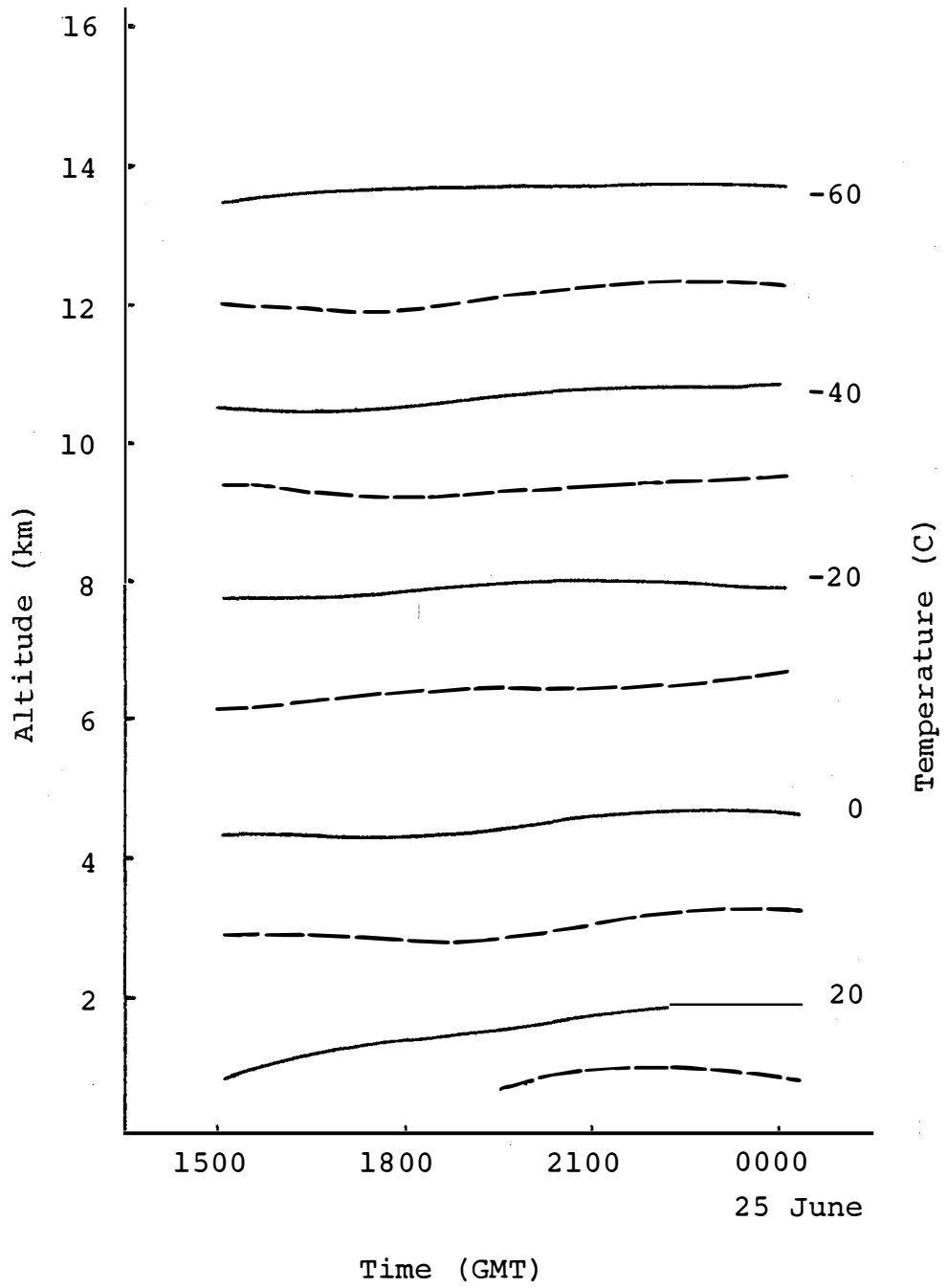
Figure 2-4   Same as Figure 2-3 for 24 June 1977.
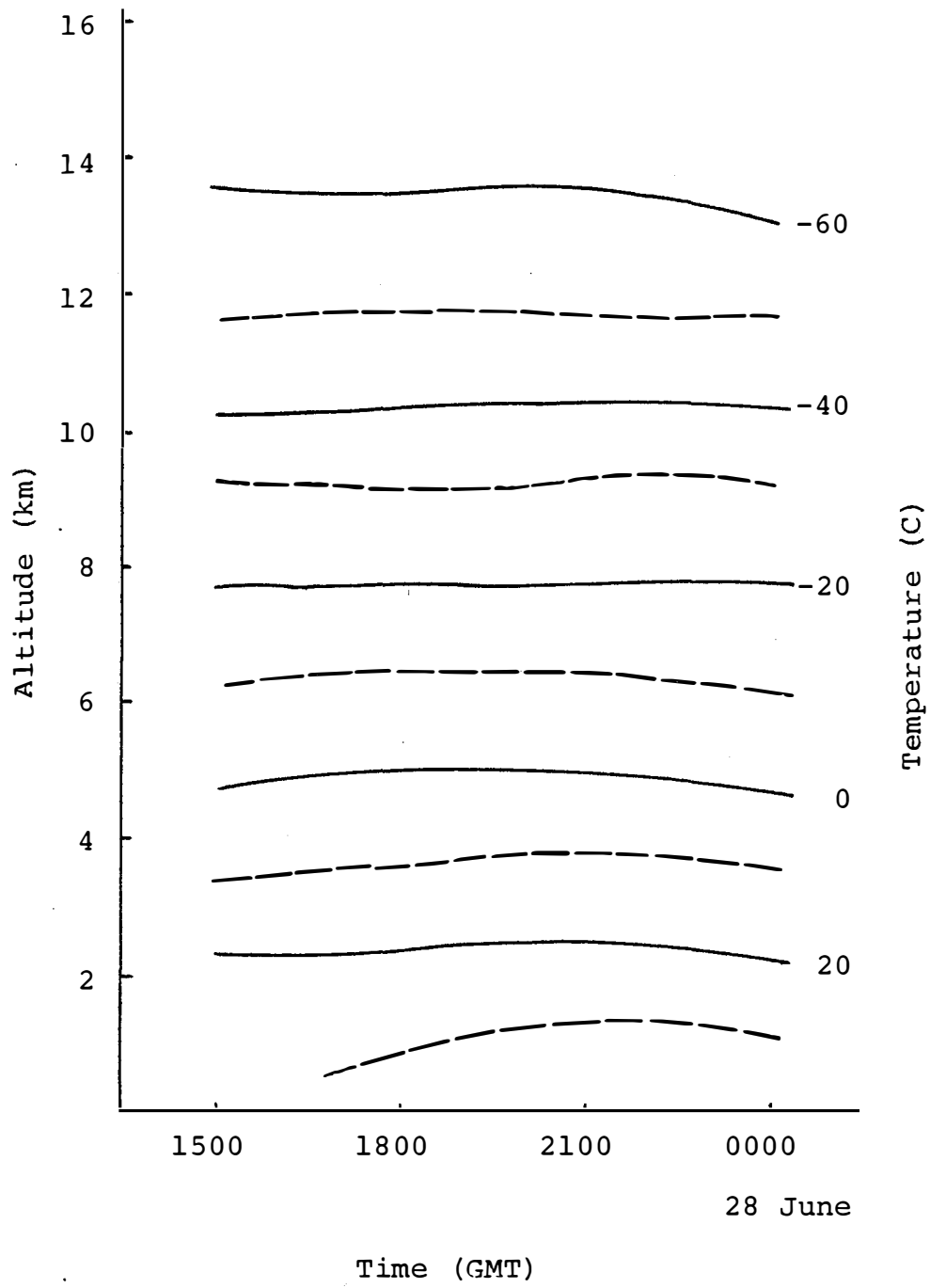
Figure 2-5 Same as Figure 2-3 for 27 June 1977.
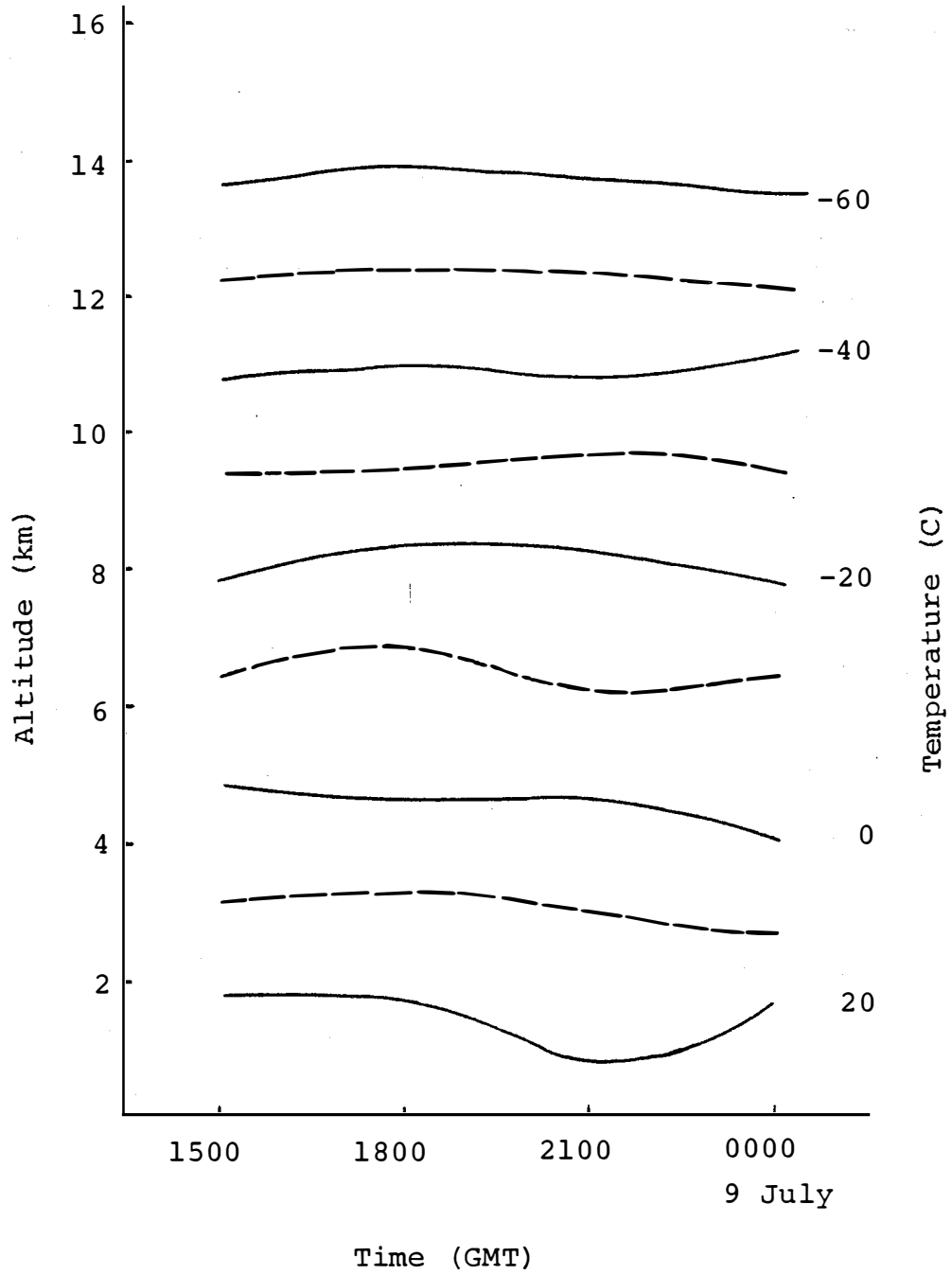
Figure 2-6 Same as Figure 2-3 for 8 July 1977

Table 2-1

Time-averaged isotherm heights (gpm) for four
rawinsonde stations in the study area.

	Midland				Post			
Temp. (C)	22 June	24 June	27 June	8 July	22 June	24 June	27 June	8 July
30	–	961	1301	978	–	–	1250	–
20	1211	1725	2459	1802	1051	1237	2472	1570
10	2950	3097	3690	3109	2768	3069	3562	2982
0	4662	4536	4872	4436	4468	4407	4873	4510
-10	6550	6415	6278	6567	6355	6368	6379	6399
-20	8107	7955	7822	8041	7871	7807	7703	7838
-30	9434	9356	9135	9400	9222	9293	9039	9302
-40	10657	10778	10398	10741	10444	10589	10480	10657
-50	11936	12084	11676	12134	11599	11972	11534	11944
-60	13383	13539	13394	13512	13271	13420	12933	13337

Table 2-1 Continued

Temp. (C)	Robert Lee				Big Spring			
	22 June	24 June	27 June	8 July	22 June	24 June	27 June	8 July
30	-	648	1065	734	-	877	1209	913
20	1233	1416	2297	1658	1132	1530	2373	1521
10	2713	3048	3514	3034	2891	3052	3593	3096
0	4418	4531	4566	4528	4473	4515	4831	4580
-10	6252	6420	6216	6512	6466	6459	6346	6515
-20	8031	7987	7520	8038	8036	7983	7709	8087
-30	9335	9427	8896	9368	9480	9403	9101	9450
-40	10594	10671	10220	10717	10692	10789	10382	10855
-50	11828	11968	11455	12002	11985	12117	11687	12237
-60	13255	13304	13069	13397	13555	13718	13381	13702
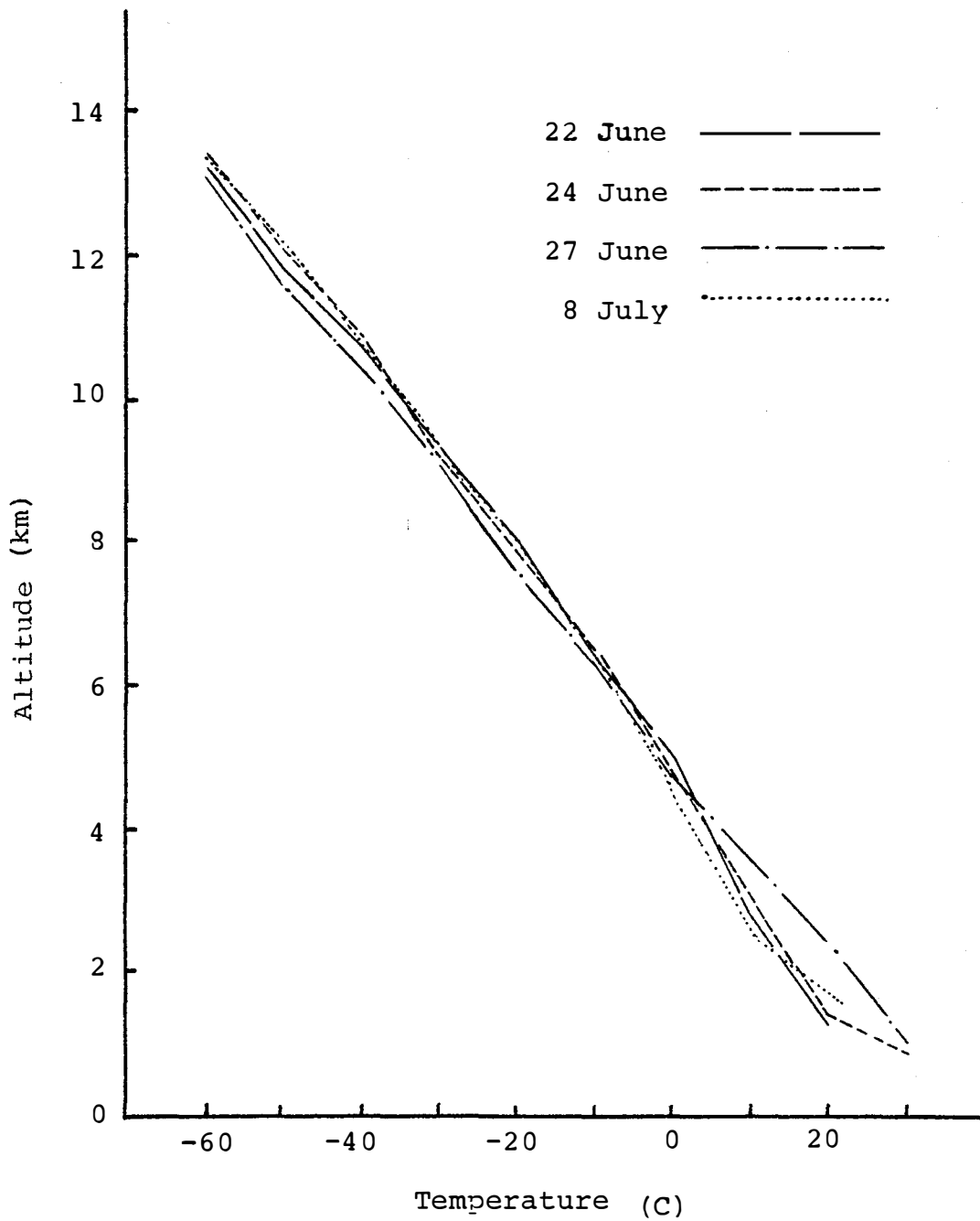
Figure 2-7 The average sounding of the four upper air
stations for the four case-study days.

2.4 Alignment of Visible and Infrared Data

As mentioned above, the visible and infrared data arrays consisted of 216 x 216 and 27 x 54 elements for the target area, respectively. The visible and infrared sensors on the GOES scan the globe simultaneously from west to east as they progress from north to south. A misalignment between visible and infrared VISSR sensors was detected during analysis of the 1976 data sets.

It has been found that a misalignment between visible and infrared data existed in the 1977 data as well. The method used to check misalignment of 1977 data consisted of simultaneously displaying both visible and infrared data sets on the ADVISAR. In order to best match the cloud cover areas of both visible and infrared data, the critical values which distinguish the cloud area from non-cloud background were increased for both visible and infrared data. As a result, the remaining cloud patterns displayed on ADVISAR were confined to the most dominant features. Although the resolution of the infrared data was poorer than that of visible data, the misalignment was easily detected. Figure 2-8 displays the difference in data set matching at 2115 GMT, 27 June before and after shifting of the infrared data array. The visible data were displayed in blue, while the infrared data were displayed in red. Black areas defined regions of low values of both visible and infrared radiance, while white areas located the super-
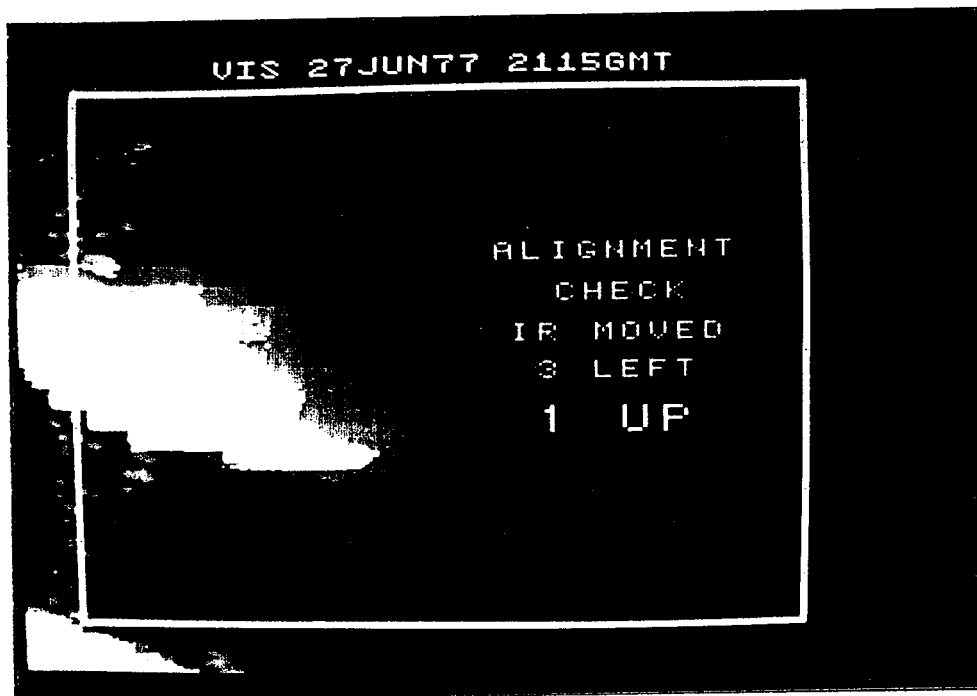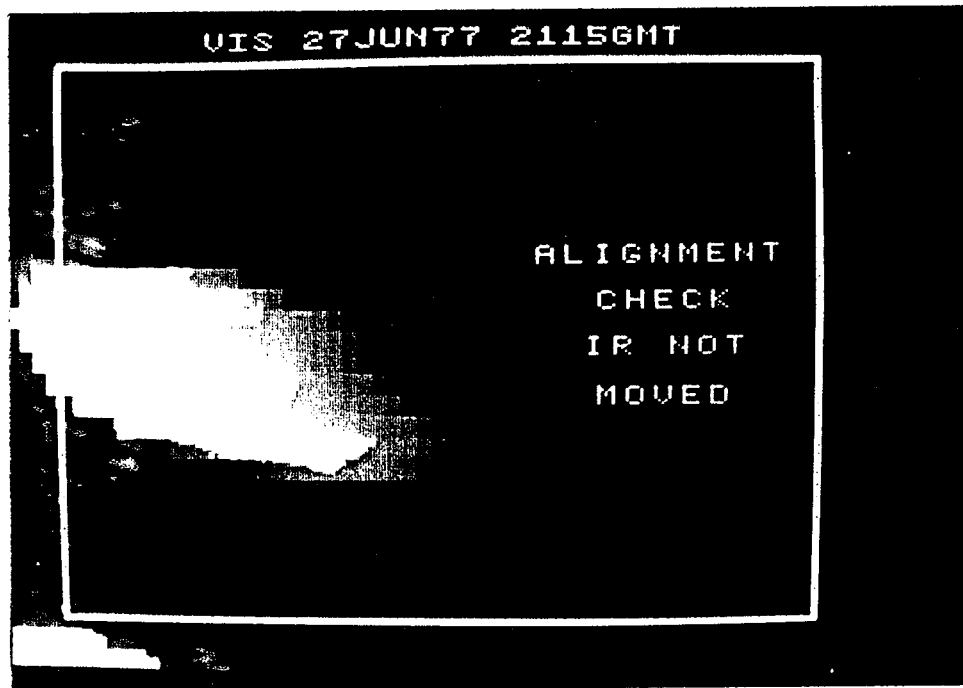
Figure 2-8   ADVISAR images used in check of alignment of
             visible and infrared data arrays at 2115 GMT
             on 27 June 1977. The upper picture is before
             shifting the infrared data set and the lower
             one is after shifting.

position of bright visible and cold infrared measurements. The larger the white and black areas and the smaller the red and blue areas, the better the match between the two data sets. Comparison of the two pictures showed that the match was better after the infrared data array was moved three pixels left and one pixel up. Because of this movement, all the elements of the infrared array were moved about 20 km away from their initial positions.

The alignment procedure described here was applied to all visible and infrared data set pairs analyzed in subsequent chapters.

CHAPTER 3

SATELLITE-DERIVED CLOUD PROPERTIES

The visible radiance data were analyzed with a cloud summary program. The principal input parameter for each time on the four case study days was the critical brightness, determined with the ADVISAR, to distinguish cloud from non-cloud surface. Based on this critical value, the boundary of each cloud was outlined as an isopleth of the critical brightness value. A number of statistical products, such as mean cloud brightness and variance of cloud brightness, as well as the cloud size were generated through the cloud summary program. In order to facilitate cloud-movement tracking, the geometric and brightness centers were also determined. The gravity-center method used to determine the geometric center involves locating the median row and column of the cloud from a point-by-point count of cloud pixels. The location of the brightness center was determined in a similar manner, using individual brightness values as weighting factors for each pixel. In addition, the maximum brightness value and its location in each cloud were tabulated.

After the cloud-by-count statistics were accumulated, the following comprehensive information was obtained: (1) percentages of cloud cover and non-cloud area within the study area; (2) mean brightness values of the total

cloud and non-cloud area; (3) brightness distribution of all data points; (4) distribution of cloud mean brightness; and (5) distribution of cloud size.

3.1 Cloud Populations

Using the cloud summary program and critical values to distinguish cloud from non-cloud surfaces, the number of clouds and percent cloud cover was obtained for each time on the four case-study days. The minimum cloud size of interest in this study is a cloud of four pixels, equivalent in area to a circular cloud of about 3.3 km diameter. All the clouds with size equal to or less than three points, were discarded by the cloud summary program. The percent cloud-cover over the whole area was obtained as the total of all clouds defined in this manner.

There were several categories employed to separate clouds according to their size as follows:

1. Tiny clouds, less than 4 pixels, corresponding to a circular cloud diameter less than 3.3 km, were neglected here.

2. Isolated convective clouds:

   (a) Small clouds, 4 to 7 pixels, with an equivalent diameter between 3.3 km and 4.3 km, usually a fair weather cumulus cloud;

   (b) Medium clouds, with 8 to 37 pixels, having an equivalent diameter between 4.3 km and 10 km,

cumulus congestus in most cases;

    (c) Large clouds, with 38 to 148 pixels and an equivalent diameter between 10 km to 20 km, and usually identified as cumulonimbus;

3. Widespread deep convective or stratiform clouds, with more than 148 pixels, corresponding to an equivalent diameter larger than 20 km, and identified as a widespread deep convective cloud for high mean brightness or as area of stratiform cloud for low mean brightness.

The cloud populations in various size categories derived from the cloud summary program are given in Table 3-1. A number of different patterns were found to occur. Large numbers of clouds appeared on 24 June and early on 8 June, with much smaller numbers of clouds on the other two days. Generally speaking, the number of small and medium isolated convective clouds dominated the total number of clouds. As a result, the numerous small and medium isolated clouds of 24 June and early on 8 July led to large total numbers of clouds at these times. However, the percent cloud cover was always dominated by the widespread convective and stratiform clouds, independent of the total cloud number, as discussed in the next section.

3.2 Percent Cloud Cover

The percent cloud cover for all 44 data sets during

Table 3-1   Number of clouds of different sizes

TIME (GMT)	22 June				24 June				27 June				8 July			
	2a*	2b*	2c*	3*	2a	2b	2c	3	2a	2b	2c	3	2a	2b	2c	3
1745	–	–	–	–	20	28	7	3	0	0	0	0	33	36	5	3
1815	4	4	1	1	27	26	7	2	0	0	0	0	–	–	–	–
1845	1	2	3	3	30	24	4	2	1	0	0	0	27	28	6	5
1915	5	7	0	1	28	26	9	3	1	1	0	0	15	17	5	4
1945	6	5	2	2	25	32	3	4	0	2	3	0	14	15	5	4
2015	2	5	0	1	33	35	7	3	6	1	2	2	15	7	0	1
2045	1	3	0	1	29	31	5	5	4	6	2	3	–	–	–	–
2115	6	15	1	1	24	22	7	4	10	12	1	1	12	12	0	1
2145	12	19	4	2	–	–	–	–	–	–	–	–	–	–	–	–
2215	7	12	2	3	20	10	2	1	5	11	5	2	–	–	–	–
2245	6	5	0	1	4	4	1	1	–	–	–	–	7	13	4	1
2315	11	3	2	2	10	10	2	2	–	–	–	–	–	–	–	–
2345	2	3	1	1	13	19	5	2	–	–	–	–	10	19	4	1
0015	8	7	2	1	15	8	2	2	–	–	–	–	5	9	2	1

*2a: Small convective: diameter between 3.3 km to 4.3 km

*2b: Medium convective: diameter between 4.3 km to 10 km

*2c: Large convective: diameter between 10 km to 20 km

* 3: Widespread: diameter larger than 20 km

the four case studies was obtained from the computer cloud summary program. It was computed as the ratio of the number of data points within the cloud boundary, determined by the critical visible value, to the total number of data points within the study area. Figure 3-1 compares the percent cloud cover results over the study area for the four days. On 22 June, cloud cover exceeded 80% much of the day. Large percent cloud cover also occurred during the late afternoon of 8 July. The early afternoon of both 24 and 27 June was dominated by small isolated clouds, which kept the cloud cover small and even clear for the first four times on 27 June. But, on both days in the late afternoon, a storm moved into the study area from the west, contributing to increased cloud cover over the study area. Figure 3-2 shows the contrasting cases of large percent cloud cover contributed by only a few clouds and small percent cloud cover despite the presence of many clouds. The cloud cover at 2045 GMT, 22 June was 87%, although there were only 5 separate clouds at this time. The percent cloud cover at 1845 GMT, 24 June was only 6.1%, despite the presence of 60 clouds in the study area.

From Figure 3-3, it is noteworthy that the size of the largest cloud at each time closely matched the tendency of the percent cloud cover shown in Figure 3-1. Once again, the percent cloud cover was strongly dominated by the widespread convective and stratiform clouds, especially on 22 June when the number of clouds was not large.
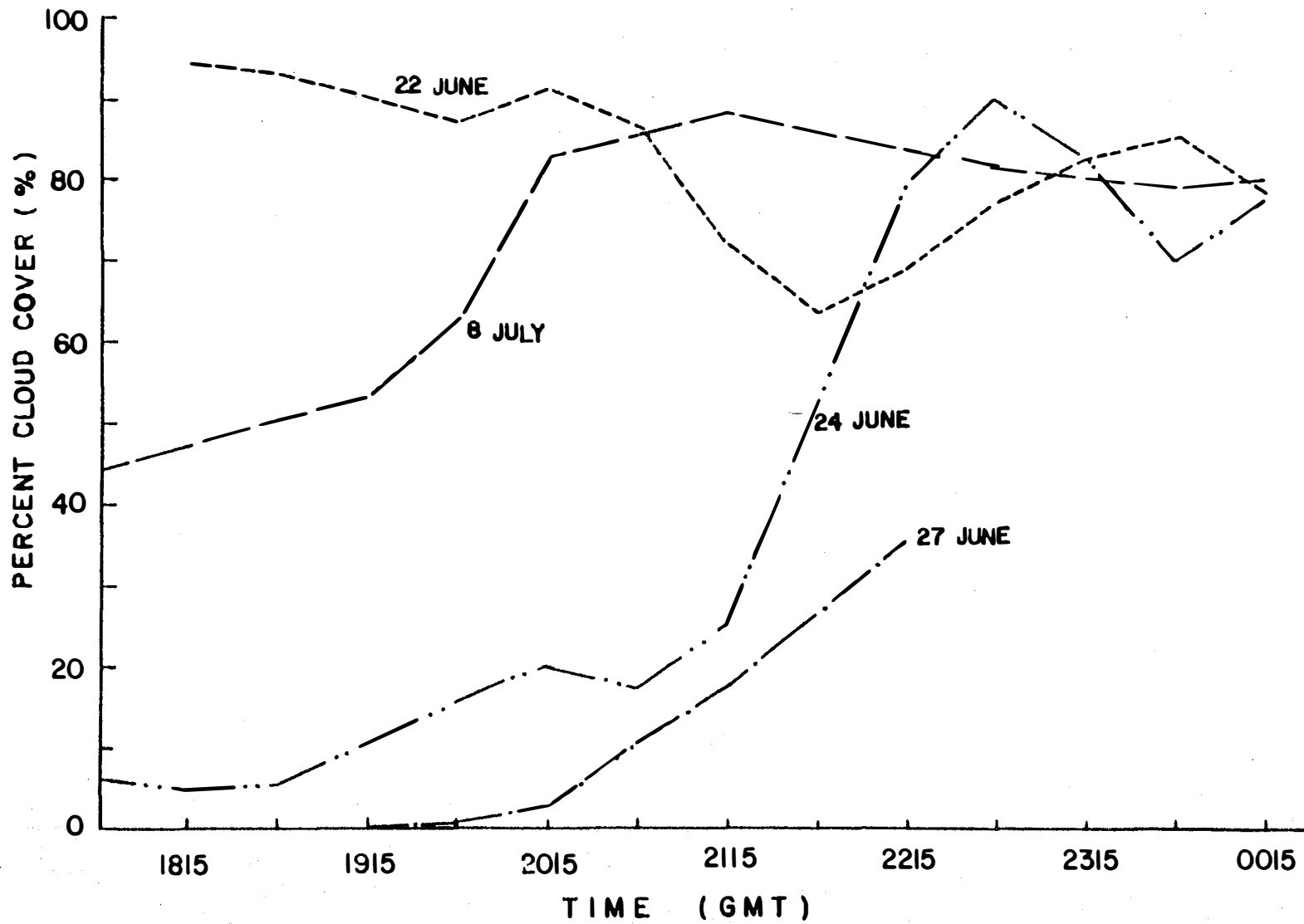
Figure 3-1   Variation of percent cloud cover with time.
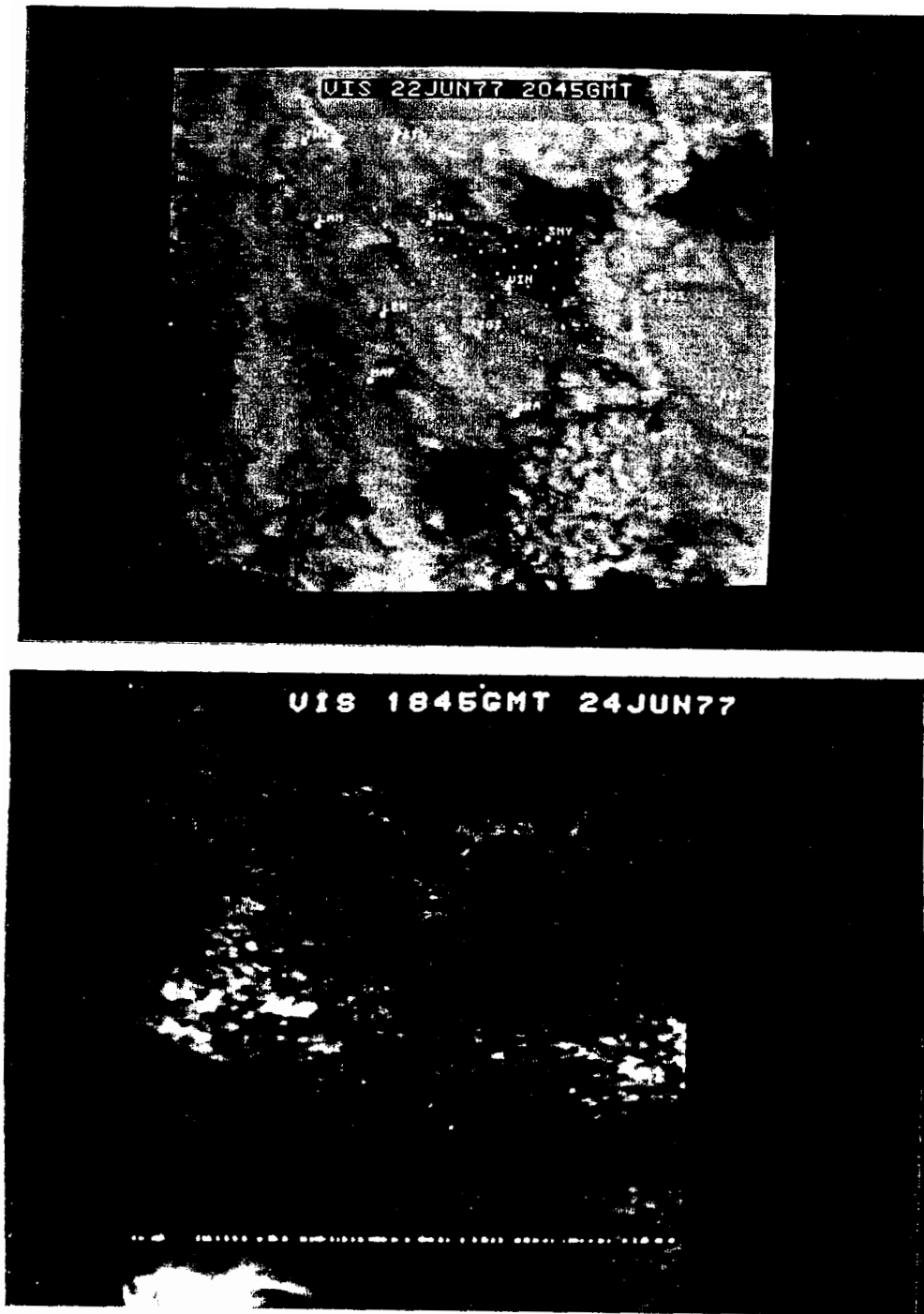
Figure 3-2 ADVISAR visible images at 2045 GMT 22 June 1977
and 1845 GMT 24 June 1977. In the upper picture
the percent cloud cover is large although there
are only a few clouds, and the lower one the
percent cloud cover is small despite the presence
of many clouds.
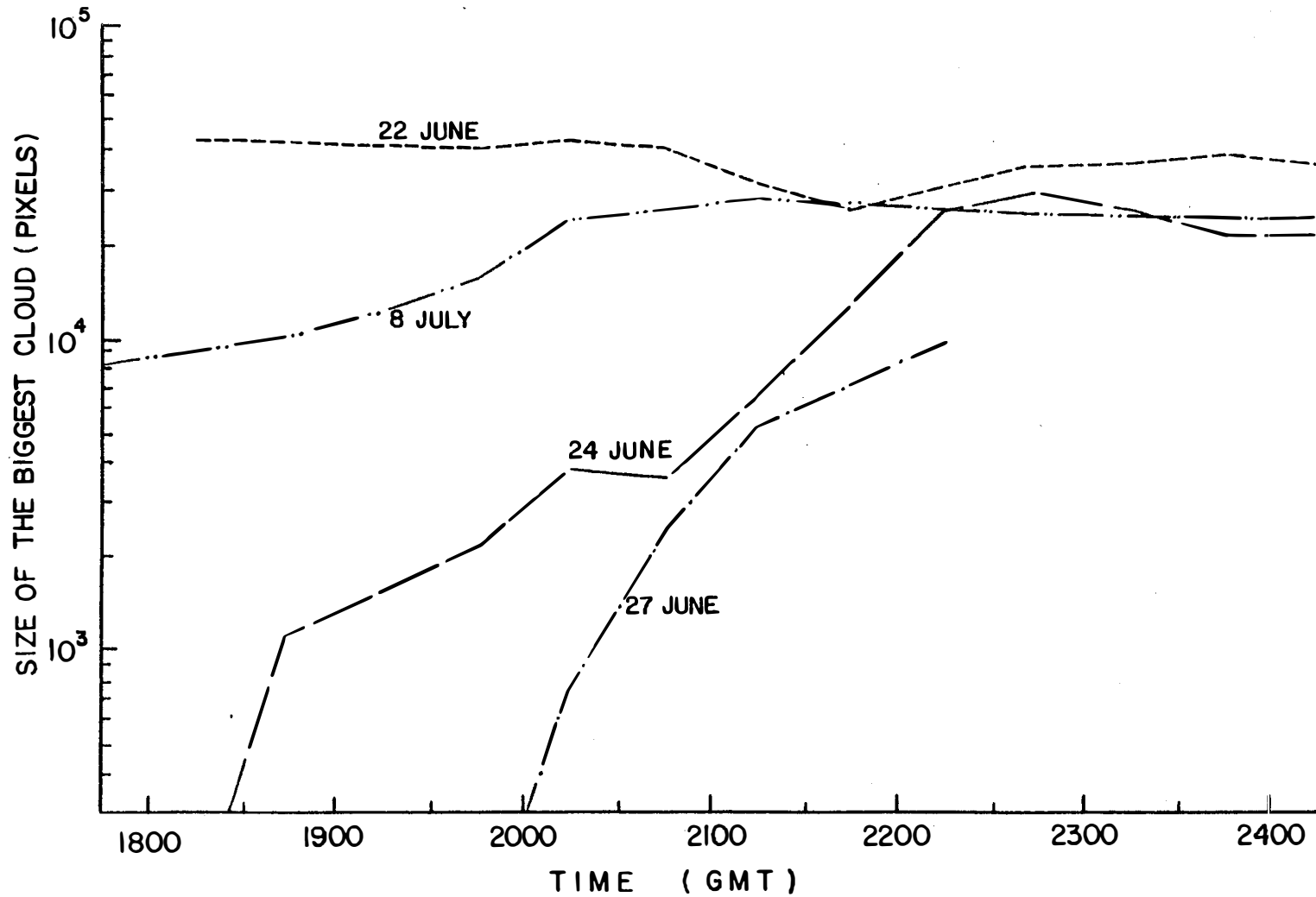
Figure 3-3 Variation of the biggest cloud size with time.

3.3 Cloud Brightness

The appearance of a cloud viewed from satellite alti-
tude depends on the visible brightness values, which vary
with solar zenith angle for a given cloud. The brightness
values decrease because of increased attenuation along a
longer path through the atmophere as the solar zenith angle
becomes larger in the late afternoon. A visible brightness
frequency distribution table was obtained from the computer
cloud summary program at each analysis time for the four
case study days. The visible brightness frequency distri-
bution curves for four selected times at two-hour intervals
are shown in Figures 3-4 through 3-7. In each figure, the
scale is the difference of individual brightness values
relative to the critical value distinguishing cloud from
non-cloud background for the given time. The appearance of
the brightness distribution curves is closely related to
the percent cloud cover at the corresponding time. A com-
parison between Figure 3-1 and Figures 3-4 through 3-7
shows that large cloud cover (greater than 70%) occurred
when the mode of the brightness distribution curve was
positive, and that small cloud cover (less than 45%)
corresponded to a negative modal value.

The modal values at 1815 and 2015 GMT on 22 June and
0015 GMT on 23 June were from 40 to 60 units greater than
the critical visible value at those times and the mode at
2215 GMT was 76 units above the critical value. The
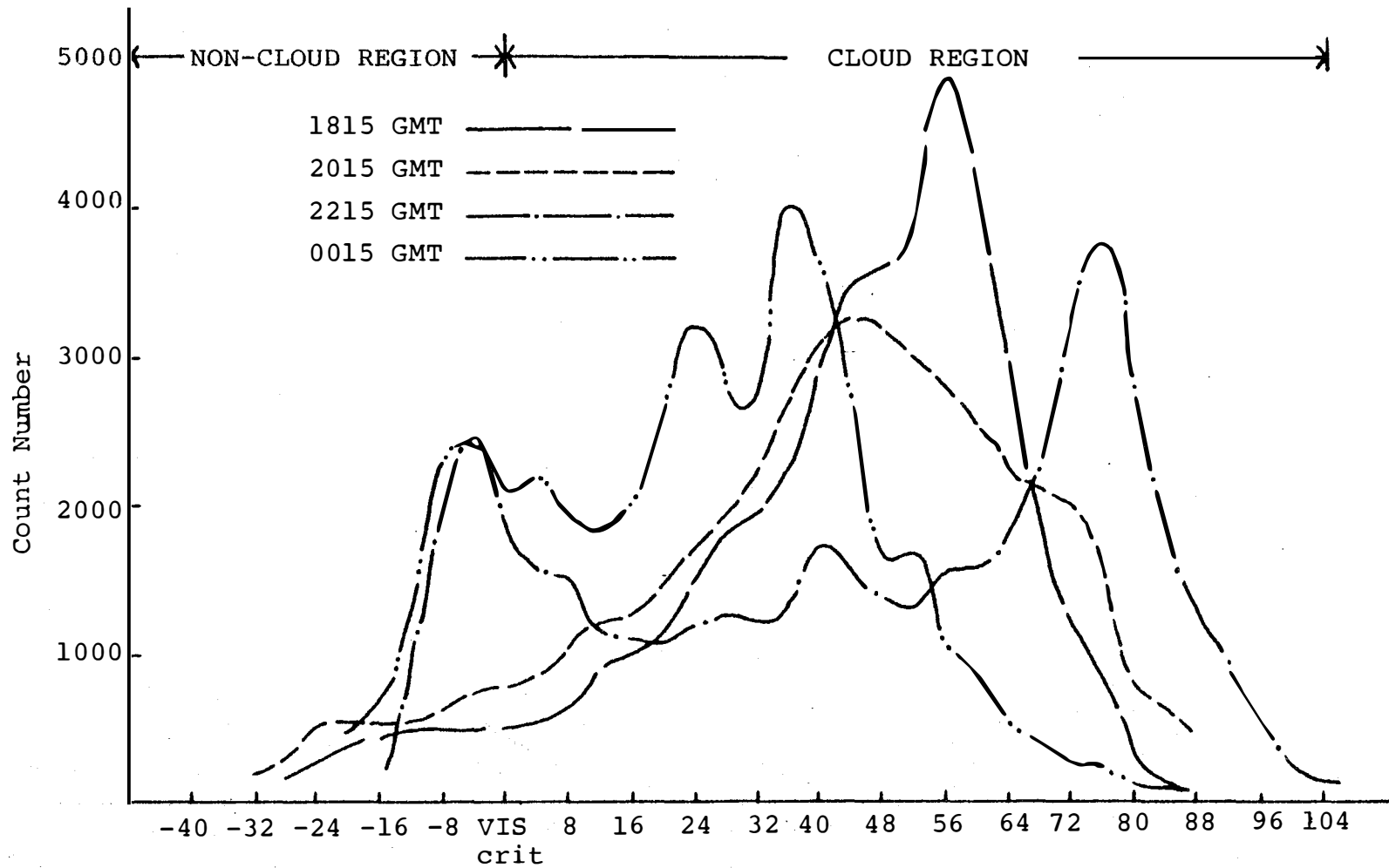
Figure 3-4 Curves of the frequency distribution of visible radiance values on 22 June.
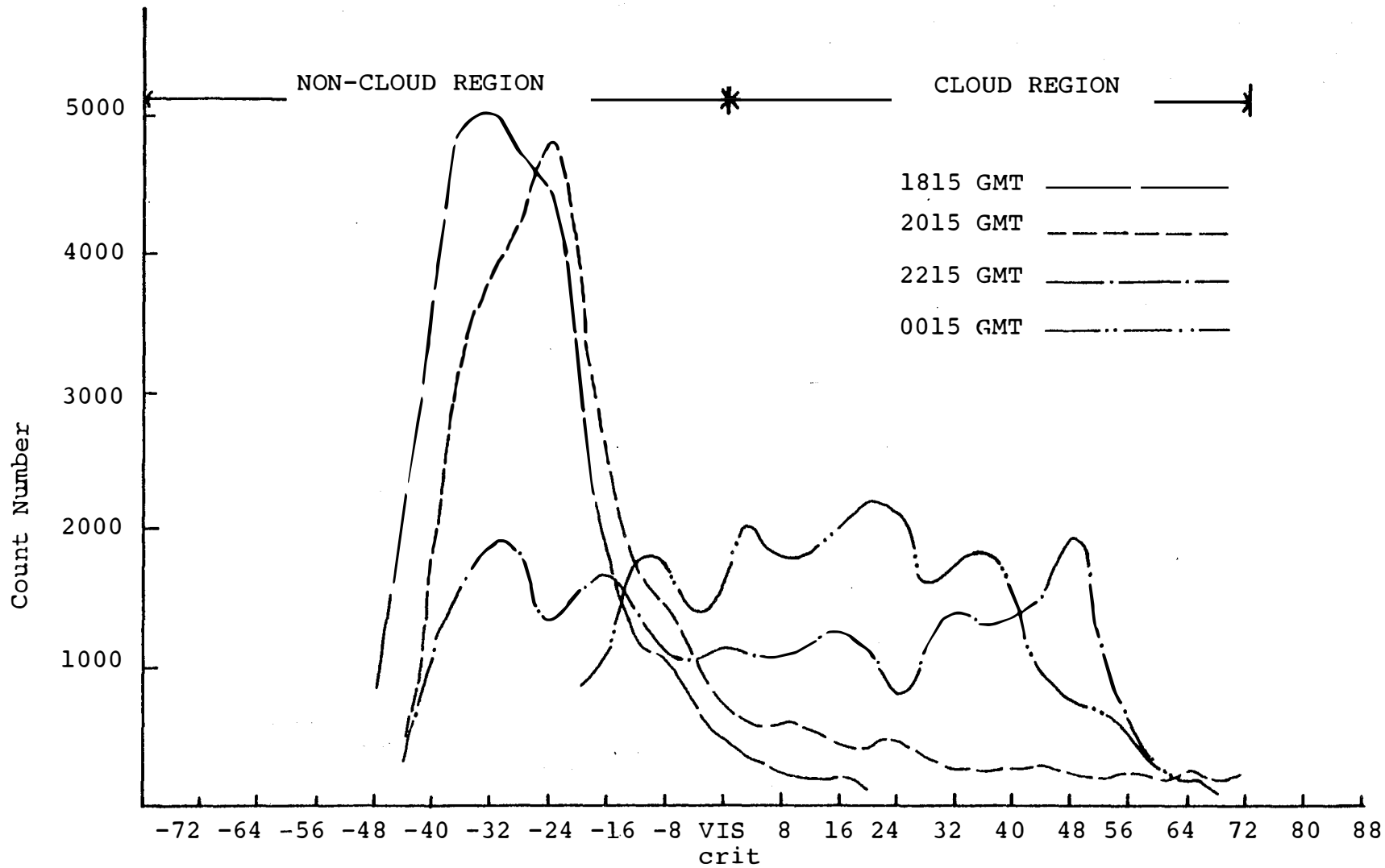
Figure 3-5 Curves of the frequency distribution of visible radiance values on 24 June.
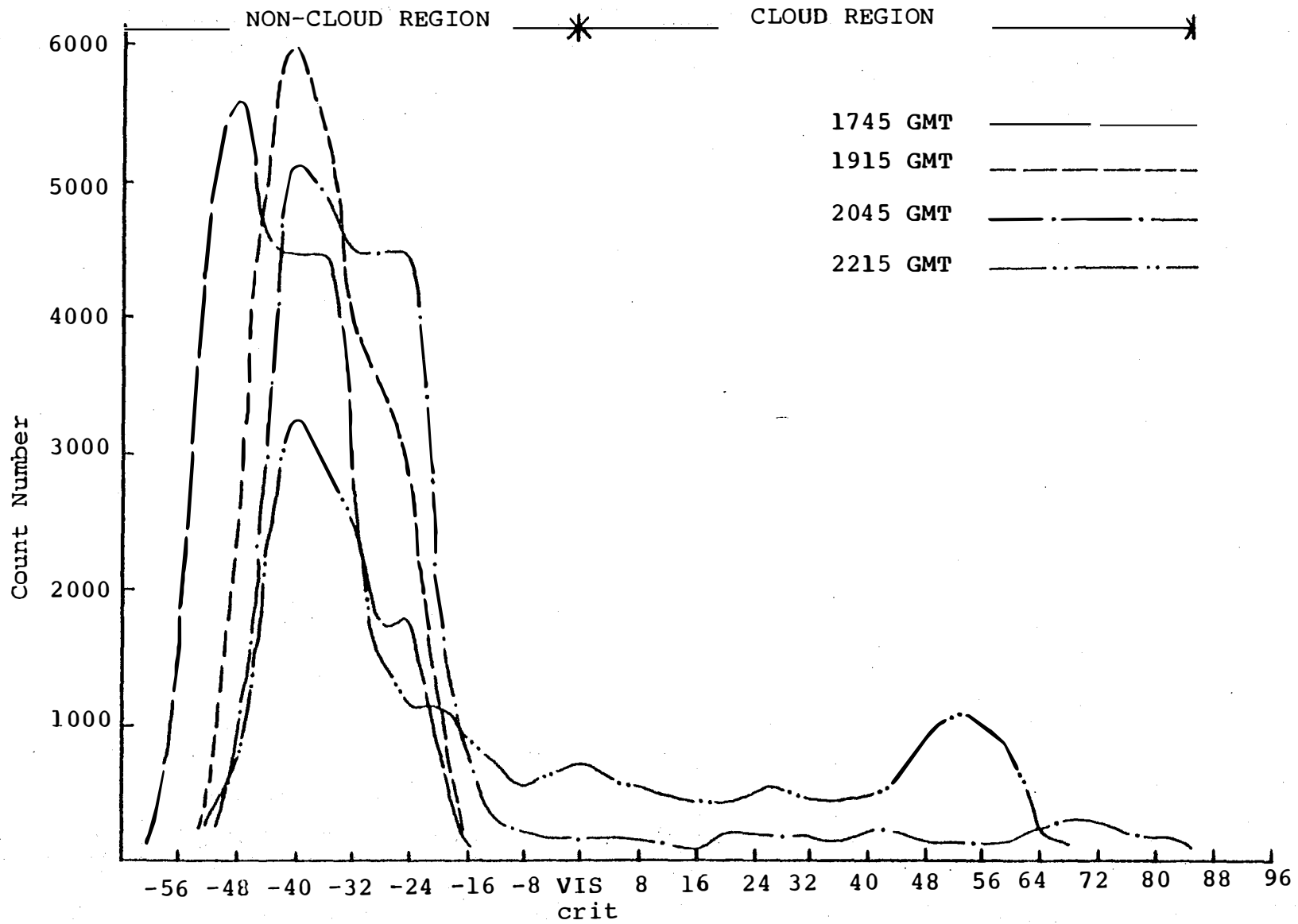
Figure 3-6 Curves of the frequency distribution of visible radiance values on 27 June.
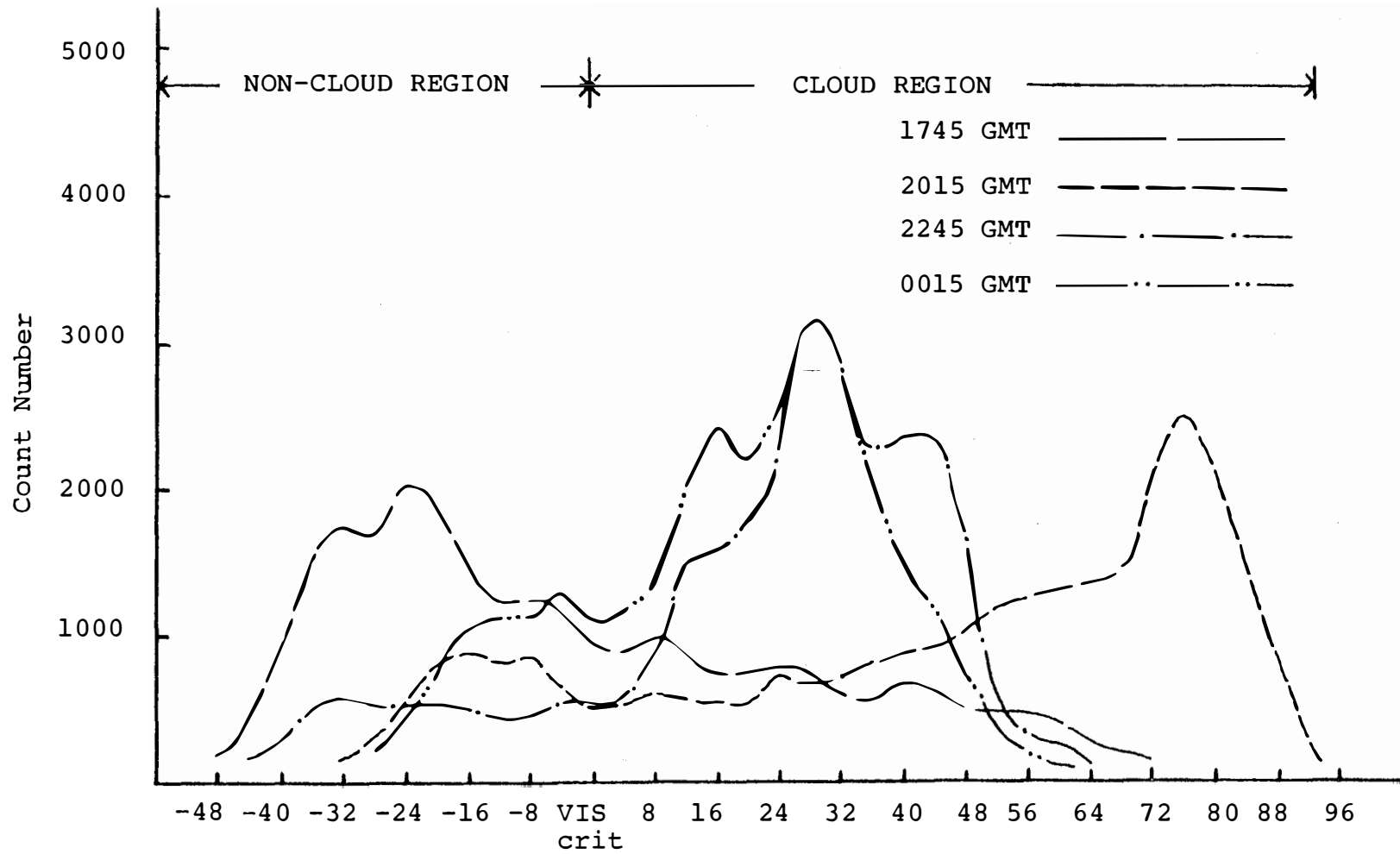
Figure 3-7   Curves of the frequency distribution of visible radiance values on 8 July.

pattern on 8 July in Figure 3-7 had a similar distribution, except for the curve at 1745 GMT, early in the day. The mode at 2015 GMT was 76 units greater than the critical value as was also observed at 2215 GMT on 22 June. At all of these times the total cloud cover was at least 80%. The most substantial rainfalls observed on the case study days occurred at these times. For both 22 June and 8 July the visible radiance values in the cloud region of the frequency distribution curve were skewed toward large positive values.

The patterns in Figure 3-5 and Figure 3-6 are similar, but very different from those on 22 June and 8 July. On these two days, the brightness frequency distributions were concentrated in the non-cloud region. The modes at 1815 and 2015 GMT on 24 June were located 32 and 24 units, respectively, below the corresponding critical values. Late that afternoon, a cloud system moved into the study area and the pattern of distribution curves at 2215 and 0015 GMT was significantly changed. The patterns on 27 June were all uniformly concentrated in the non-cloud region, with modal values at the four selected times all from 40 to 48 units below the critical visible value for each time. At all of these times, the cloud cover was less than 35%. In contrast to the 22 June and 8 July curves, the visible radiance values in the cloud region on 24 and 27 June were quite uniformly distributed over all positive values.

The precipitation analyses from the raingage network for these four days support the tentative conclusion that the visible data brightness value distribution curves are correlated with rainfall. A more detailed discussion of weather conditions will be presented in the next chapter for verification.

3.4 Comparison of Digital and Photographic Data

Because of the non-coincident viewing times for satellite imagery from GOES EAST and radiance data from GOES WEST, the averages of percent cloud cover and numbers of clouds derived from the radiance data at 15 minutes and 45 minutes after the hour were used for comparison with those derived from the imagery on the half hour. Comparisons of percent cloud cover and cloud numbers derived from satellite radiance data and from photographic imagery are shown in Table 3-2 at one-hour intervals. Although agreement between the two sets of results is generally good, there are some instances of poor agreement.

In the original analysis of the photographic imagery, the study area was divided into nine sub-areas, as shown in Figure 1-2. In the comparison presented here, these individual values of percent cloud cover were averaged to produce a more representative overall estimate. Further, the number of isolated and widespread clouds for the whole study area was obtained by adding the numbers from each

Table 3-2   Comparison of percent cloud cover and cloud numbers from satellite radiance data and photographic imagery.

DAY	Time (GMT)	Percent Cloud Cover		Number of Widespread Clouds		Number of Isolated Clouds		Total Number of Clouds	
		Radiance	Imagery	Radiance	Imagery	Radiance	Imagery	Radiance	Imagery
22 June	1830	93.5	88	2	1	6.5	42	8.5	43
	1930	89.1	84	1.5	2	12.5	92	14	94
	2030	89.2	81	1	2	5.5	100	6.5	102
	2130	68.3	59	1.5	1	28.5	105	30	106
	2230	73.6	54	2	1	16	37	18	38
	2330	–	–	–	–	–	–	–	–
23 June	0030	79.3	65	1	1	17	12	18	13
24 June	1730	6.4	32	3	3	55	247	58	250
	1830	5.4	9	2	1	59	218	61	219
	1930	13.6	23	3.5	2	61.5	284	65	286
	2030	18.7	9	4	2	70	96	74	98
	2130	25.4	20	4	3	73	70	77	73
	2230	84.8	28	1	2	20.5	27	21.5	29
	2330	76.9	49	2	3	29.5	0	31.5	3
25 June	0030	78.4	51	2	1	25	5	27	6

Table 3-2   Continued

DAY	Time (GMT)	Percent Cloud Cover		Number of Widespread Clouds		Number of Isolated Clouds		Total Number of Clouds	
		Radiance	Imagery	Radiance	Imagery	Radiance	Imagery	Radiance	Imagery
27 June	1730	0	0	0	0	0	0	0	0
	1830	0	0	0	0	0	0	0	0
	1930	0.3	5	1.5	0	2	7	3.5	7
	2030	6.6	5	2.5	1	0.5	30	13	31
	2130	17.8	11	1	1	23	66	24	67
	2230	35.2	32	2	2	21	34	23	36
8 July	1730	43.6	57	3	3	74	323	77	326
	1830	50.1	53	5	3	61	256	66	259
	1930	58.4	61	4	2	35.5	247	39.5	249
	2030	82.8	73	1	1	22	191	23	192
	2130	90.9	79	1	1	24	176	25	177
	2230	81.9	83	1	1	24	78	25	79
	2330	79.2	70	1	1	33	80	34	81
9 July	0030	80.2	73	1	2	16	73	17	75

sub-area. Table 3-2 compares the percent cloud cover and cloud number results derived from these two sources.

The agreement of percent cloud cover between the two sets is good, except for a few cases on 24 June. Because the percent cloud cover from photographic imagery was estimated visually, it was difficult to maintain as consistent an accuracy as with percent cloud cover derived from radiance data. Figure 3-8 shows that the trends of percent cloud cover from radiance data and photographic imagery have similar patterns. In general, the difference in percent cloud cover estimated from these two data sets was approximately 5% to 10%. The most difficult estimates of percent cloud cover occurred at times when isolated, cluster and line clouds were predominant. This situation was particularly true on 24 June, where the differences in Table 3-2 are very noticeable.

The agreement in Table 3-2 in number of widespread clouds between these two data sets is seen to be much better than that for isolated clouds. Especially on 24 June, when isolated clouds dominated, the agreement was very poor. A detailed study of the results on this date points to an explanation. The computer cloud summary program treated many small clouds as a single large cloud as long as the individual clouds were linked together at even one point. As a result, the number of widespread clouds was one or two more than the value derived form the
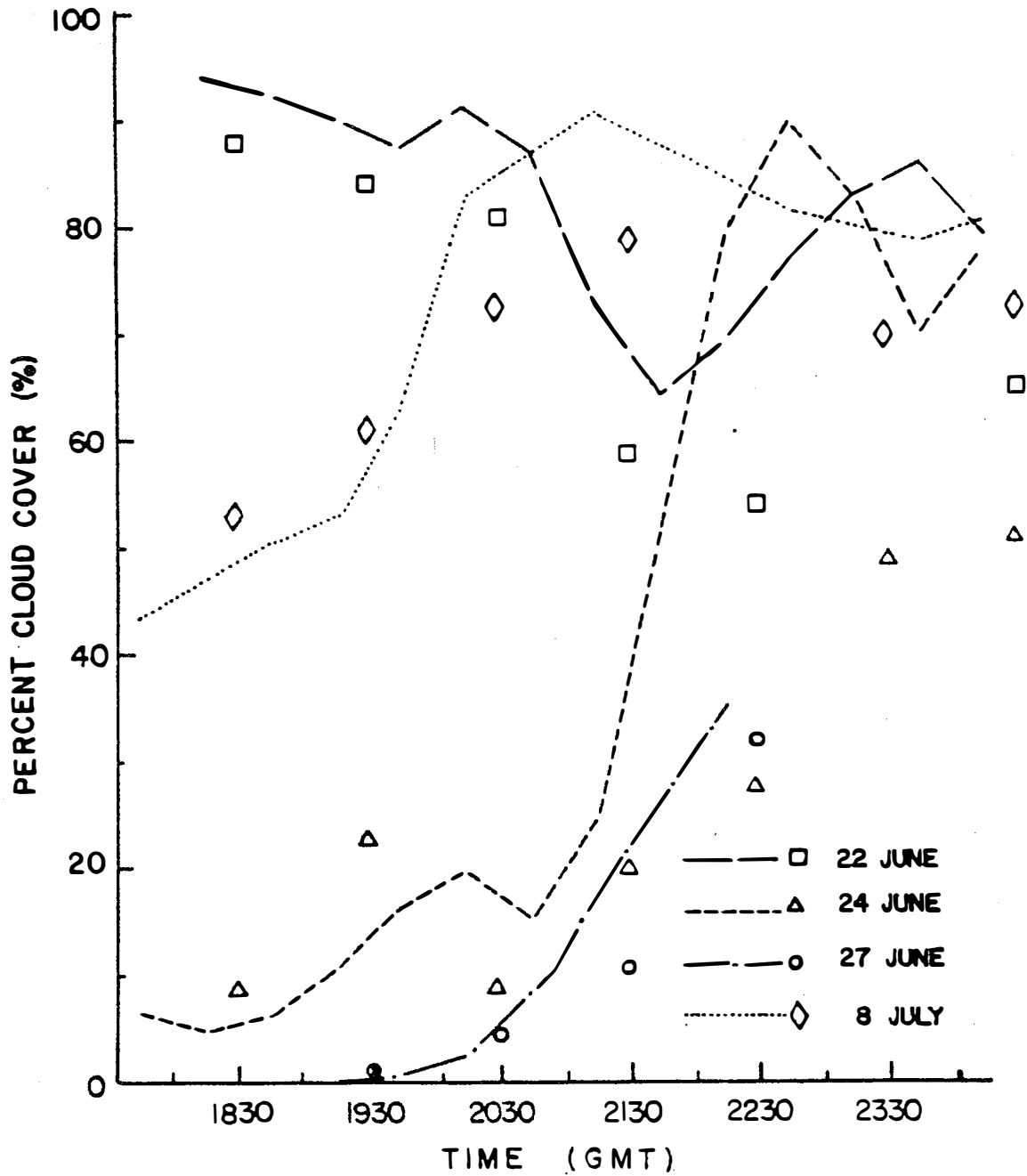
Figure 3-8   Variation of percent cloud cover from radiance
data and photographic imagery. The curves are
the same as Figure 3-1, while the symbols are
from photographic imagery.

imagery, while the number of isolated clouds was much less than that from imagery. Early on 8 July, the number of isolated clouds differed for the same reason, although the numbers of the widespread clouds were nearly equal.

Another factor influencing the accuracy of these results was the variation in solar zenith angle, which increased to 50° after 2230 GMT; consequently, the brightness of the scene was significantly reduced. Under these conditions, fewer small isolated clouds could be distinguished from the underlying surface in the photographic imagery. The late afternoons of 24 June and 8 July are good examples of this problem.

In conclusion, the results derived from radiance data analyzed by the summary program are considered to be more accurate and quantitative. However, analysis of the imagery can be of assistance to the study of radiance data sets, especially in providing a large-scale view of the overall synoptic pattern existing at a given time.

3.5 Albedo

Albedo is the ratio of the radiation reflected by a surface to the radiation incident upon it, and is normally expressed as a fraction, ranging from 0 for a perfect absorber to 1 for a perfect reflector. Some representative albedo value ranges for various surfaces given in the Smithsonian Meteorological Tables (List, 1966) are:

0.03 to 0.10 for rivers and seas, 0.07 to 0.20 for ground, and 0.05 to 0.84 for clouds. A calibration computer program was obtained for the basic albedo value determination (Smith, 1977), and was applied to the determination of albedo values in the same manner as utilized in a previous case study (Jurica and Chi, 1979).

The visible radiance data which represent the albedo over the observed area, have been converted to albedo values utilizing the curve of Figure 2-1 as the basis of the technique. On the four case study days to be analyzed, the smallest solar zenith angle of approximately 9.0° occurred at 1845 GMT. Because the albedo value is inversely proportional to the cosine of solar zenith angle, a difference of only 1% existed between albedos at 1845 GMT each day and the values for zero solar zenith angle given in Figure 2-1. It was assumed that all the small isolated cumulus used to establish the critical brightness value had similar cloud properties and their albedo values did not change with time. Therefore, all the critical visible values should have corresponded to a certain albedo value. Curves of visible radiance data versus albedo were derived based on this assumption for different zenith angles and are shown in Figure 3-9.

Figure 3-10 shows an example of the enhanced visible and infrared ADVISAR images at 2115 GMT on 27 June 1977. The albedo values corresponding to the colors of the
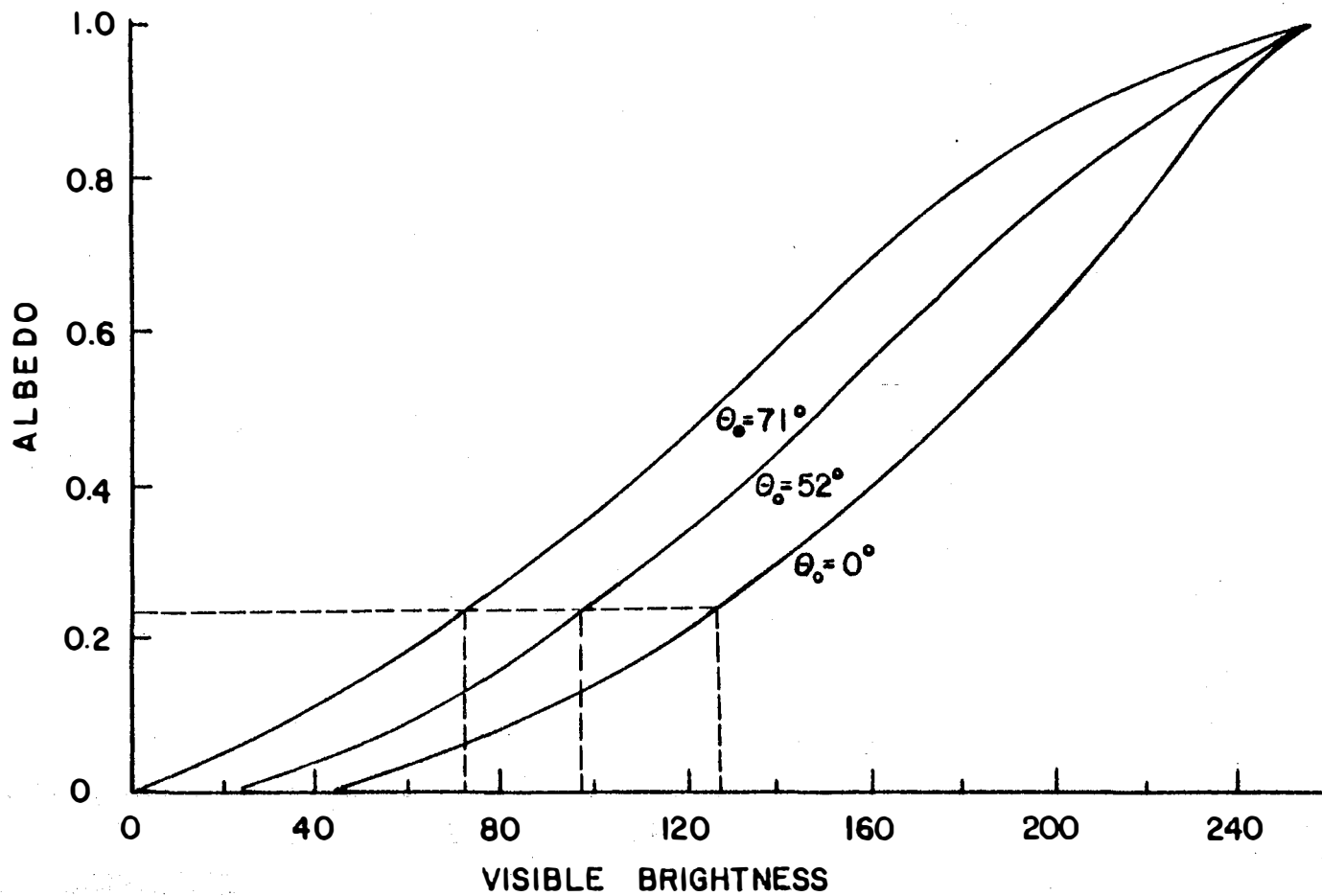
Figure 3-9 Albedo curves for solar zenith angles: 0^O(VIS$_{crit}$=128), 52^O(VIS$_{crit}$=96) and 71^O(VIS$_{crit}$=72).
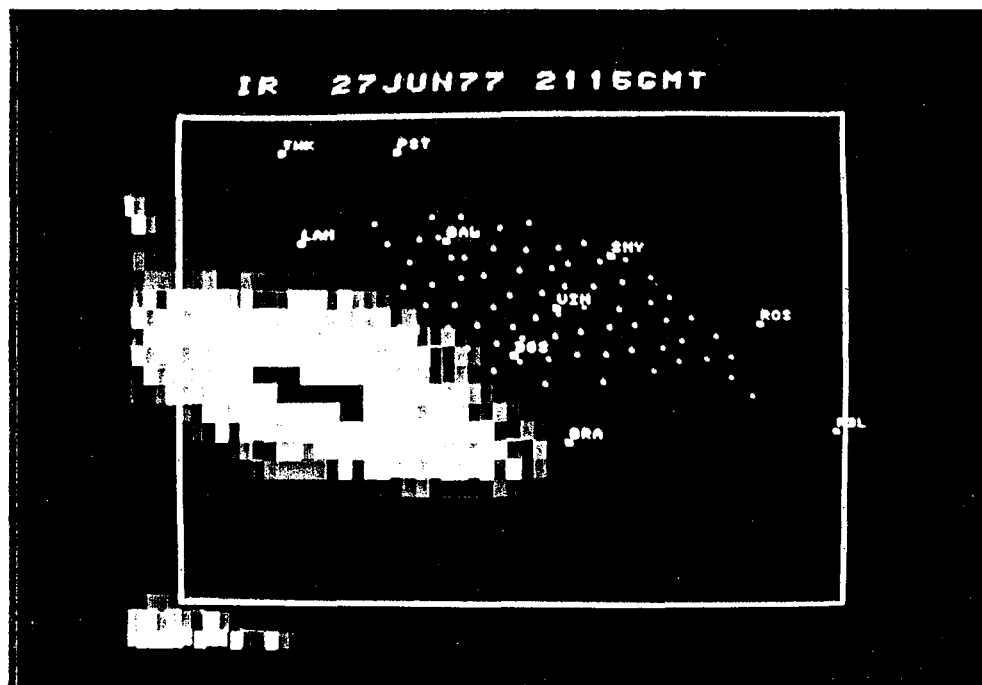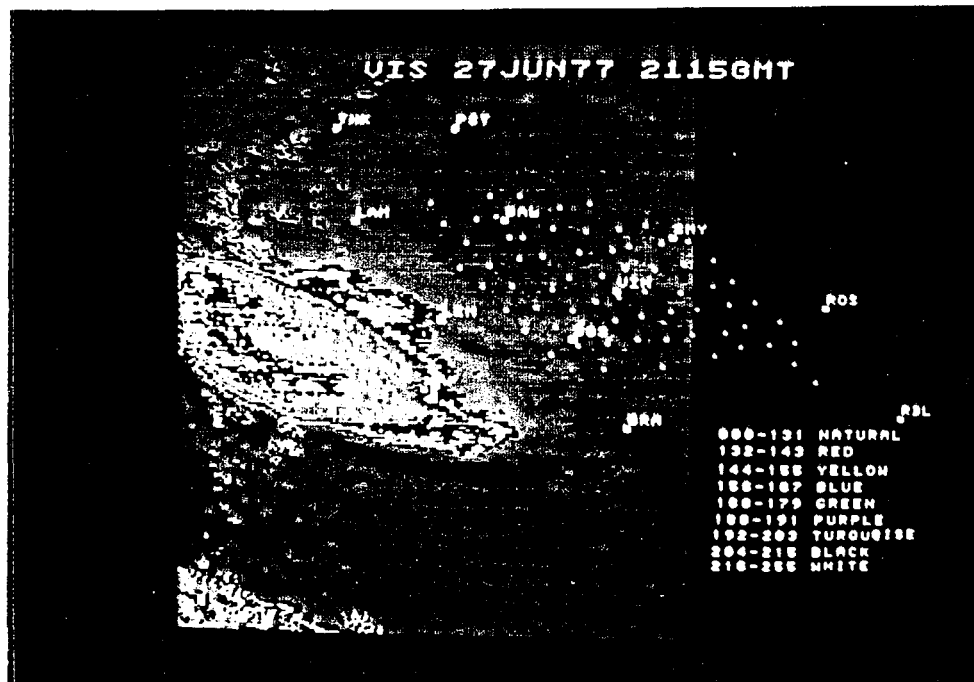
Figure 3-10 Enhanced visible and infrared pictures at
2115 GMT 27 June 1977. The correspondence
between the colors and albedo and cloud top
temperature are given in the text.

visible picture were taken from Figure 3-9, and are as follows: red (.25 - .30), yellow (.31 - .37), blue (.38 - .44), green (.45 - .50), purple (.51 - .58), turquoise (.59 - .66), black (.67 - .76), white (larger than .77). The same color sequence given in Figure 2-2 was utilized in the infrared picture, and corresponds to cloud top temperatures as follows: red (0 to -9 C), yellow (-10 to -19 C), blue (-20 to -29 C), green (-30 to -39 C), purple (-40 to -49 C), turquoise (-50 to -59 C), black (-60 to -69 C), white (less than -70 C). A storm cell moved into the study area from the west during the late afternoon of 27 June. Because the storm was rapidly developing at 2115 GMT, the gradients of both brightness and cloud top height were very sharp near the edge of the storm, especially along the southern edge. The brightness near the center of the storm was strong and the height of the storm in the central portion was approximately 15 km, corresponding to cloud top temperatures from -60 to -70 C. These pictures provide a good example of the value of enhancement for location of particulary active convective areas within a cloud system.

CHAPTER 4

COMPARISON OF SATELLITE-DERIVED RESULTS
WITH RADAR AND RAINGAGE MEASUREMENTS

The cloud characteristics derived from the satellite radiance data and presented in the last chapter are discussed from several points of view in this chapter. The relation between the satellite radiance data and large-scale, mesoscale and small-scale weather conditions are included in this discussion. By mesoscale, or subsynoptic scale, is meant a spatial scale of several hundred kilometers and a temporal scale of several hours. The comparison with weather conditions and with other data sources comprises the main portion of the verification of the satellite-derived results presented in this chapter. Utilizing the available satellite, radar and precipitation data, a comparison was made by placing the three different data sources into a common coordinate system (Reynolds and Smith, 1979). The reference coordinates have been selected to be the rectangular array of visible satellite radiance measurements used in this study. The objective of this comparison was to enhance understanding of (a) the structure of the convective clouds (b) the relation between organized mesoscale features and the synoptic scale (c) storm development processes, and (d) precipitation mechanisms on the four case study days.

Both PPI (Plan Position Indicator) and RHI (Range Height Indicator) digital radar displays were employed in this investigation. Vertical radar profiles were utilized to study the structure of the storm cells selected for analysis. In addition, the RHI displays provided information on the internal structure of clouds for which cloud top temperatures were obtained from the satellite infrared radiance data. Finally, the comparison of the several data sources was completed by integrating the three sets of results.

Each of the following four sections presents a discussion of one of the case study days. On the first two days, 8 July and 22 June, signigicant precipitation events occurred, while little or no precipitation was detected by the raingage network on the remaining two case study days, 24 June and 27 June. The discussions consider how the large-scale, mesoscale and small-scale weather conditions were related and how the technique of composite presentation of several data sets was applied to each of the study cases. Finally, the summary of the results demonstrates the increased information derived from such a method of analysis.

4.1 Case Study of 8 July 1977

The 8 July case study offered an excellent opportunity for the integration of radar and precipitation data

together with visible and infrared satellite data. The
discussion of this case study concentrates on the precipi-
tation events and comparisons between satellite and radar
data. Two times, 1942 and 2018 GMT, have been selected
for a discussion of RHI cross-sections which passed
through precipitation cells. In addition, a discussion of
the synoptic, mesoscale and small-scale features is
included.

4.1.1 Review of Synoptic Conditions

Two weak cold fronts extended from the northeastern
United States through the central United States into Texas
at 1500 GMT (Figure 4-1a). The cold fronts moved slowly
eastward and passed through the study area at 1800 GMT,
just before heavy rainfall was detected in the raingage
network (Figure 4-1b). During the next three-hour inter-
val, the fronts moved eastward (Figure 4-1c) and left the
study area by 0000 GMT 9 July (Figure 4-1d), as the
rainfall subsided.

A distinct ridge and trough pattern was present at
500 mb on 8 July (Figure 4-2a and b). The ridge passed
through the New Mexico area at 1200 GMT and remained
stationary until 0000 GMT 9 July. Cold air advection
occurred within the study area at the 500-mb level. The
5880 gpm contour passed through the study area at 1200 GMT
8 July and had moved to the south away from the study area
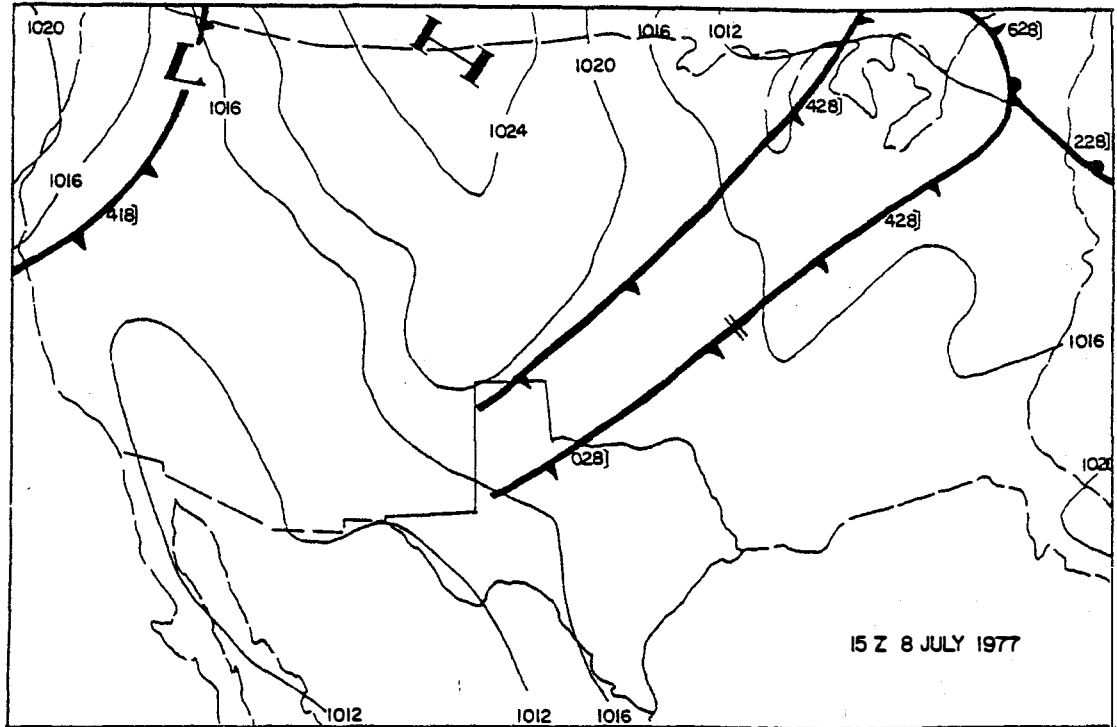
(a)
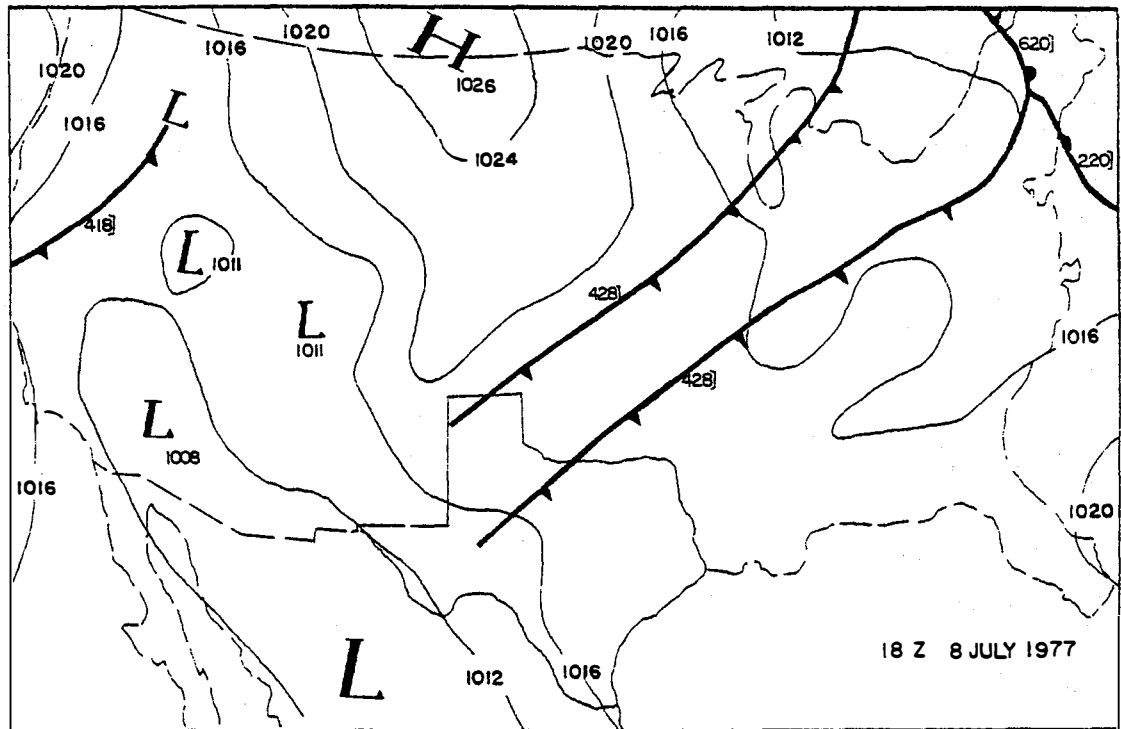
(b)

Figure 4-1 Surface synoptic charts on 8 July 1977.

(c)

21Z 8 JULY 1977

(d)
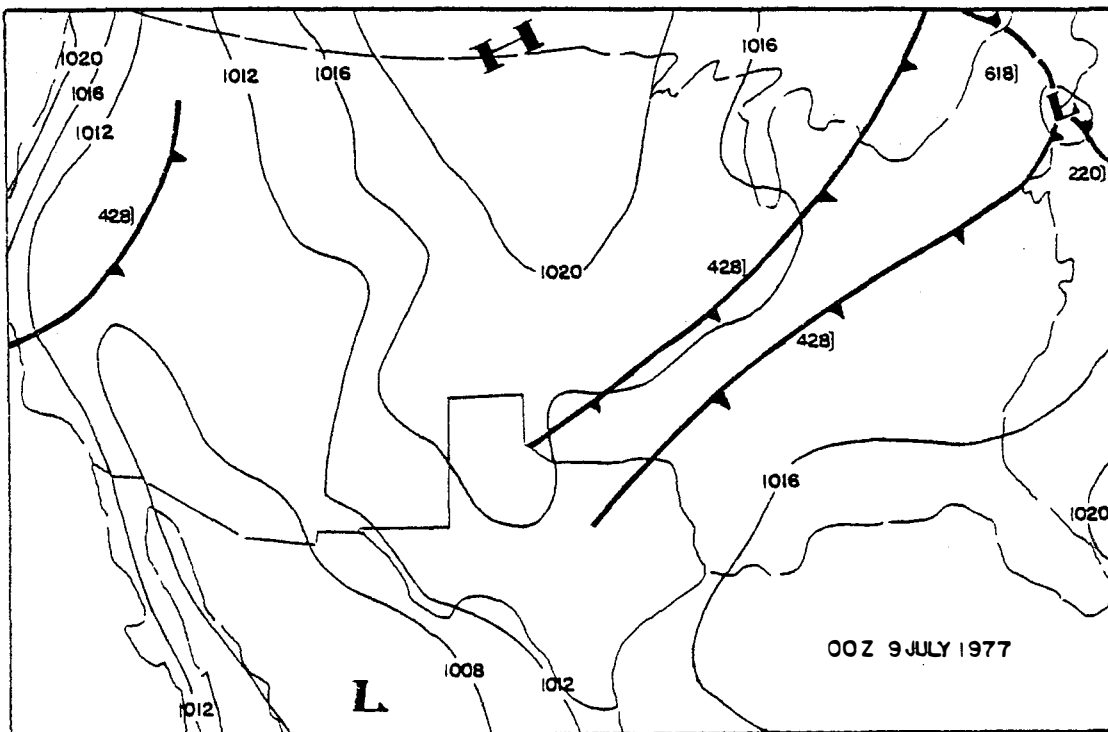
00Z 9 JULY 1977

Figure 4-1   Continued
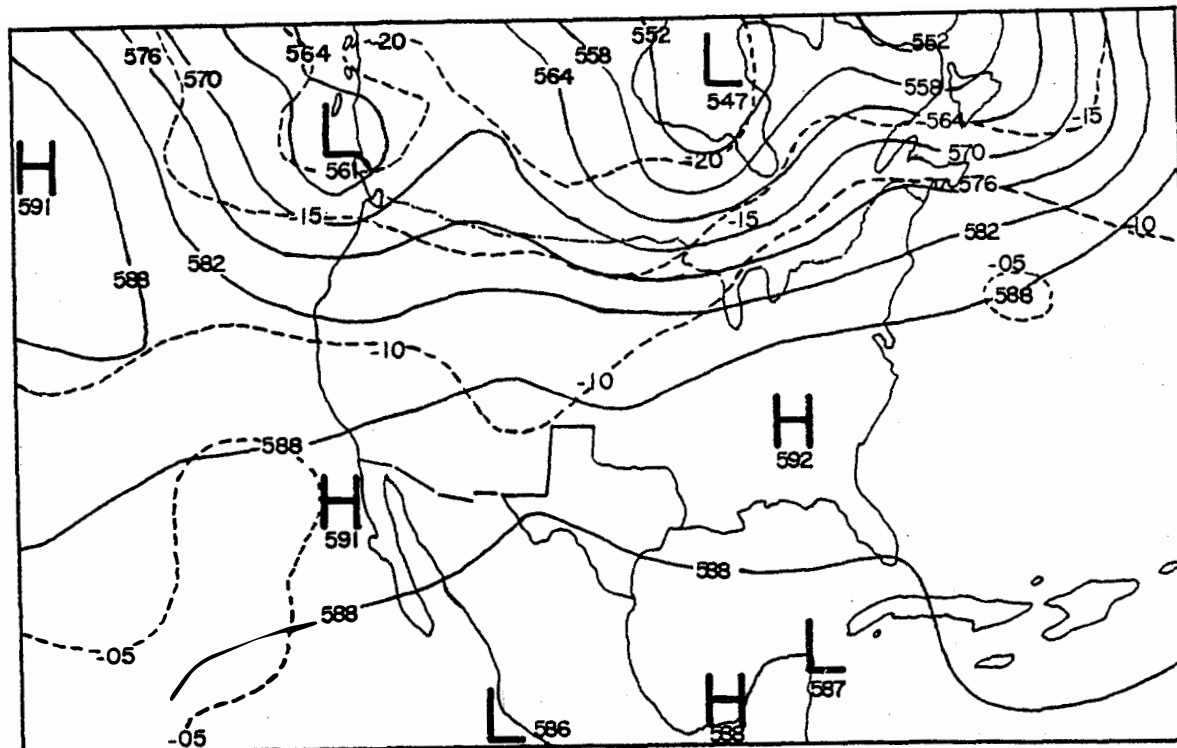
(a) **500 mb**   **12 Z**   **8 JULY**   **1977**
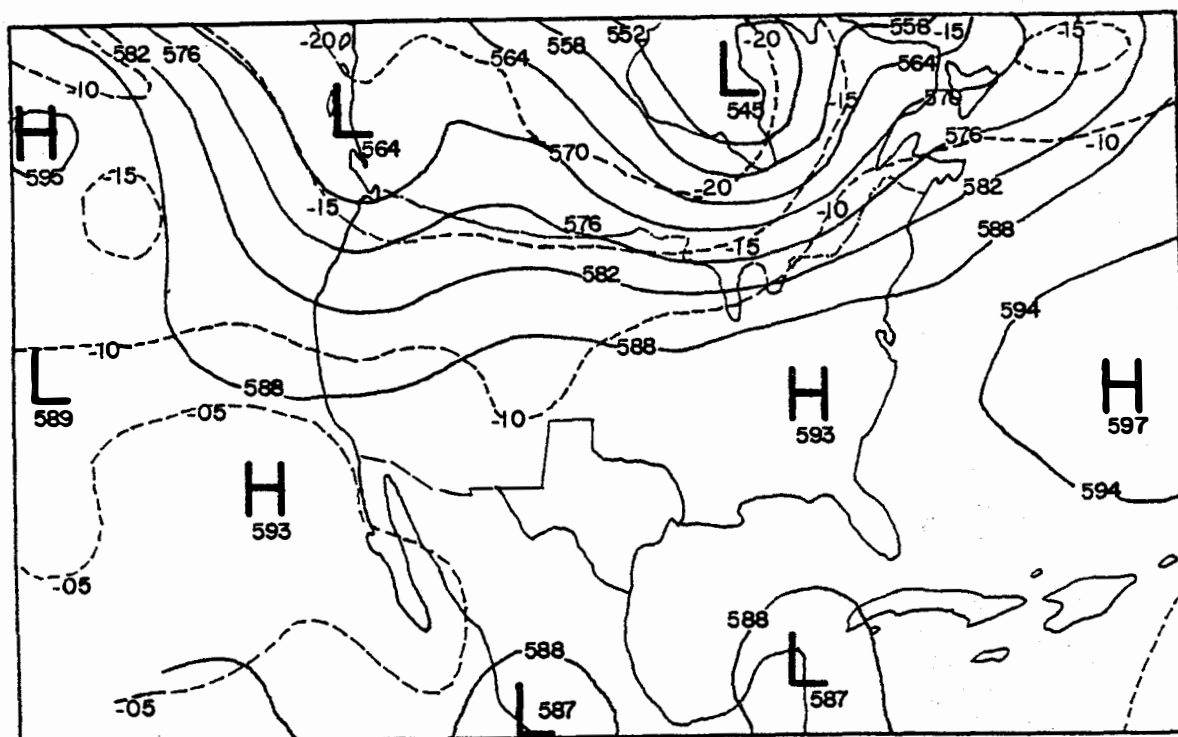
(b) **500 mb**   **00 Z**   **9 JULY**   **1977**

Figure 4-2 500-mb charts on 8 July 1977. Contours
(solid lines) are given in decameters
and isotherms (dashed lines) are given
in Celsius degrees.

by 0000 GMT 9 July.

4.1.2 Subsynoptic Features

4.1.2.1 Precipitation Analysis

The recording raingage network in 1977 consisted of
59 stations and recorded rainfall to the nearest one-
hundredth inch for every 15-minute interval. The precipi-
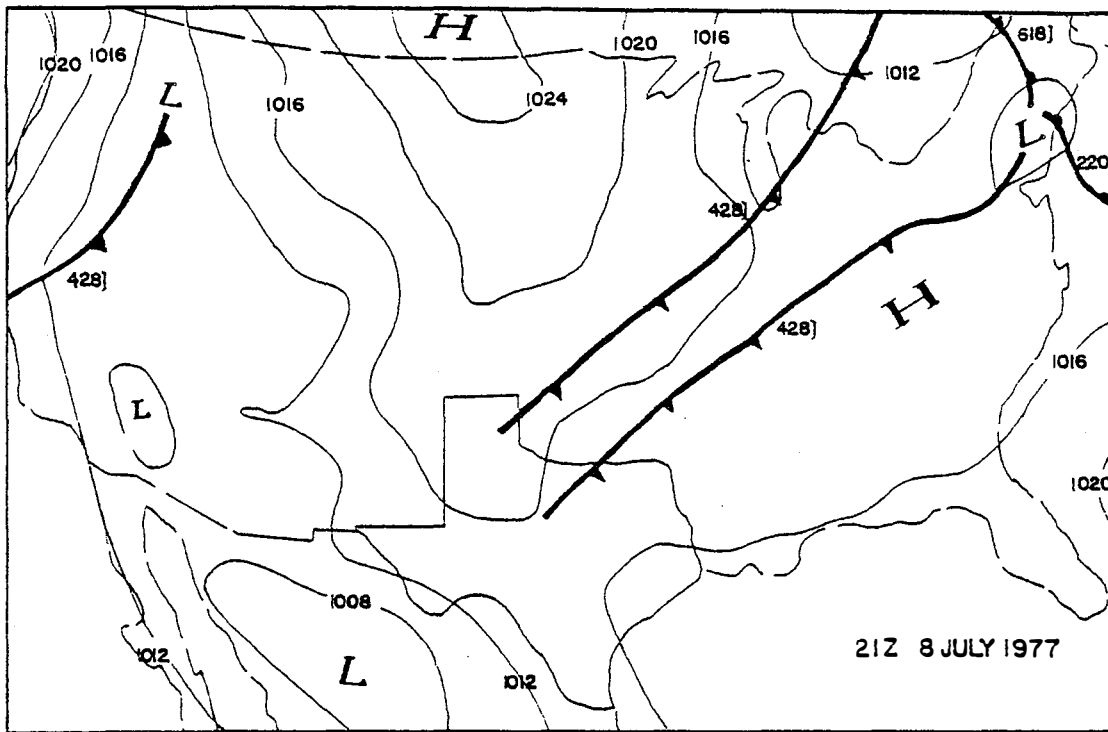tation analysis indicated that the precipitation on 8 July
was concentrated in the afternoon, from 1830 to 2045 GMT,
when a line of intense rainfall formed in association with
the passage of the two cold fronts through the raingage
network. The rain subsided within the raingage network
soon after the cold fronts moved out of the study area.
The total precipitation volume was derived by first
constructing a network of triangles with the raingages at
each vertex, then averaging rainfall amount over each
triangle and finally summing up over the entire network
(Haragan, et al., 1979). The variation with time of total
precipitation volume on 8 July is shown in Figure 4-3.
The value plotted at a given time represents the rainfall
occurring during the preceding 15-minute interval. The
spatial pattern of total rainfall from 1800 to 0000 GMT
9 July (Figure 4-4) shows that the heavy rainfall areas
were located in a band stretching from southwest to
northeast, with many stations collecting over 1.5 inches
during this six-hour interval. The broken isohyet in
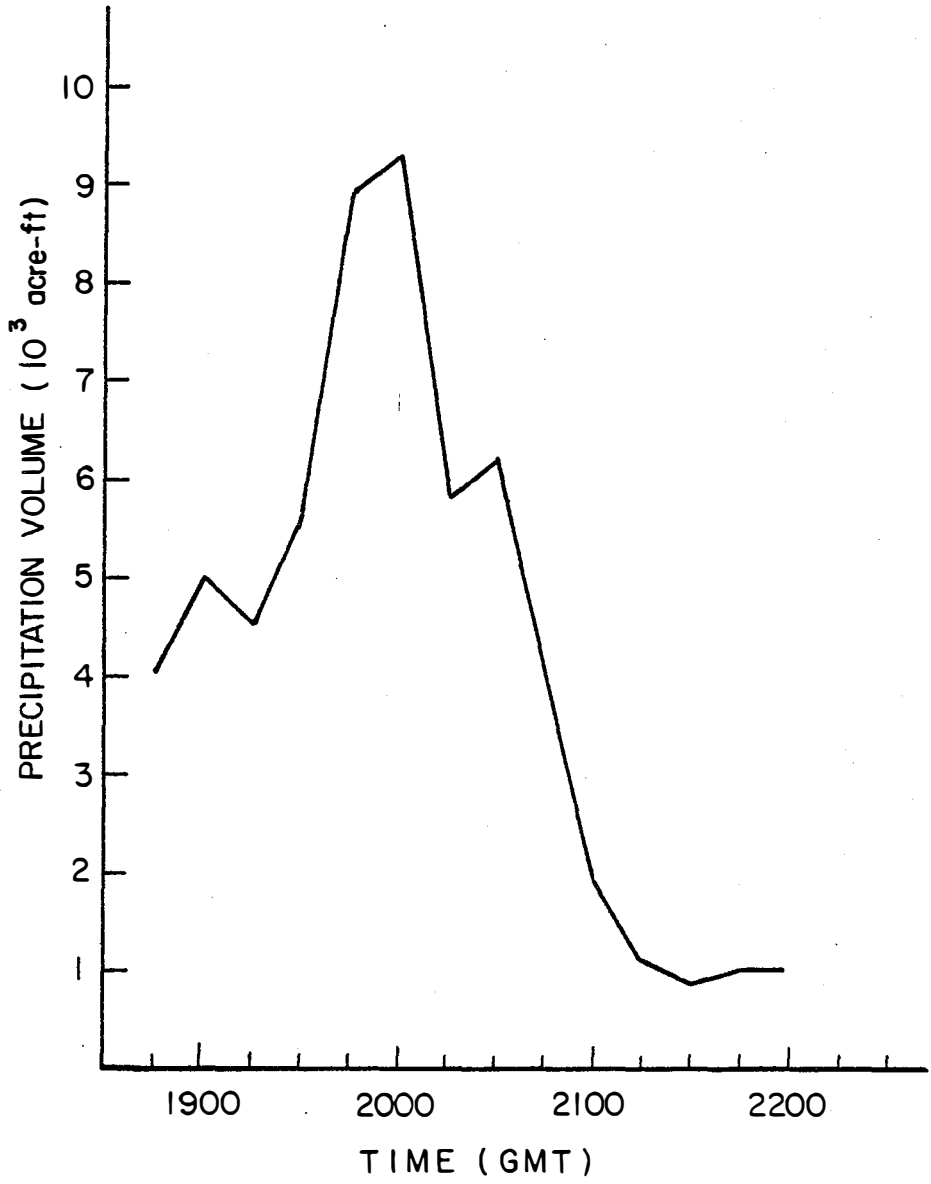
Figure 4-3   Variation of total network precipitation with time on 8 July 1977.
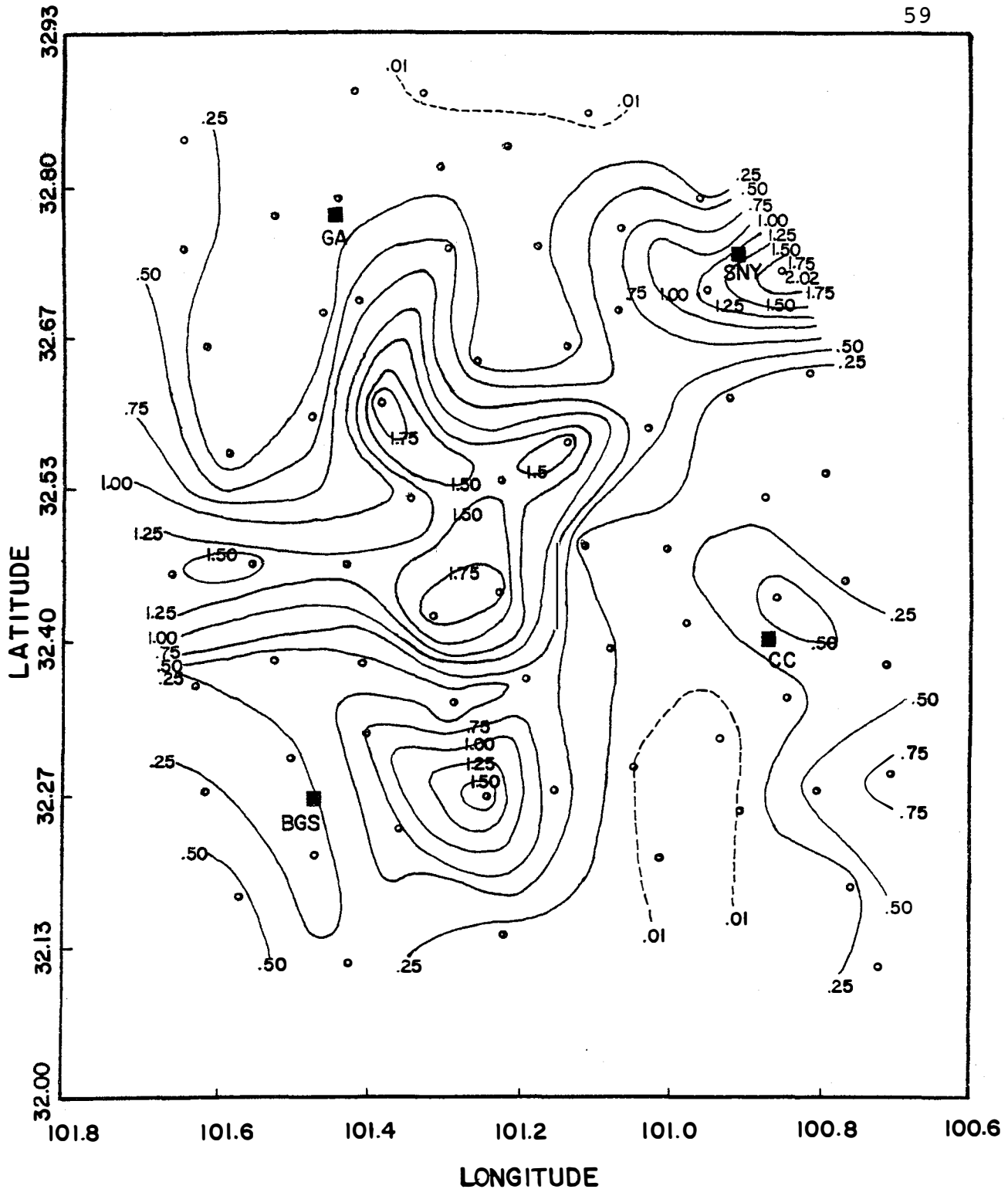
Figure 4-4   Precipitation analysis of the total precipitation
             from 1800 GMT 8 July to 0000 GMT 9 July 1977.
             The isohyets are labelled in inches.

Figure 4-4 represents a rainfall of 0.01 inch and the solid contours are given for every 0.25 inch. The total surface water produced by precipitation was found to be 66,095 acre-ft, the heaviest rain among four case study days.

4.1.2.2 Mesonetwork Observations

Measurements gathered with the mesoscale surface network (Scoggins, et al., 1977) indicated that the temperature patterns were well correlated with the occurrence of convective activity with a center of minimum temperature matching the strong radar echoes, as discussed below. The analysis of surface parameters showed good correspondence with the timing of precipitation development inside the study area from 1800 to 2100 GMT. Large centers of surface velocity convergence occurred prior to 2100 GMT, followed by strong divergence and eventual dissipation. Further, strong upward vertical motion existed 50 mb above the surface prior to 2100 GMT and downward motion thereafter. And also, surface moisture convergence prior to 2100 GMT showed maxima in regions of strong convection. Finally, the horizontal mass convergence in low levels increased between 1500 and 1800 GMT as thunderstorm development occurred over the study area.

4.1.2.3 Discussion of Snyder M-33 Radar PPI Displays

The highly modified M-33 radar located at Winston

Field in Snyder, Texas, provided the digital data for this case study day. The M-33 radar was operated by MRI at two wavelengths, one S-band (9.1 cm) and one X-band (3 cm) (Table 4-1). Both radars were operated in a continuous volume scan mode recording digitized data at azimuth intervals of 1° and elevation intervals of 1.5°. The S-band radar was considered the primary data acquisition radar and was operated whenever echoes existed in or near the operational area. The X-band radar was more subject to attenuation and, consequently, was operated only when significant echoes existed close to the radar site. The normal volume scan included 12 elevations up to 18° and required 5 minutes to complete. On some occasions, however, the scan was intentionally limited to less than 18°; on these occasions, the volume scan duration was less than 5 minutes (Mulvey, 1978).

Figure 4-5 shows PPI plots from the M-33 radar on 8 July 1977. The borders of the raingage network and satellite study area are drawn over the radar echo pattern. The displays show that strong reflectivity values were observed within the raingage network from 1800 until 2200 GMT. The precipitation analysis indicated several isolated storm cells over the network during the first hour of the study period. The strong echo area in which reflectivity was larger than 45 dBz was easily identified

Table 4-1

HIPLEX radar characteristics
Snyder, Texas - 1977

	S-band	X-band
Frequency	3300 MHz	9250 MHz
Peak power	850 Kw	250 Kw
PRF	900 sec^{-1}	Phase locked to S-band
Transmitted pulse length	1.3 μs	0.25 μs
3 db antenna beam width	1.6°	1.1°
Receiver type	Logarithmic	Logarithmic
MDS (nominal)	-105 dbm	-110 dbm
Dynamic range	80 db	80 db
Processing	Digital linear power averaging	Digital linear power averaging
Bin spacing	1 μs	1 μs (average of 5 0.25 μs bins)
Number of bins	1024	1024
Recording medium	1600 BPI digital tape	1600 BPI digital tape

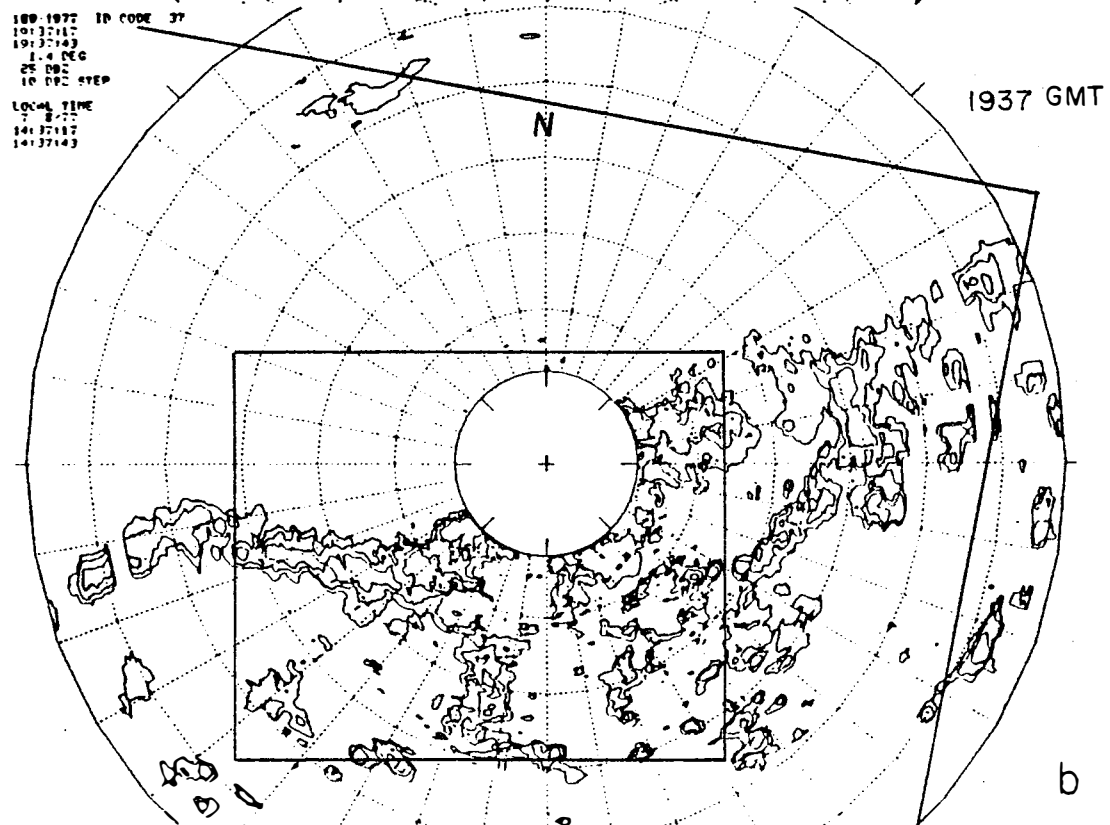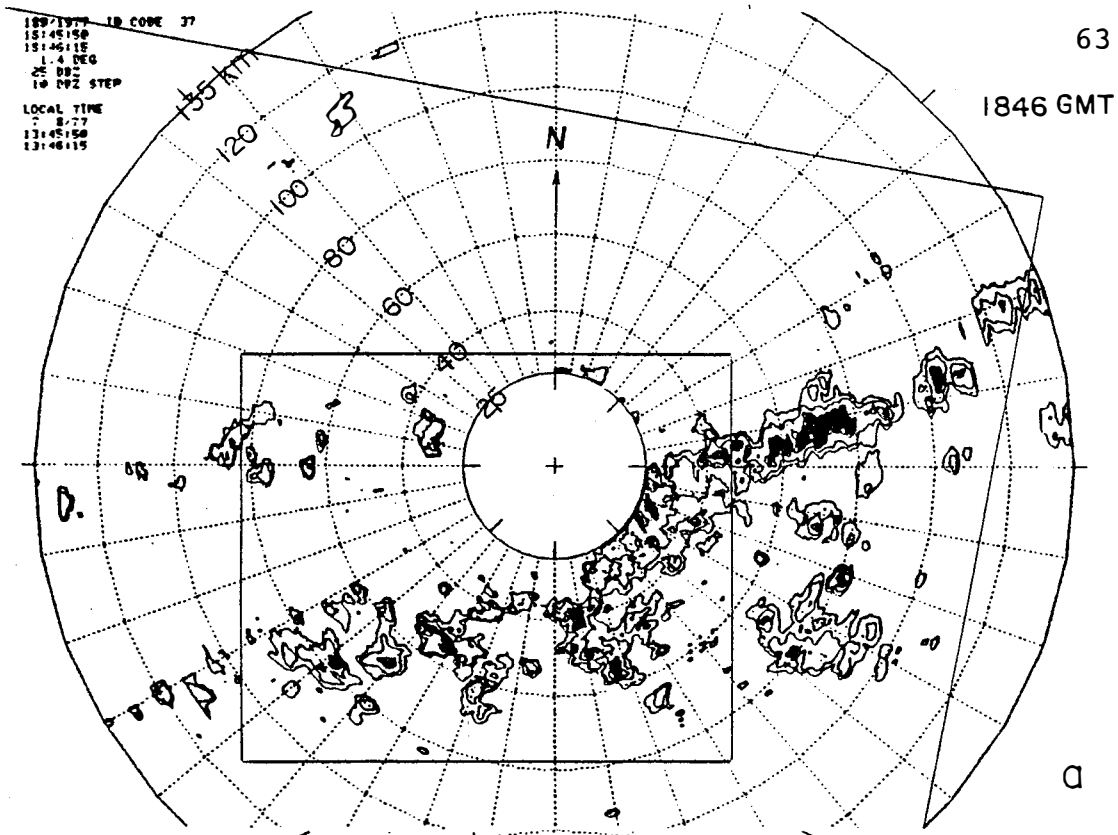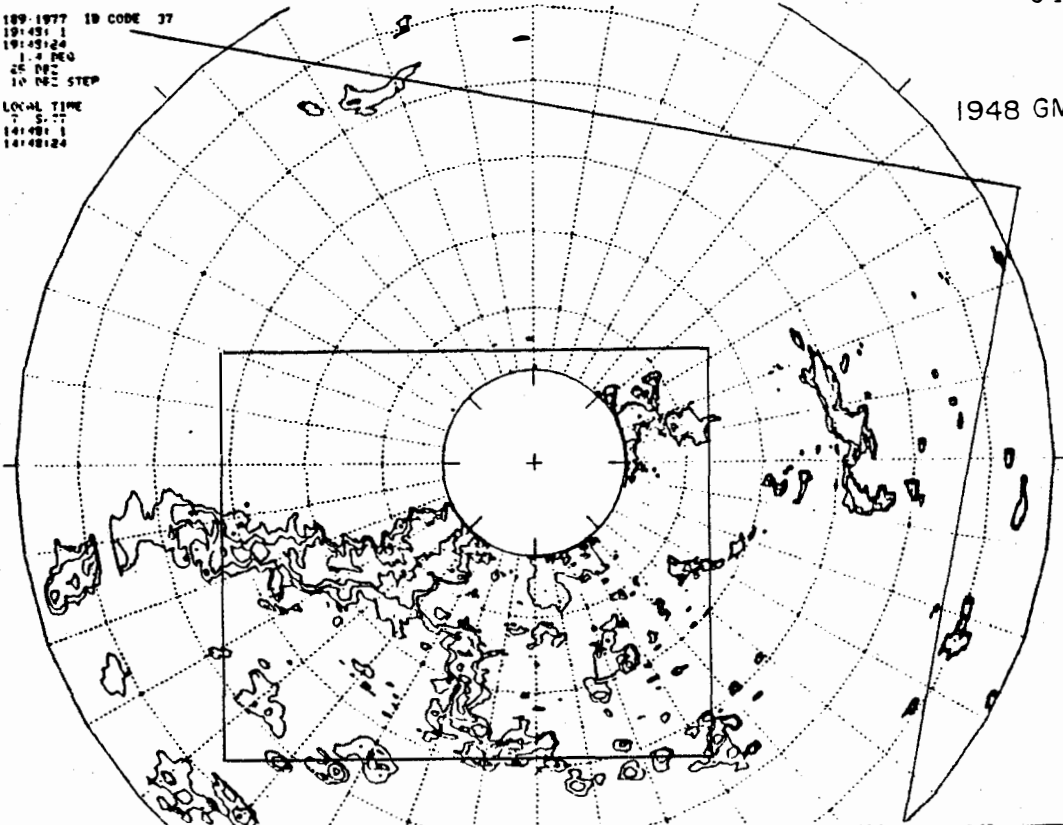Figure 4-5   PPI displays on 8 July 1977 from the M-33 radar
at Snyder.   The outer boundary shows the study
area, while the inner box is for the raingage
network.   The echo threshold is 25 dBz and dark
solid areas represent reflectivities greater
than 45 dBz.

1948 GMT

C

2018 GMT

N

d
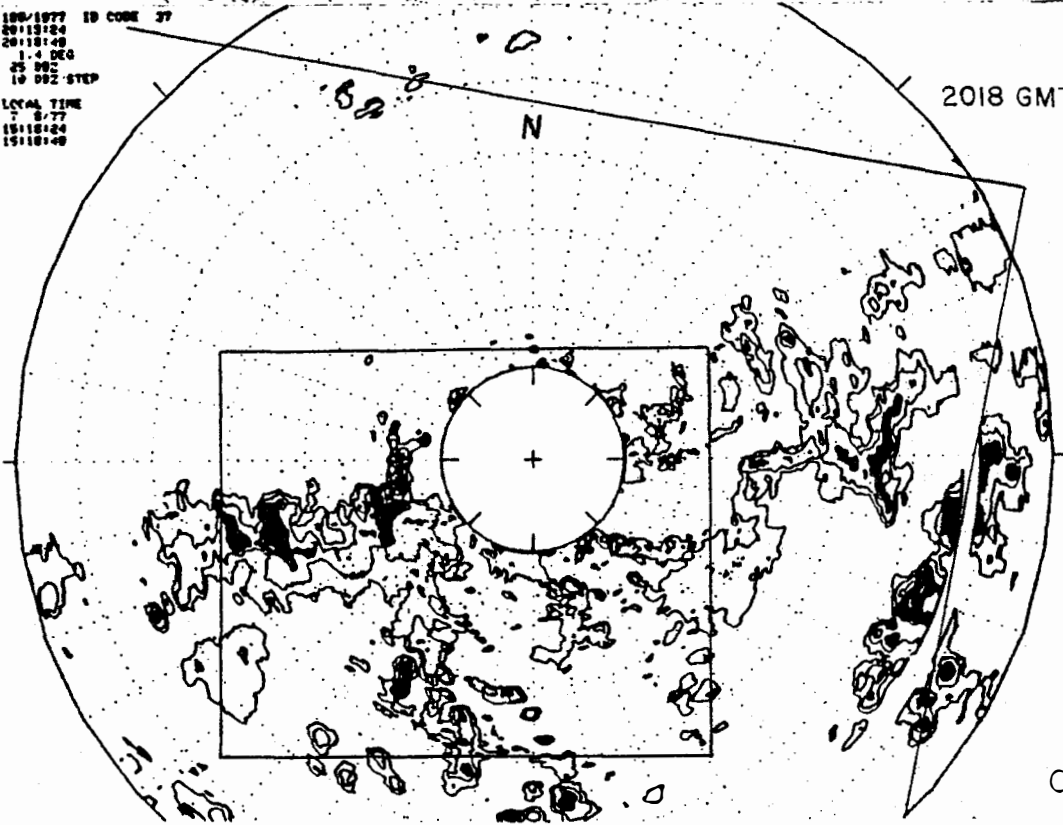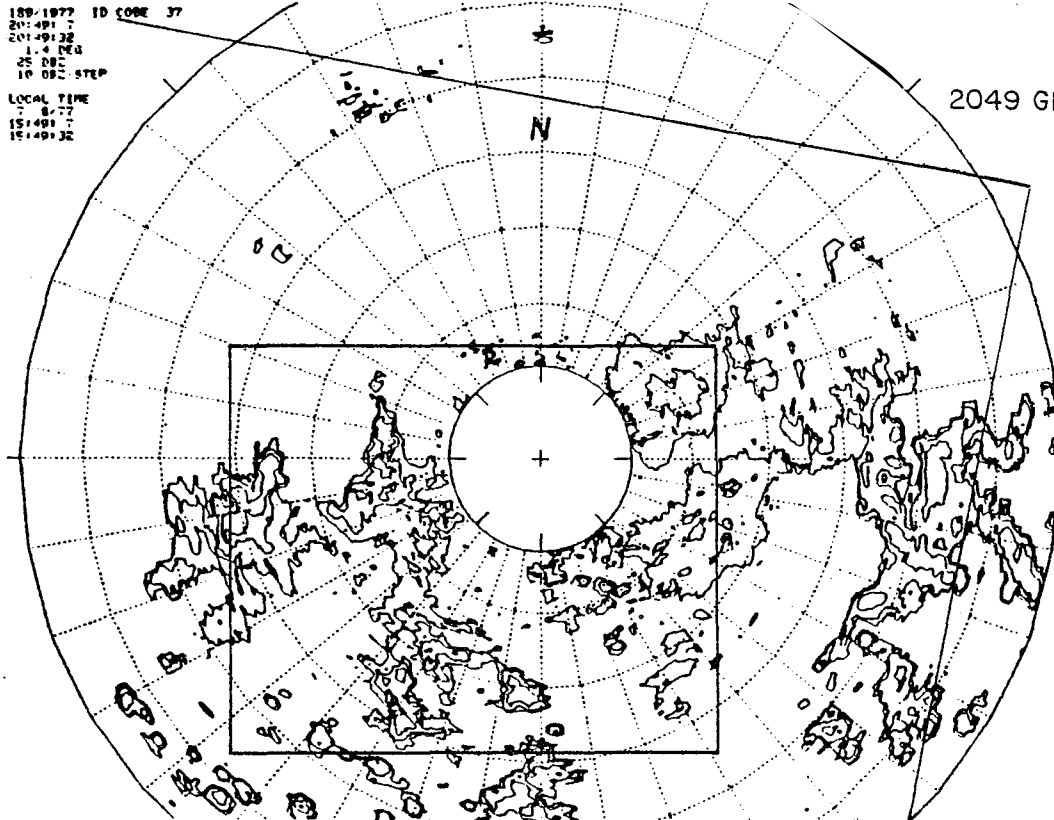
Figure 4-5   Continued
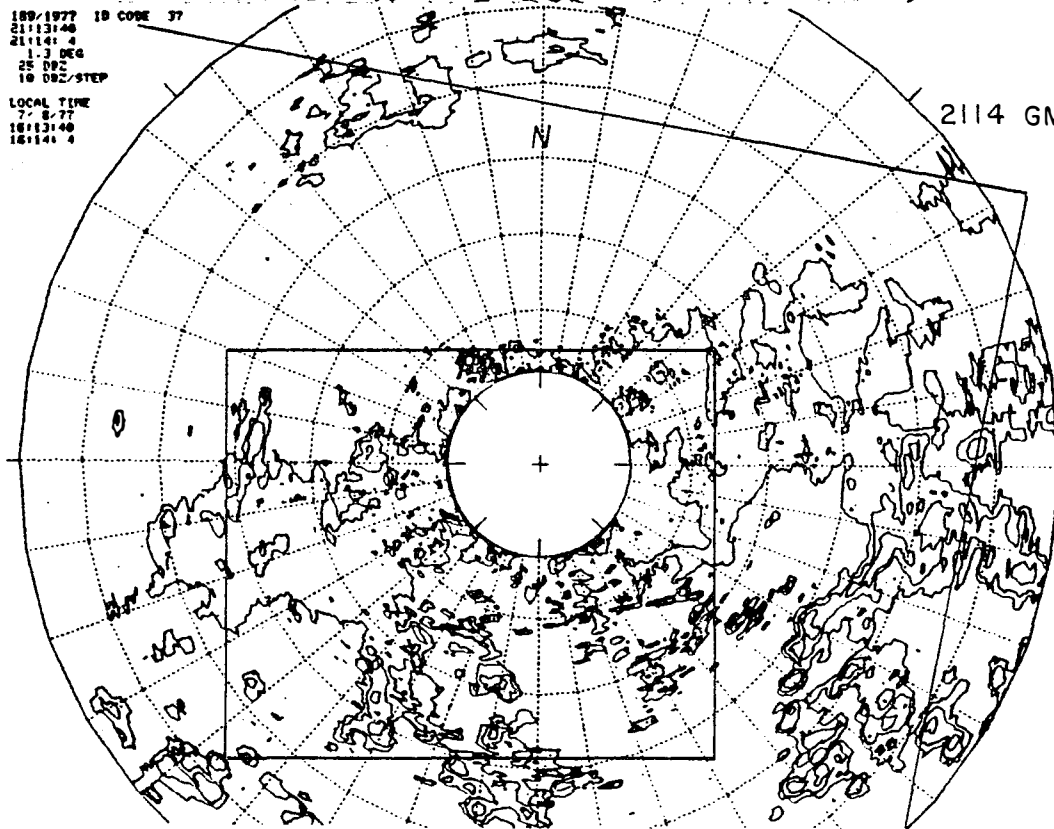
Figure 4-5   Continued

with the position of the storm cells on the PPI plot at
1845 GMT. The plot for 1937 GMT shows that a cluster of
strong reflectivity cells located in the central portion
of the raingage network passed through the Snyder area,
although no data were available within 25 km of the radar
site because of the range delay. The rainfall pattern
during the period 1930-1945 GMT verified that a heavy rain
band passed through this area, producing more than 0.80
inch within 15 minutes at two stations. The radar PPI
plot for 1948 GMT and the corresponding precipitation
pattern had similar shapes and position. The rain band
structure persisted until 2018 GMT, maintaining the same
appearance in the precipitation pattern. The rainfall
intensity decreased rapidly after 2015 GMT, although the
rainfall area remained in the central portion of the
raingage network. The PPI plots show that the echo area
became more widespread later, but that reflectivity values
weakened. The precipitation analysis and digital PPI
plots were in good agreement on this point. The satellite
visible data showed increases in the percent cloud cover
and in the area covered by the brightest clouds early in
the study period, reaching maximum values near 2015 GMT,
as was observed in the precipitation pattern. The area of
high cloud tops seen in the infrared satellite radiance
data also changed following the behavior of the precipi-
tation pattern. A more detailed discussion of this

comparison is included in the next subsection.

4.1.2.4 Visible and Infrared Radiance Data Combined with Rainfall Records

The latitude and longitude coordinates of each raingage station have been located in the satellite radiance data arrays. After plotting the raingage data, isohyetal patterns were constructed in the transformed coordinate system for comparison with the radiance data. Note that the reference coordinate system was selected to be the rectangular array of visible satellite radiance data.

The rain began in the interval 1830-1845 GMT, as was shown in Figure 4-3. The sequence of diagrams in Figure 4-6 shows the relative location of cloud albedo, cloud top temperature and the rain area. Note that only the coldest isotherms are shown in any given frame in Figure 4-6. The diagram at 1845 GMT shows that the most intense rain area was located under the brightest and coldest cloud tops within which the cloud albedo was larger than 0.63 and the corresponding cloud top height was above 13 km. More than 0.5 inch of rain had occurred within the previous 15 minutes. A strong rain band along a line from Snyder to Big Spring formed soon after the rain began, and is the rain band detected in the PPI radar plots of Figure 4-5. The maximum precipitation occurring within the rain band was located under clouds with either high albedo or
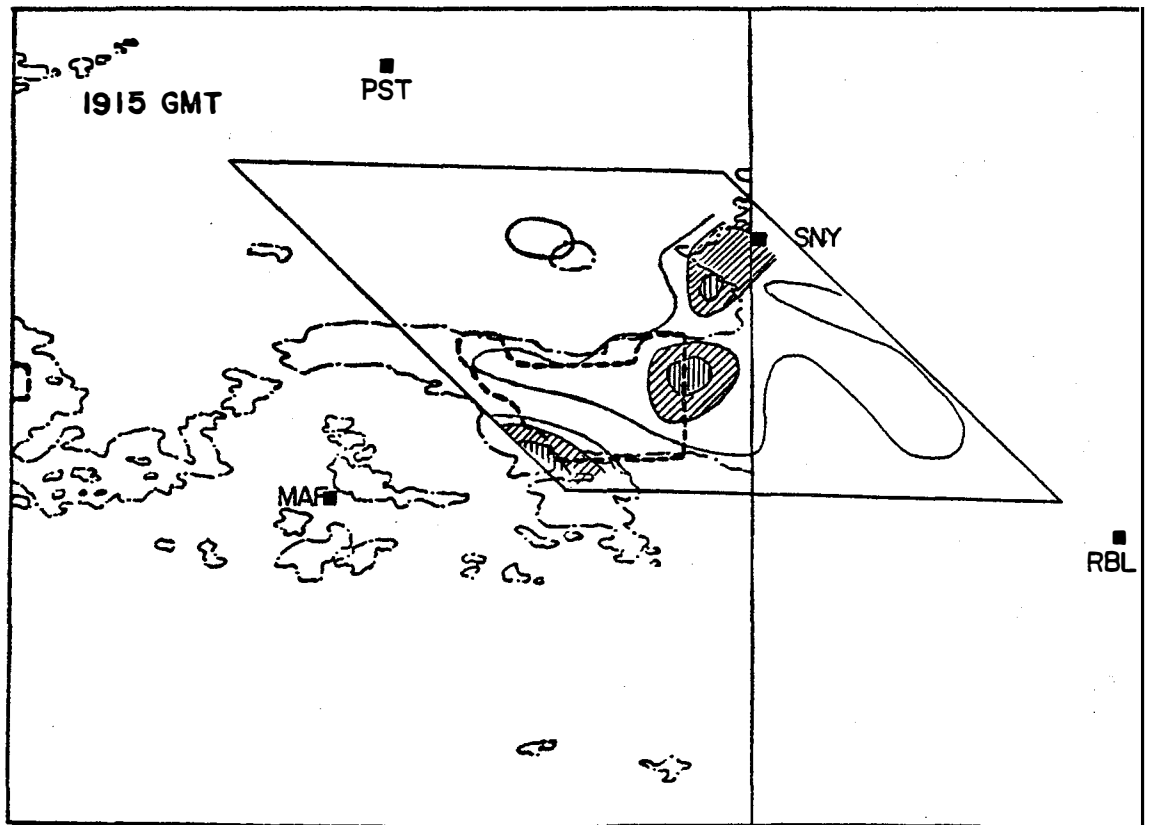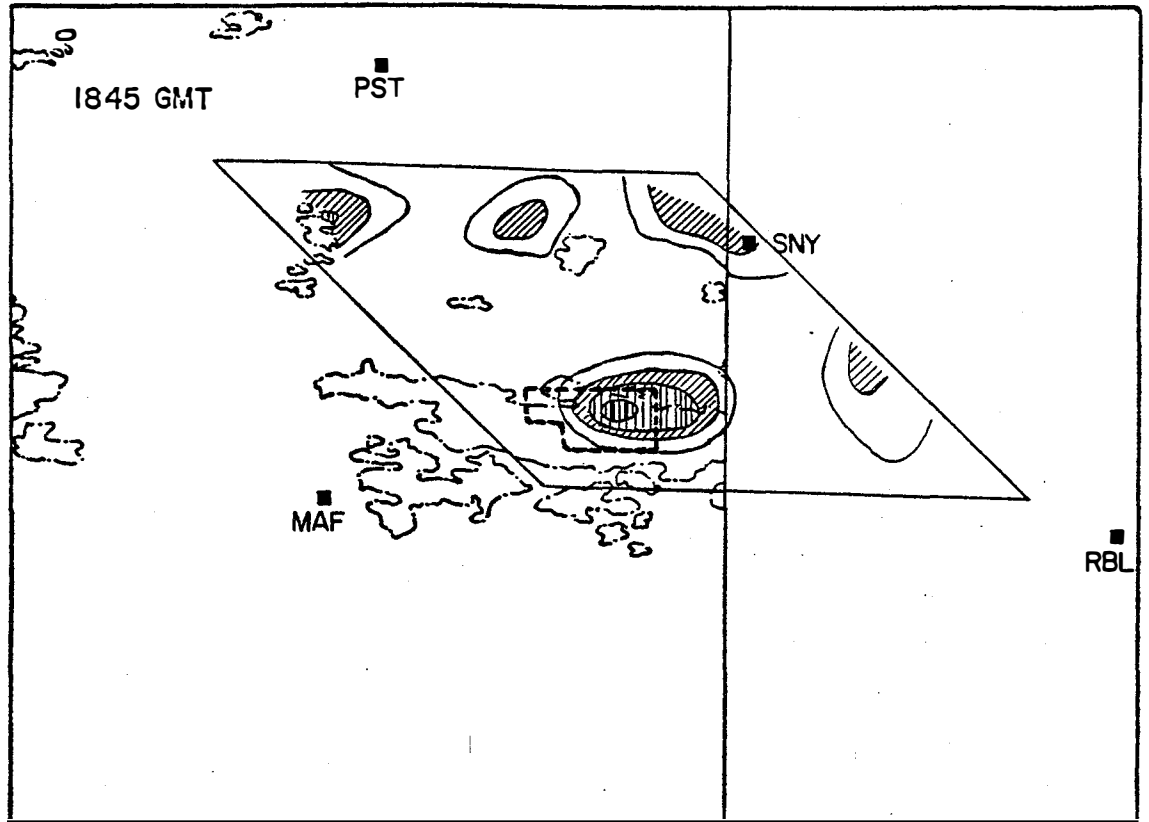
Figure 4-6 Cloud albedo, cloud top temperature and rainfall intensity on 8 July 1977.

1945 GMT
PST
SNY
MAF
RBL

2015 GMT
PST
SNY
MAF
RBL

Figure 4-6   Continued

2115 GMT

PST

SNY

MAF

RBL

Albedo
0.44 — — — —
0.63 — · — · —
Cloud-top temperature (C)
-40 – -49 ················
-50 – -59 — — — — —
-60 – -69 ————

Rainfall (inch/15 min)
0.01 – 0.09
0.10 – 0.24
0.25 – 0.49
0.50 – 0.74
0.75 – 1.00
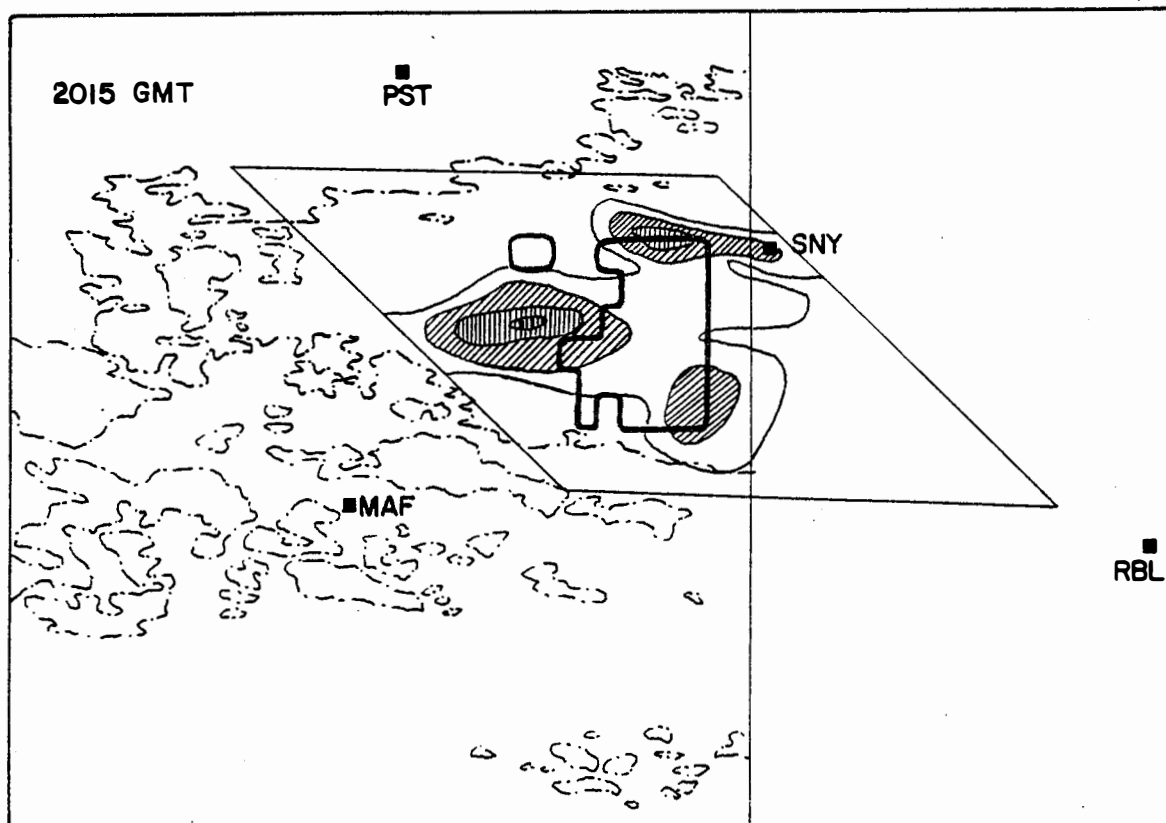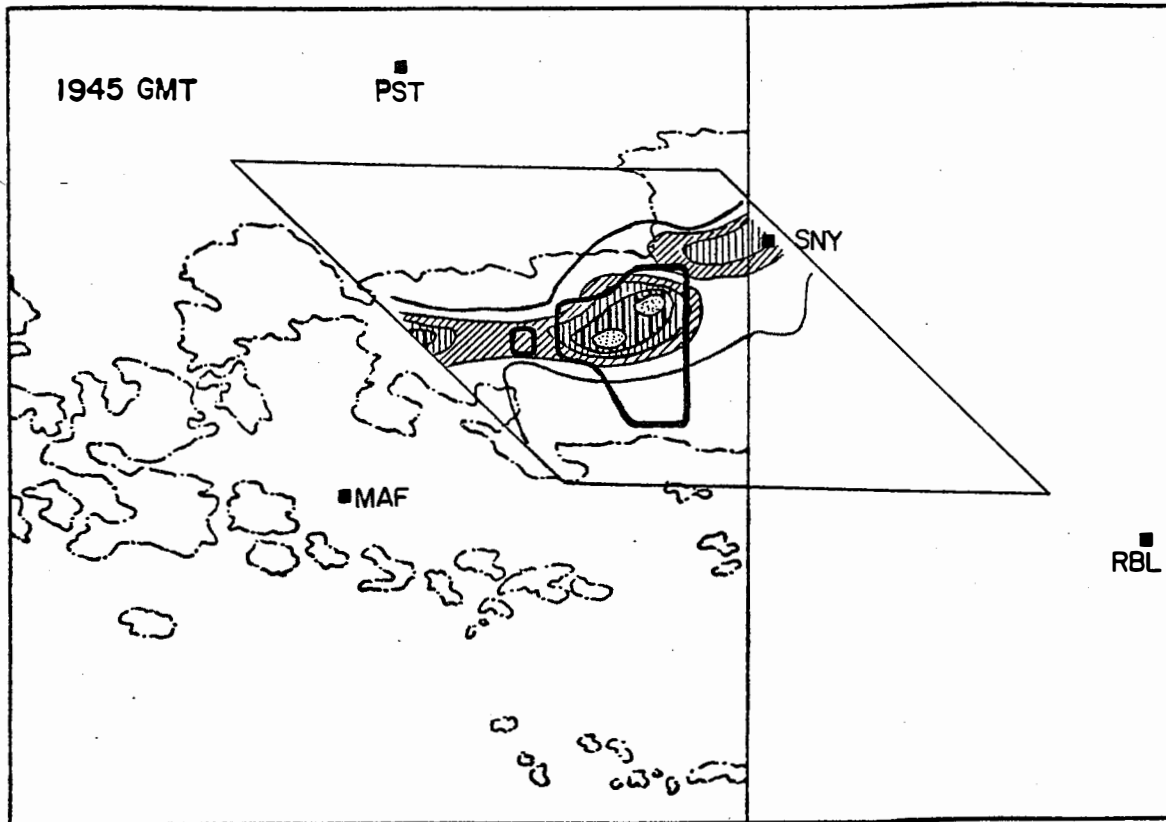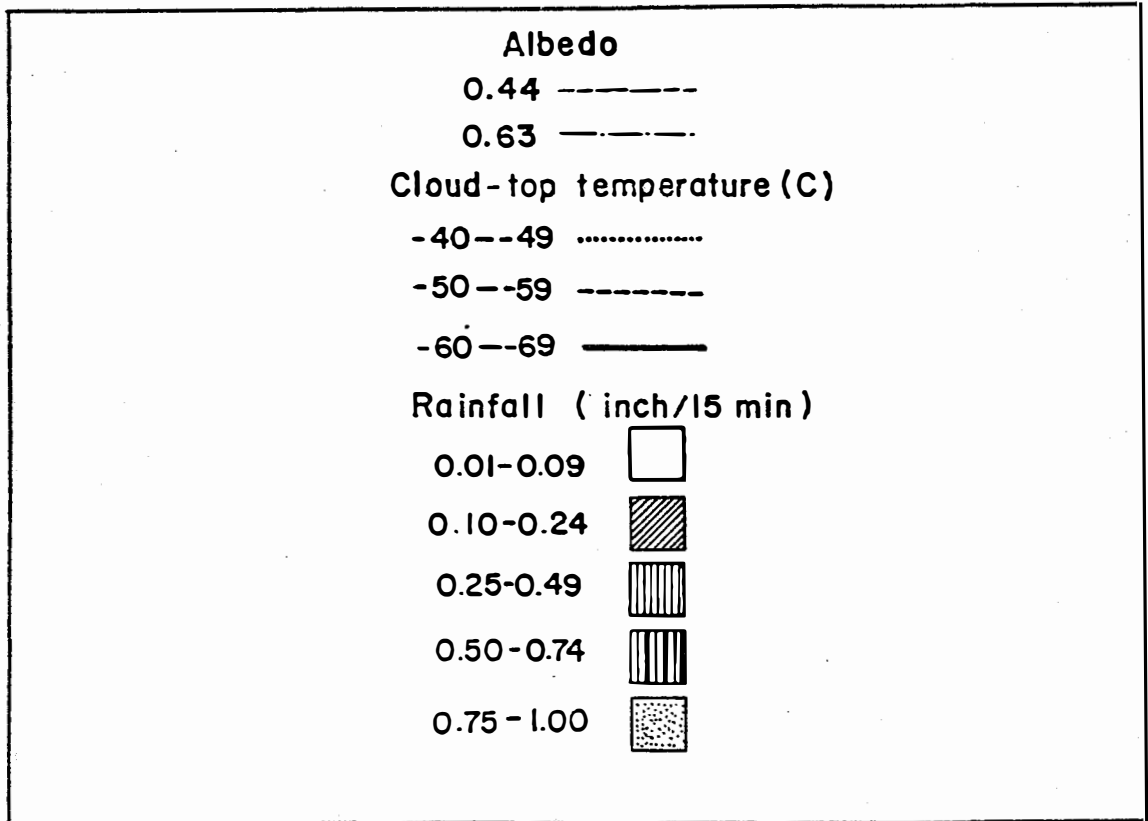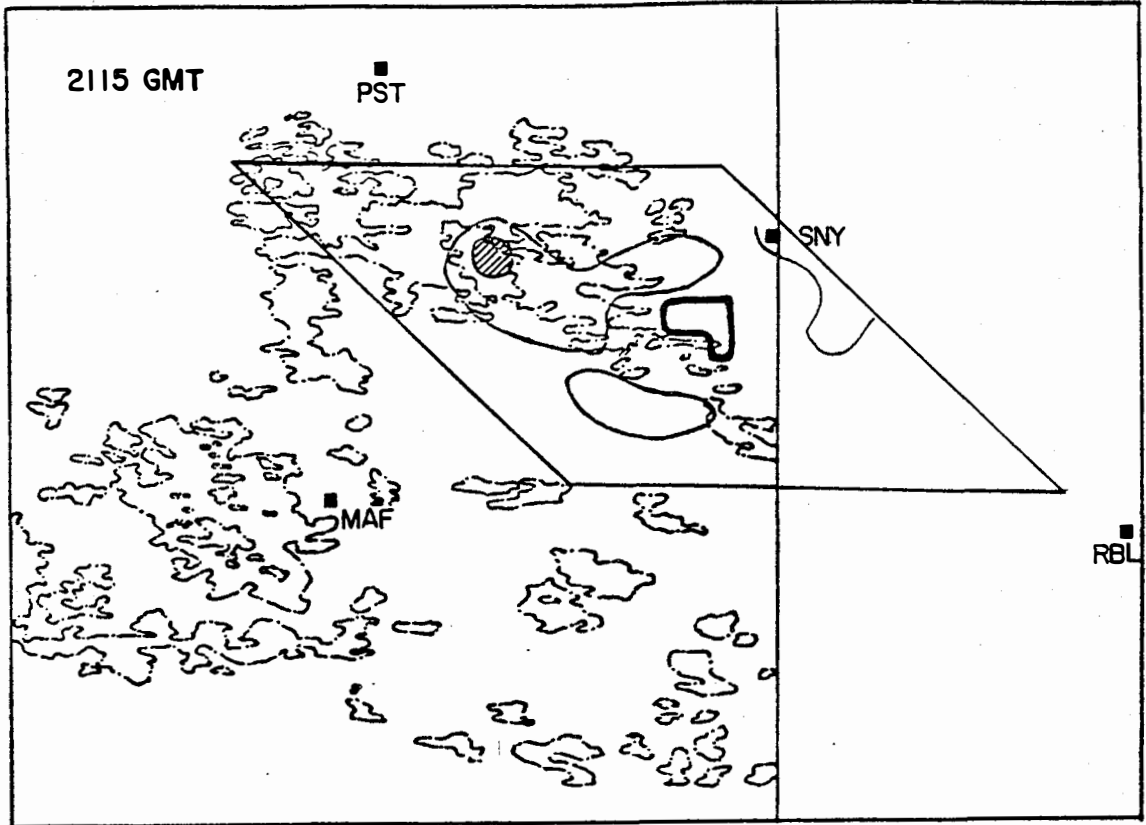
Figure 4-6   Continued

high tops, or both. The rainfall intensity increased
sharply after 1915 GMT when the clouds over the raingage
network developed tops to approximately 14.5 km and the
area of albedo greater than 0.63 increased considerably.
The precipitation peak was reached just before 2000 GMT.
Meanwhile, at 2015 GMT the raingage network was totally
covered by bright and high-topped clouds with albedos
over 0.63 and top heights above 15 km. The PPI digital
radar analysis also indicated that the reflectivity
gradients within the rain band became quite sharp,
attaining values greater than 55 dBz at this time. The
rainfall intensity decreased rapidly after the precipi-
tation peak and little precipitation was recorded after
2200 GMT. In addition, the bright cloud area decreased
and the cloud tops became lower, as seen in the sequence
of satellite visible and infrared data following 2115 GMT.
Finally, the PPI digital plots indicated the rain band
structure broke up and reflectivities weakened after
2114 GMT.

4.1.3 Small-scale Features

  4.1.3.1 Discussion of M-33 Radar
           RHI cross sections

    RHI plots of the M-33 data at 1942 and 2018 GMT are
analyzed in this discussion, and compared with both
satellite-derived cloud top heights and rainfall data.

These times were selected because several particularly interesting clouds were present in the study area (Figure 4-7). Three different cross sections through the storm cells of interest at 1942 GMT are considered in this discussion, while four at 2018 GMT are discussed.

The RHI plots for 1942 GMT were taken along the azimuth angles 200°, 235°, and 242° with respect to Snyder. Figure 4-8 shows the isohyet pattern for the period 1945-2000 GMT, upon which lines are drawn marking the three cross sections to be presented in the RHI radar plots. The cross section along the line AA' in Figure 4-8 shows the vertical structure of a typical isolated storm (Figure 4-9). A strong 50 dBz reflectivity center was located 53 km from the radar site. If the commonly used Z-R relationship, $Z = 200 R^{1.6}$ (Rogers, 1976) is employed to infer an approximate rainfall intensity, one obtains about 0.48 inch within 15 minutes. The actual rainfall measured at the raingage along this cross section was 0.31 inch within the same time, good agreement considering that a different Z-R relation might be appropriate or that evaporation below the cloud base may have occurred. The cloud top heights estimated from the satellite infrared data and soundings at Big Spring varied from 13 to 15 km. In addition to the actual estimated heights, the cloud top estimates which would result from cloud top temperatures errors of 3 C have been shown in order to provide a measure of the uncertainty (seen to be approximately
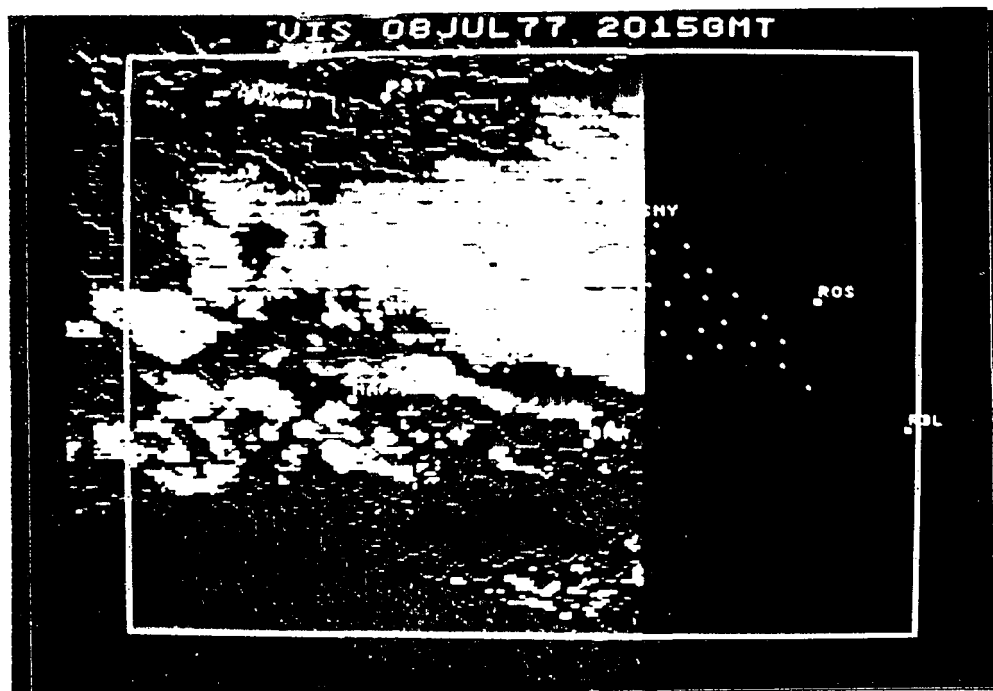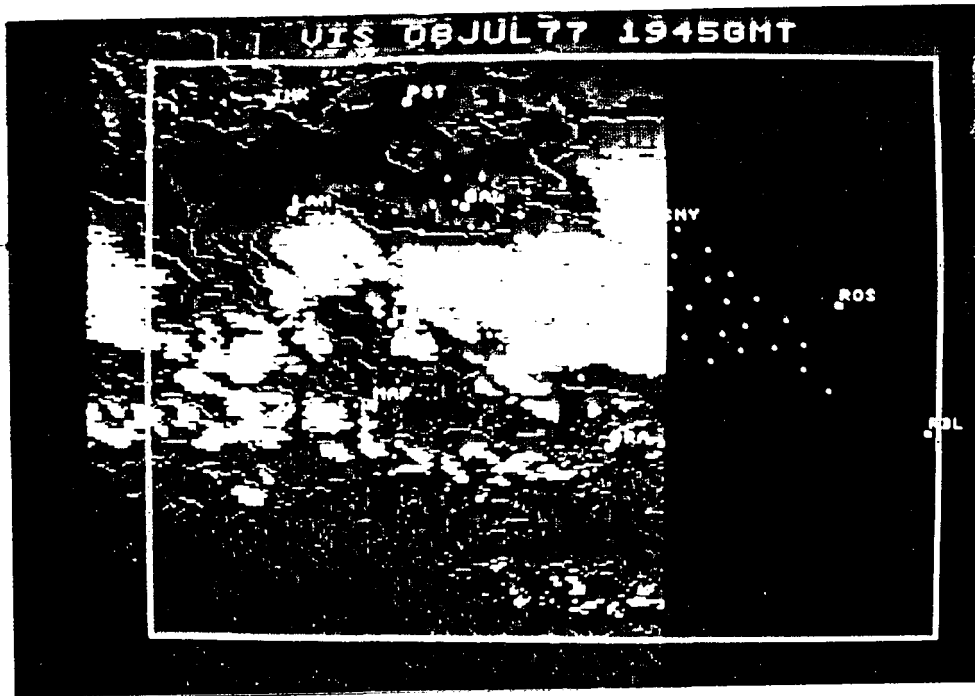
Figure 4-7   Enhanced visible pictures at 1945 and 2015
             GMT on 8 July 1977. The colors correspond
             to albedo as follows: red, 0.24 - 0.43;
             blue, 0.44 - 0.62; yellow, 0.63 - 0.79;
             black, 0.80 - 1.00
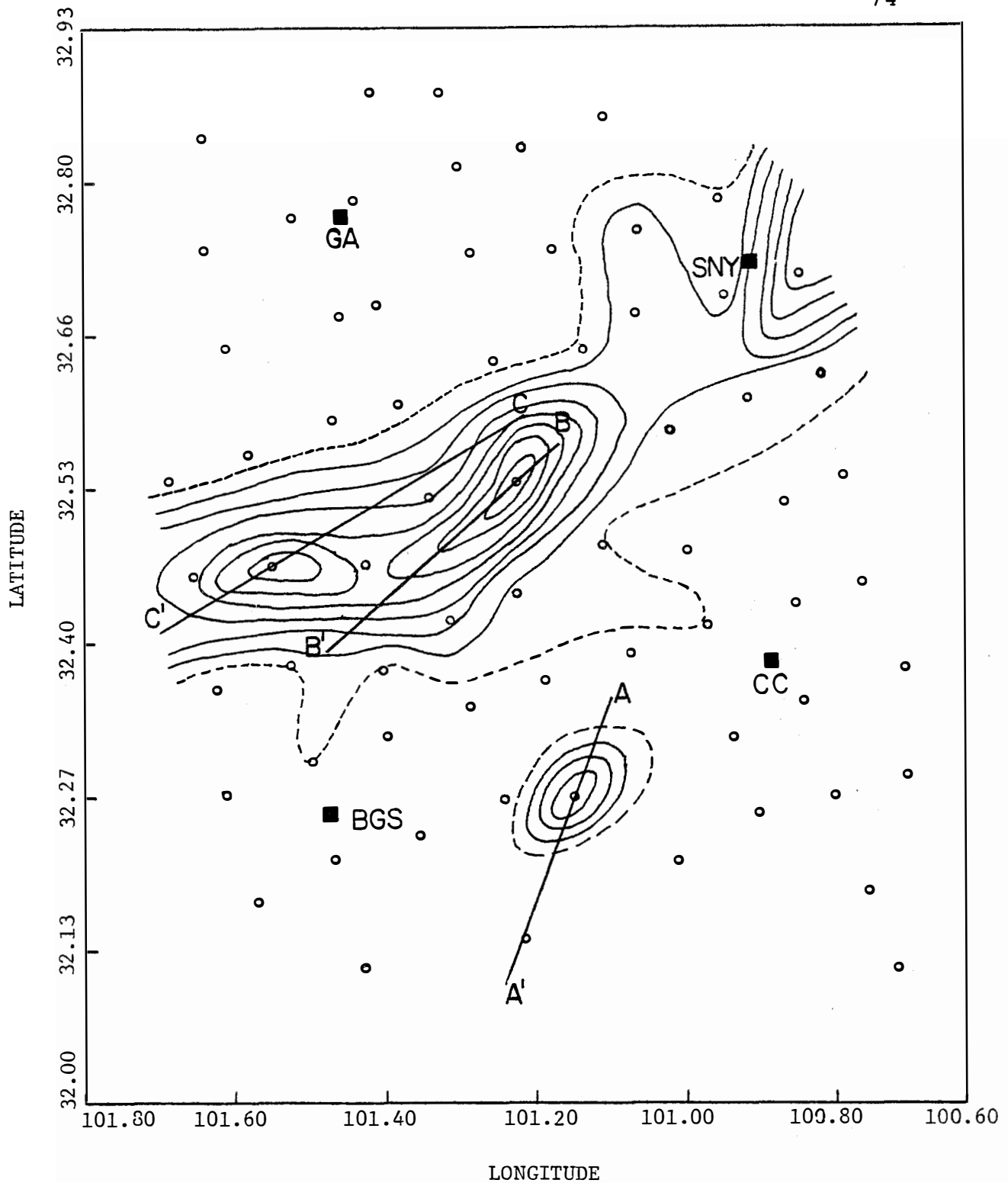
Figure 4-8   Isohyet pattern for the period 1945-2000 GMT
             8 July 1977.   The dashed line is the isohyet
             for 0.01 inch, and the solid lines are
             contoured with a threshold of 0.1 inch
             and given in 0.1 inch increments.
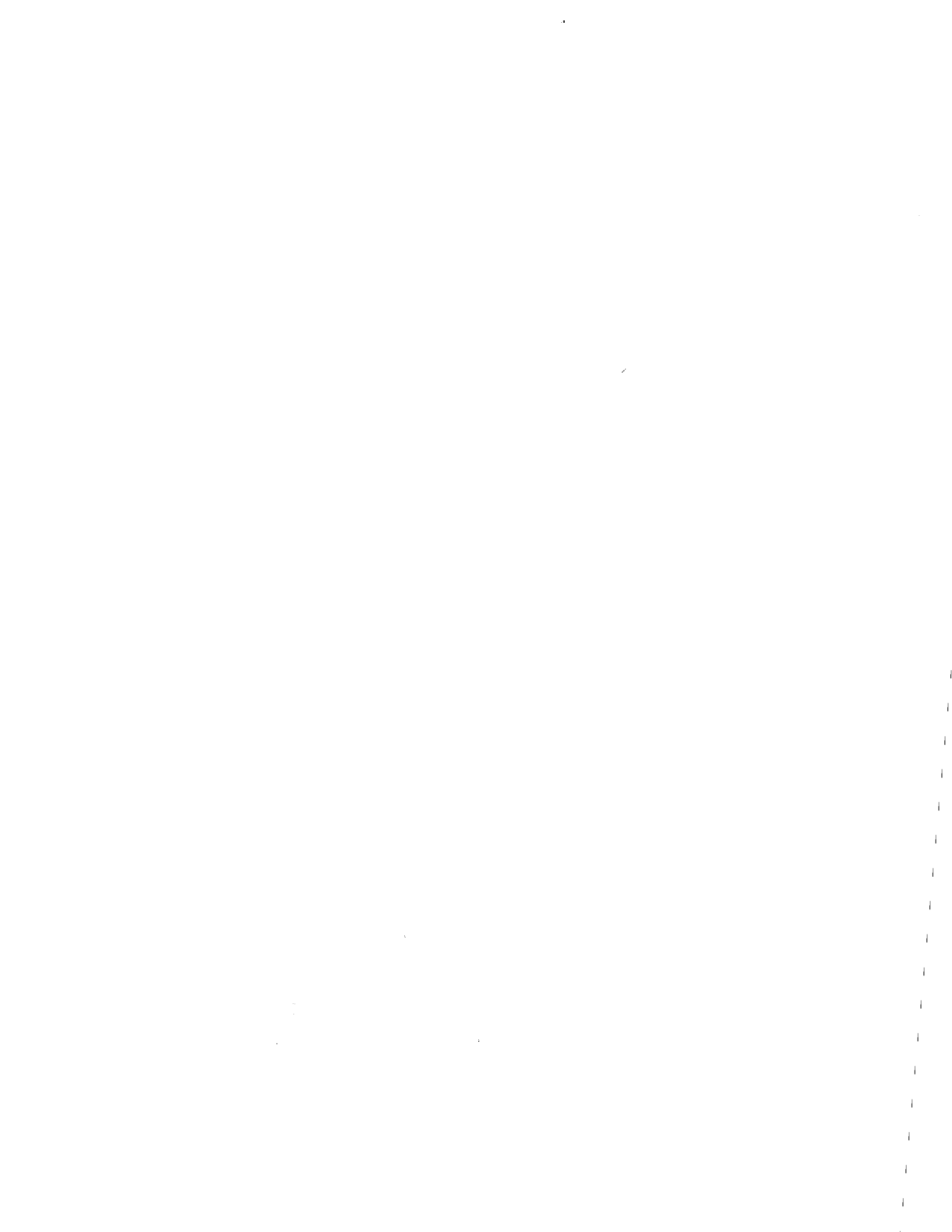
Figure 4-9 RHI display derived from M-33 radar for the azimuth angle 200° at 1942 GMT 8 July 1977. The threshold is 30 dBz and is contoured in 10 dBz increments. The upper solid line is the cloud top height derived from satellite infrared data and the dashed lines correspond to a temperature uncertainty of ±3 C. Also shown are rainfall analysis results with actual raingage measurements marked by ▲ .

1 km) in cloud top height associated with what is often considered to be a reasonable estimate of the error in cloud top temperature measurements. The minimum detectable signal at 1942 GMT on 8 July was 30 dBz. Therefore, the top of the precipitation-particle produced echo detected by radar at 1942 GMT was considerably below the cloud top detected with the satellite infrared data.

The cross section along the line BB' in Figure 4-8 contained more intense reflectivity values, as evidenced by a raingage measurement at 32 km range of 0.80 inch within 15 minutes (Figure 4-10). Cross section BB' has been located directly within the rain band structure identified in the PPI plots of Figure 4-5. As in cross section AA', the satellite-derived cloud tops remained uniform in height along the length of the cross section. The assumed Z-R relation gave a rainfall under the intense reflectivity center of 0.9 inch over a 15-minute interval.

The cross section along the line CC' in Figure 4-8 is of special interest in this study (Figure 4-11). The satellite-derived cloud top heights varied greatly close to the radar site and even overlapped the heights indicated by the M-33 radar. Beyond 35 km in range, the cloud top heights increased to approximately 12 km and then remained quite level. The apparent error in cloud top height can be explained by the fact that each infrared pixel covered a rather large area, about 5.8 x 11.7 km.
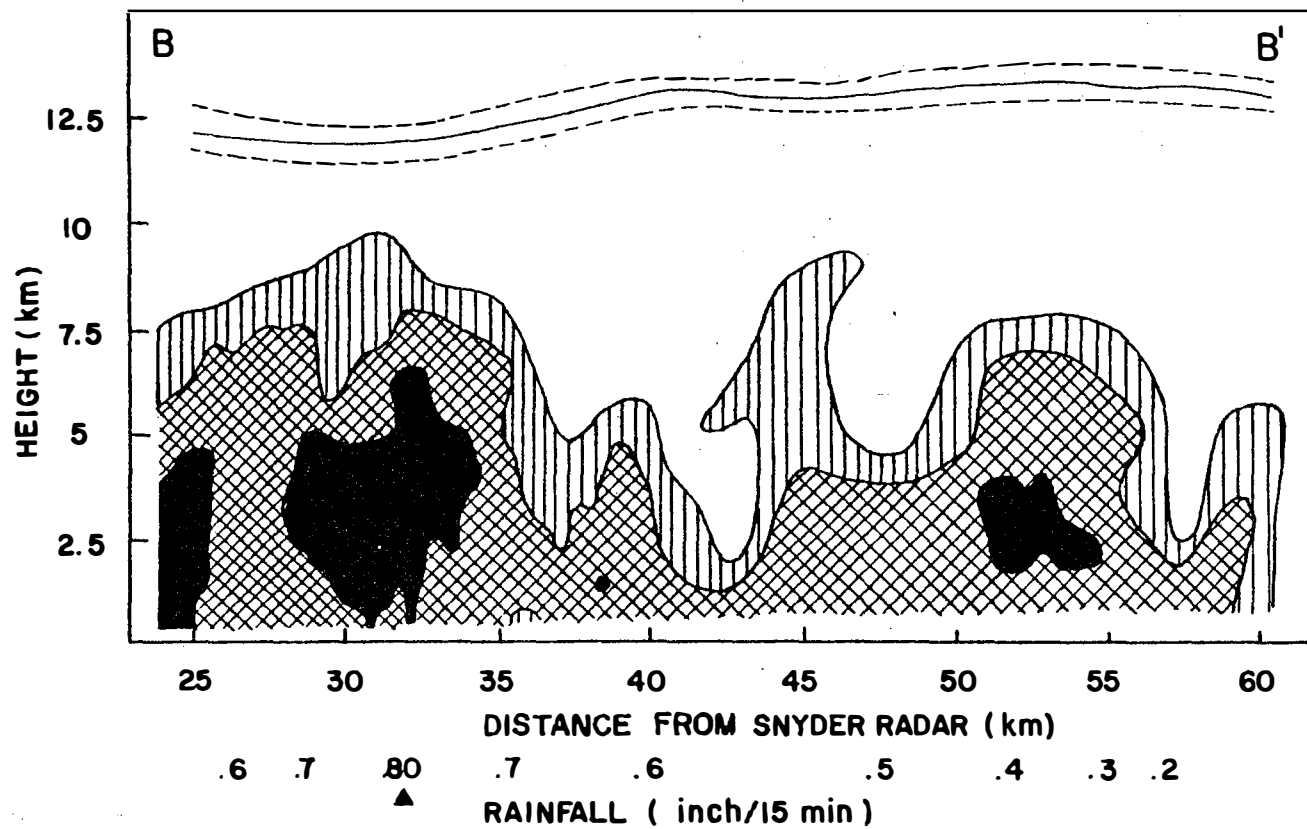
Figure 4-10   Same as Figure 4-9 for the azimuth angle 235°.
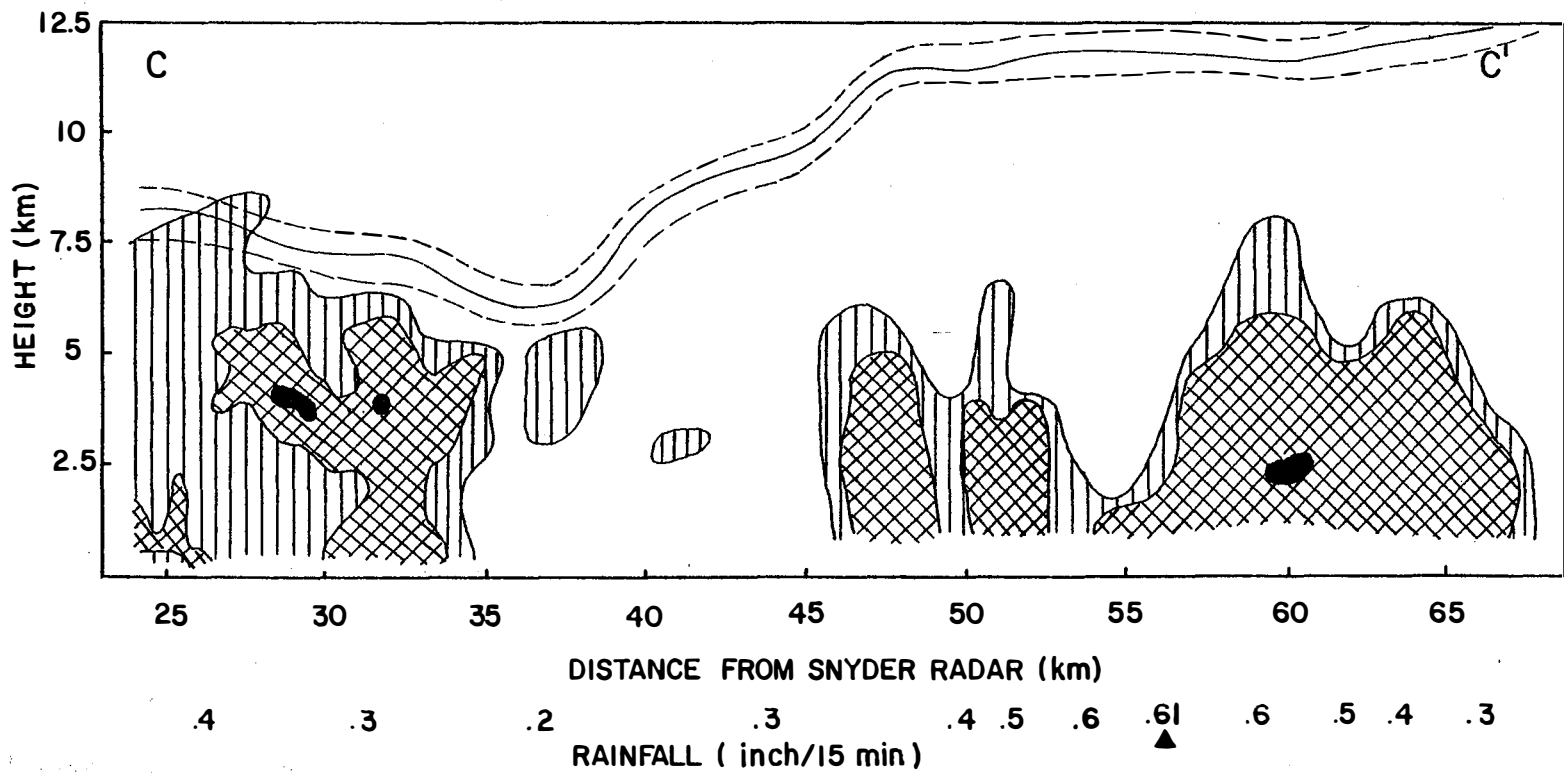
Figure 4-11   Same as Figure 4-9 for the azimuth angle 242°.

As a result, the satellite infrared data simply averaged away the presence of smaller cells detectable by radar. Improvement in the spatial resolution of satellite infrared sensors is clearly needed, as this case demonstrates. Nonetheless, the agreement among the several data sets is quite acceptable.

Four RHI cross sections at 2018 GMT along azimuth angles 211°, 223°, 253°, and 259° are discussed because each of them passed through an intense storm (Figure 4-12). The minimum detectable signal at this time was about 17 dBz, resulting in considerably higher radar echo tops, reaching 13 km, than were seen at 1945 GMT. The satellite-derived cloud top heights were closer to the radar reflectivity heights at this time because of the smaller detectable signal.

The RHI plot, satellite cloud top heights and the rainfall measurements along the line DD' are shown in Figure 4-13. There were three storm cells detected by the M-33 radar along this cross section, the closer two being within the raingage network. The satellite cloud top heights were quite uniform over the storm cells and above the radar reflectivity pattern. However, beyond the range of the main storm cells the satellite cloud top heights decreased noticeably. The assumed Z-R relation yielded a 15-minute rainfall of 0.15 inch under the reflectivity maximum of 42 dBz, located 55 km from the
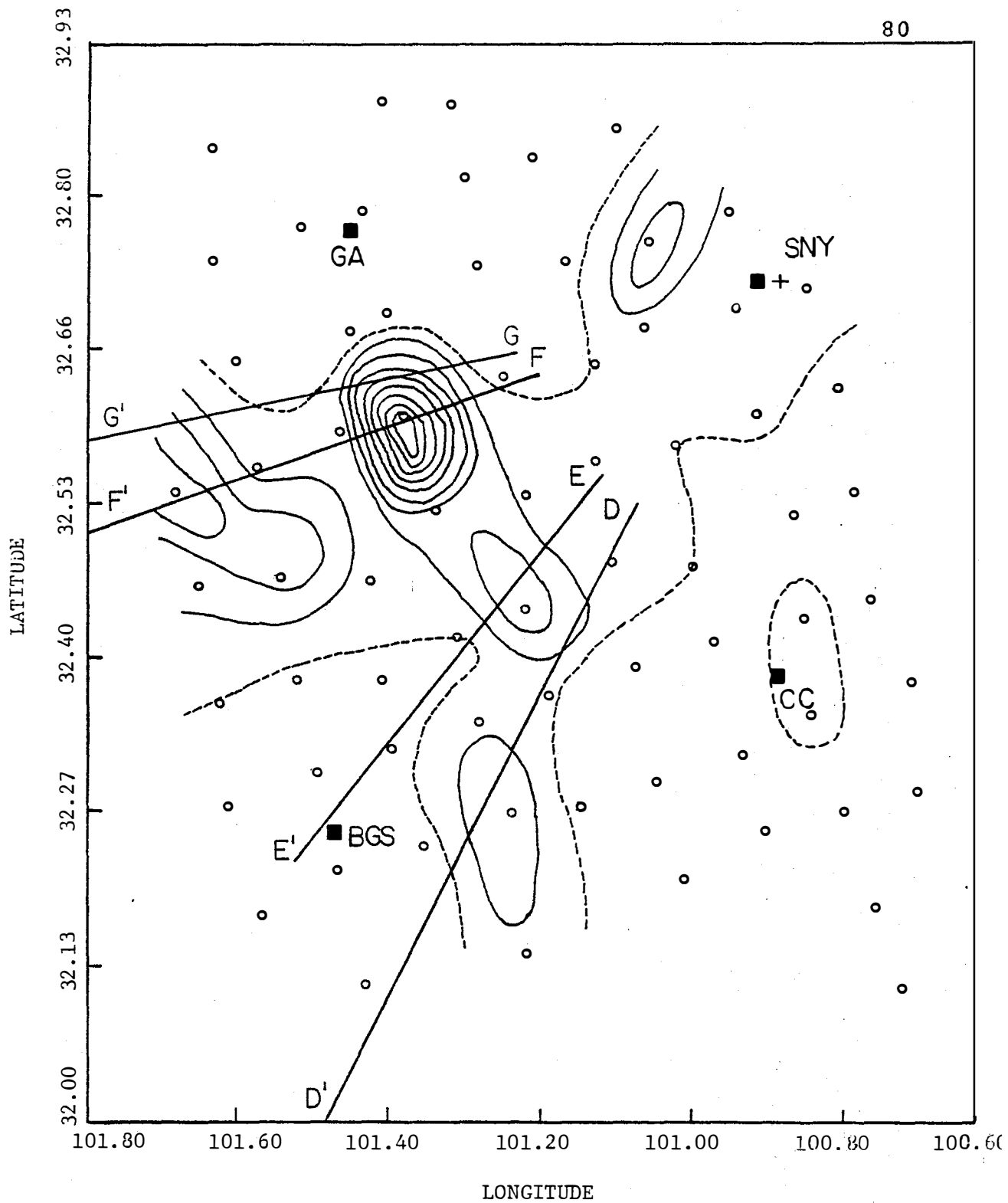
Figure 4-12   Isohyet pattern for the period 2015-2030 GMT
8 July 1977.   Codes are the same as
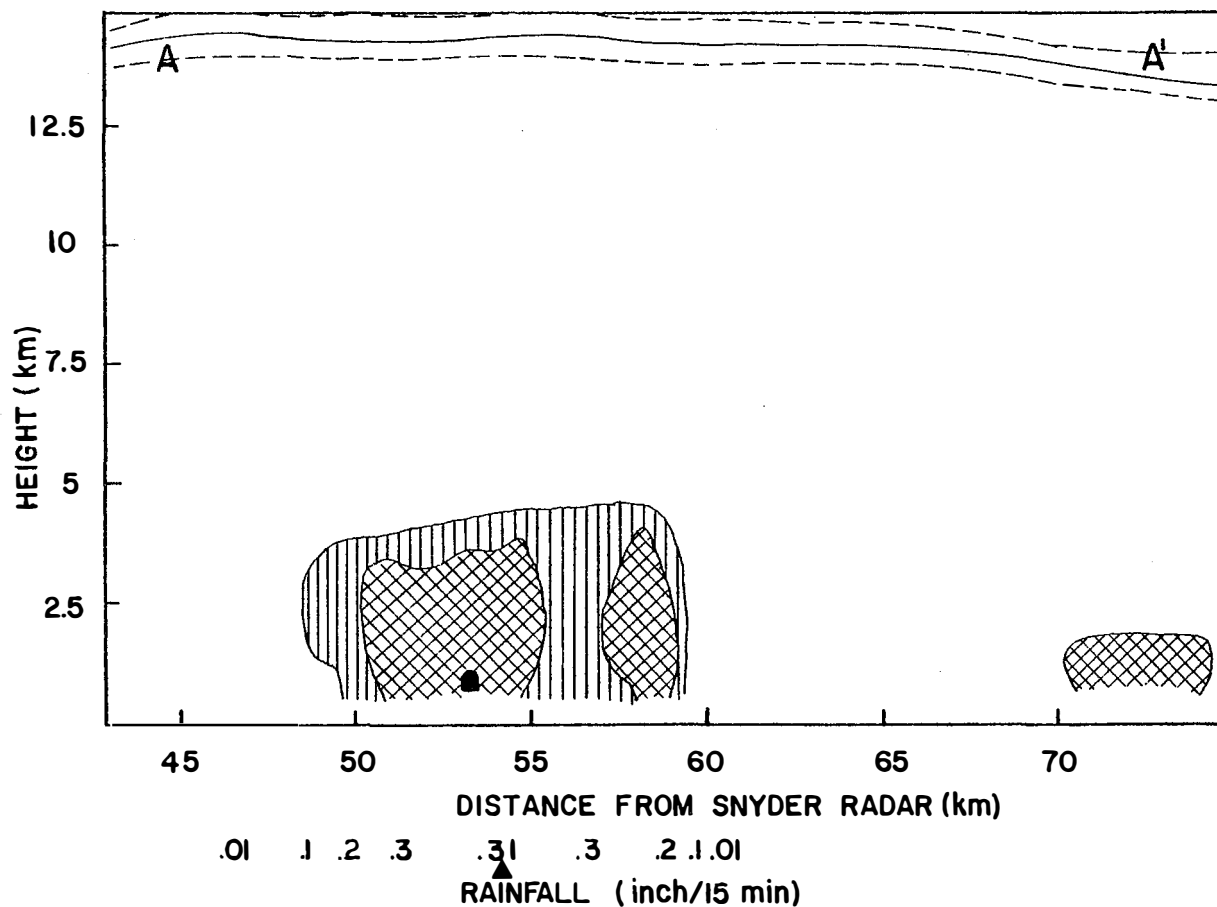Figure 4-8.
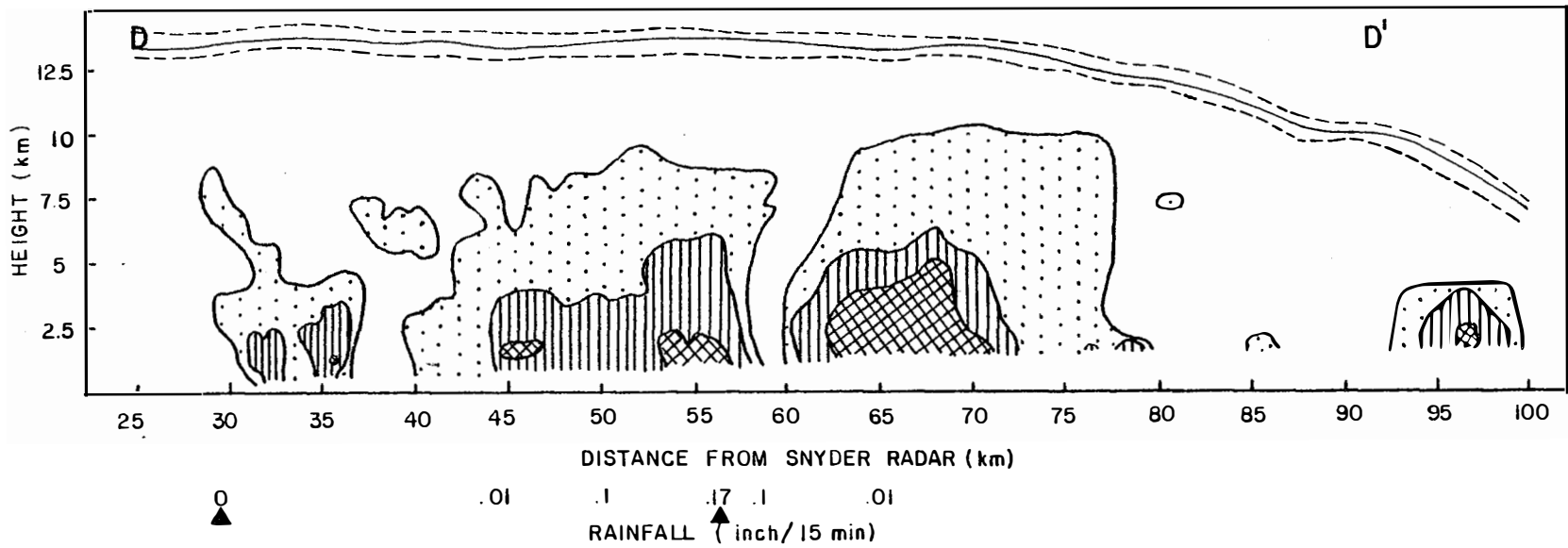
Figure 4-13   RHI display derived from M-33 radar data for the azimuth angle 211°
at 2018 GMT 8 July 1977.   The data threshold is 20 dBz and is
contoured in 10 dBz increments.   The upper lines are the same
as in Figure 4-9.

Snyder radar, compared to 0.17 inch recorded by the raingage network.

Figure 4-14 shows the cross section along the line EE' in Figure 4-12. The satellite cloud top heights were nearly horizontal and followed closely the shape of the echo tops. The lowest cloud tops of 13 km were located at a range of 68 km over a weak reflectivity region, and were only 1 km lower than the maximum cloud top heights found near a range of 30 km. The strongest reflectivity area was located between 30 km and 43 km from the radar site and corresponded to the small storm cell apparent in Figure 4-12. The computed rainfall in this case was 0.20 inch under the reflectivity storm cell, corresponding to a reflectivity of 44 dBz.

The cross section at an azimuth angle of 253° is shown by line FF' in Figure 4-12. This line passed through the most intense rainfall area at this time which was located inside the rain band discussed earlier (Figure 4-15). The total precipitation measured in the center of this cell over 15 minutes was 0.89 inch, while the reflectivity there was close to 60 dBz. The satellite-derived cloud heights were quite uniform over the intense reflectivity area, but decreased rapidly beyond the storm. The satellite cloud heights and radar echo tops again overlapped within the intense radar reflectivity cells. However, the overlap was within the uncertainty of the
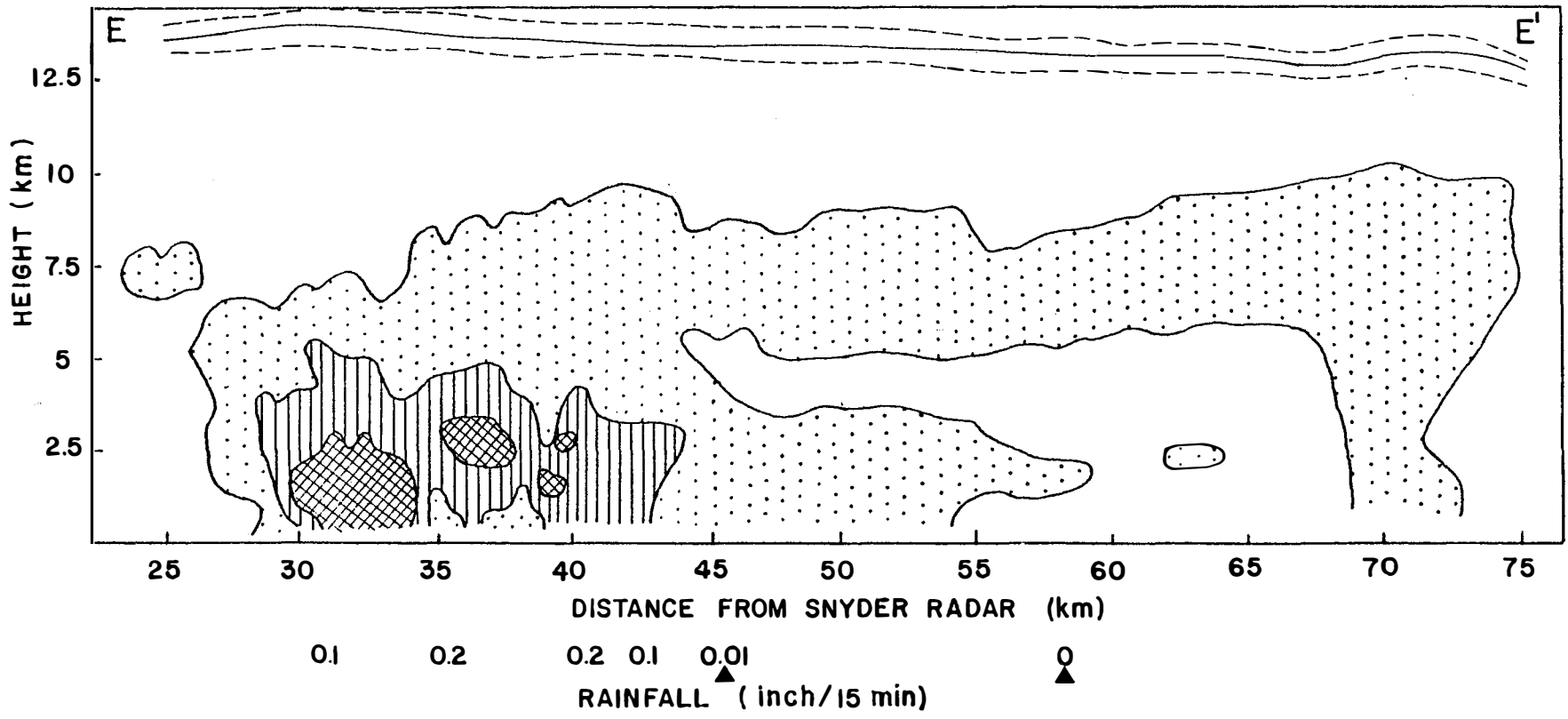
Figure 4-14   Same as Figure 4-13 for azimuth angle 223°.
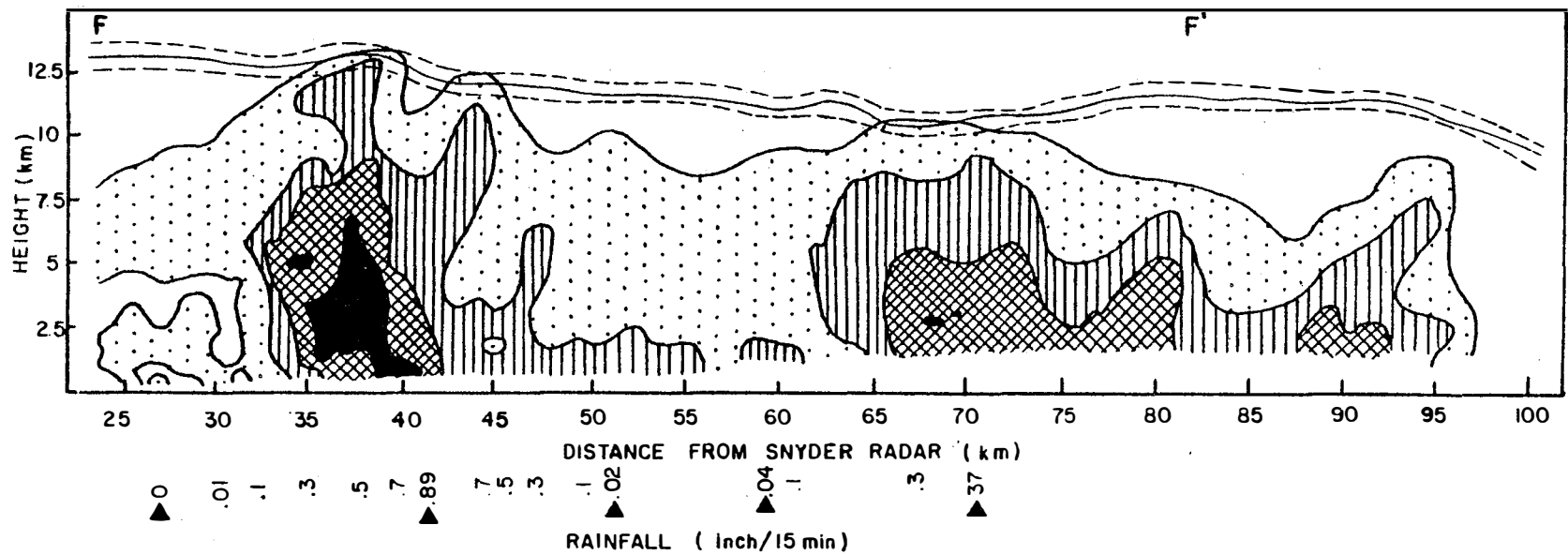
Figure 4-15   Same as Figure 4-13 for azimuth angle 253°.

satellite-derived cloud top heights. The gradient of precipitation intensity under the strong storm cell was sharp with the heaviest rain occurring immediately under the intense reflectivity core. The radar reflectivity under that strong storm cell was about 55 dBz, inferring 0.98 inch of rain within 15 minutes from the assumed Z-R relation.

One case of special interest is the cross section along the line GG', for an azimuth angle of 259°. This case is discussed here because the most intense reflectivity at this time occurred along this line (Figure 4-16). The structure was similiar to the previous case along FF'. A strong storm cell with large reflectivity gradients was located 35 km from the radar site. This cross section was along the edge of the rain band discussed before, and shown in Figure 4-5. The cloud top heights from the infrared radiances varied from 11 to 12.5 km over two intense storm cells, but decreased rapidly beyond the third storm cell which was located about 80 km from the radar. The agreement between the satellite cloud top heights and radar reflectivity was good along this cross section. A strong reflectivity maximum of more than 60 dBz was located 35 km from radar site. It is probable that heavy rain did occur under this intense echo which occurred within the raingage network, but there was no raingage located exactly along this
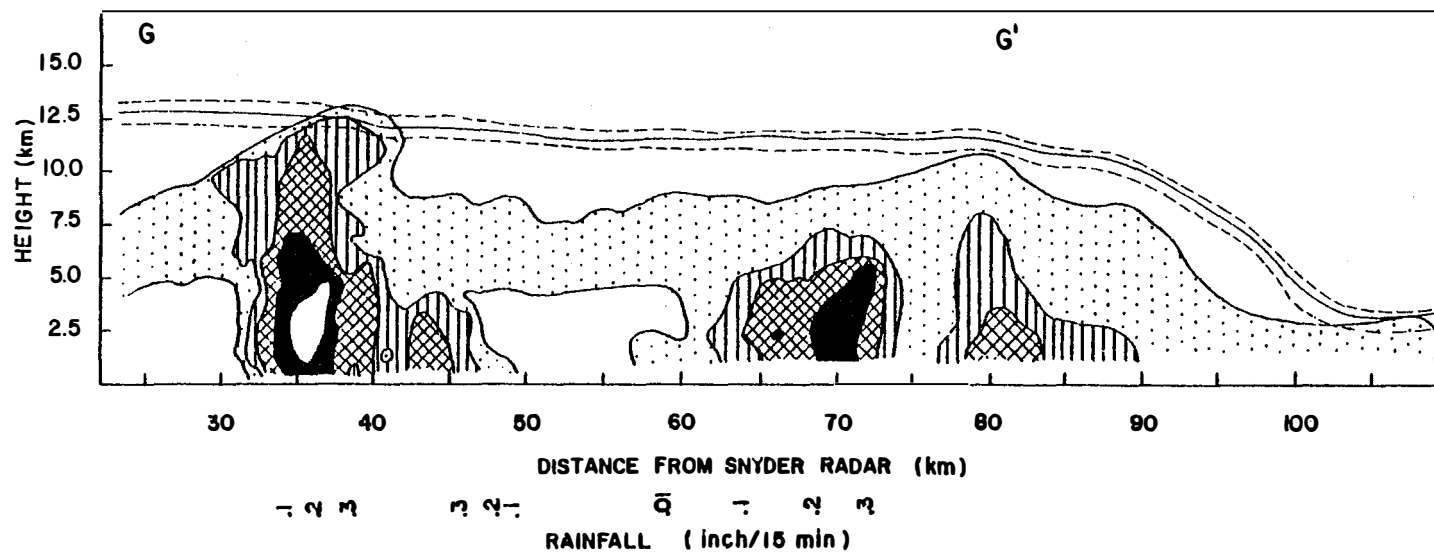
Figure 4-16   Same as Figure 4-13 for azimuth angle 259°.

direction. This example illustrates the restrictions associated with interpreting rainfall measurements even from a raingage network with rather dense spacing, and points to the desirability of higher resolution data sources such as radar or satellite measurements.

4.1.3.2   Review of Soundings

Atmospheric soundings were made as part of the mesoscale program of Texas HIPLEX. The measurements were made and the data processed by personnel at Texas A & M University. Temperature, moisture and wind were extracted from the soundings at 25-mb intervals (Scoggins, 1977). Although the data were available at Midland, Post, Robert Lee and Big Spring, only the soundings at Big Spring are discussed in this study, because it has been determined that, although station-station variations did exist, the temporal changes at a given station were more revealing.

Figure 4-17 shows the soundings at Big Spring on 8 July. The atmosphere was rather dry at 1500 GMT, but the moisture content then increased rapidly until 1800 GMT. The negative area had disappeared by 1800 GMT as the surface warmed up, and convective processes had become likely. Later in the afternoon, the surface was saturated at both 2100 GMT and 0000 GMT 9 July. By this time major precipitation events had occurred. The diamond-shaped appearance of the soundings in the lower layers at both of
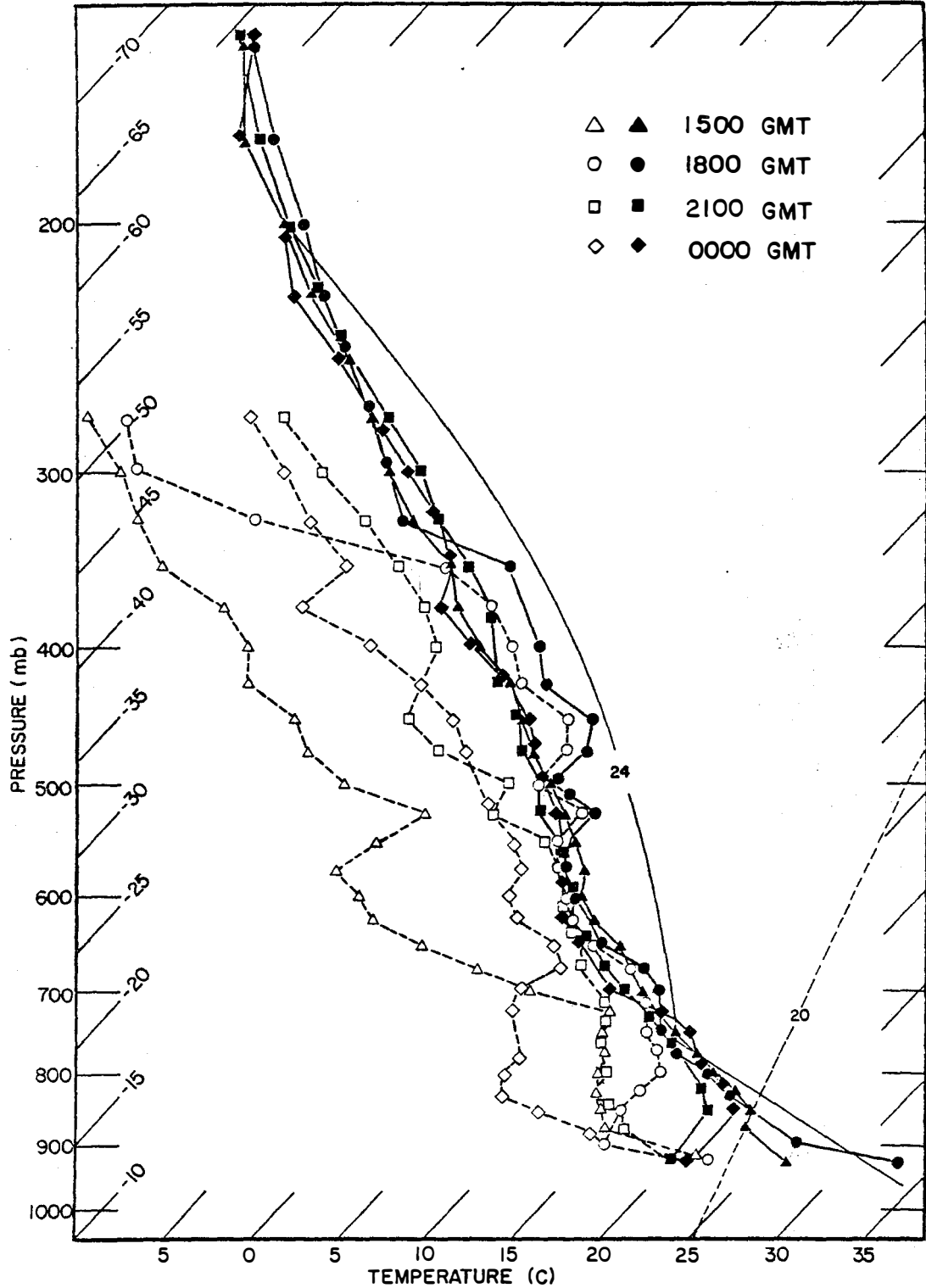
Figure 4-17   Atmospheric soundings taken at Big Spring on
8 July 1977. Open symbols connected by
dashed lines are dew-point and full symbols
connected by solid lines are temperature
on a skew T-log P chart.

these times is clearly evident in Figure 4-17. Usually, unsaturated air and subsidence exist in such a region beneath an anvil cloud (Zipser, 1977). The previous discussions have already pointed out that the thunderstorms began to dissipate after 2100 GMT on this day, an observation which is consistent with the above-stated condition.

4.1.3.3 K-index and Precipitable Water Values

A study of the relationship between various stability parameters (such as the Showalter Index, Total Totals, K-index, SWEAT, etc.) and the occurrence of deep convection in the Texas HIPLEX area (Alexander, 1979) showed the K-index to be a good indicator of weather conditions of interest to this study. The K-index is a measure of thunderstorm potential based on the vertical lapse rate, the moisture content of the lower atmosphere and the vertical depth of the surface moist layer. The temperature difference between 850 and 500 mb is used to parameterize the temperature lapse rate. The 850-mb dew point temperature provides information on the moisture content of the lower atmosphere. The vertical extent of the moist layer is indicated by the 700-mb dew point depression. When these parameters are combined, the K-index is expressed as follows:

$$K = T_{850} - T_{500} + T_{d850} - T_{700} + T_{d700}$$

where temperatures are expressed in Celsius degrees.
The suggested probabilities of thunderstorm occurrence
are as follows:

K Value	Thunderstorm Probability
< 15	0%
15 - 20	20%
21 - 25	20 - 40%
26 - 30	40 - 60%
31 - 35	60 - 80%
36 - 40	80 - 90%
> 40	near 100%

Precipitable water provides an estimate of the
maximum amount of rainfall that might occur over the
target area under perfectly efficient conditions. The
amount of precipitable water in the atmosphere can be
expressed as follows:

$$W = \frac{1}{g} \int_p^{p_0} q \, dp$$

where W stands for precipitable water, g is gravitational
acceleration, q is the specific humidity and p is
pressure. The integral can be evaluated by dividing the
atmosphere into layers of approximately uniform specific
humidities, solving for these individually and then
summing.

The K-indices and the corresponding suggested

thunderstorm probabilities as well as precipitable water
calculated from the sounding data on 8 July are listed in
Table 4-2. The large K-indices, which averaged 37 on this
day, indicated that the occurrence of thunderstorms was
highly probable. In fact, strong thunderstorms accompa-
nied by heavy rain were caused by the frontal activity
which occurred on this day, as discussed previously. It
is interesting to note that the variation of the K-index
with time at Big Spring correlated well with the thunder-
storm development. It increased toward 1800 GMT when the
rain began and decreased after 2100 GMT when the storm
dissipated. Note also that Big Spring is the only
sounding station within the raingage network, and was
located close to the rain band observed in both the
satellite imagery and radar PPI displays. The several
items noted here appear to confirm that the K-index is a
good indicator of weather conditions for the Texas HIPLEX
area.

Most of the values of precipitable water were greater
than 3 cm and even greater than 4 cm in some cases. The
four-station average for 8 July was 3.64 cm, indicating
that more than ample moisture was available on this day.
The variation of precipitable water with time at
Big Spring followed a pattern similar to that of the
K-index on this day. The four-station mean values of
precipitable water also varied closely in time with the

Table 4-2

K-indices, suggested thunderstorm probabilities
and precipitable water on 8 July 1977.

Time (GMT)	Midland		Post		Robert Lee		Big Spring	
	K-index	Prob.(%)	K-index	Prob.(%)	K-index	Prob.(%)	K-index	Prob.(%)
1500	37	80-90	40	80-90	37	80-90	35	60-80
1800	40	80-90	35	60-80	35	60-80	42	~100
2100	-	-	35	60-80	36	80-90	39	80-90
0000	-	-	34	60-80	40	80-90	33	60-80

Time	Precipitable Water (cm)	Precipitable Water (cm)	Precipitable Water (cm)	Precipitable Water (cm)	Four Station Mean
1500	2.95	3.77	4.17	3.26	3.54
1800	3.36	3.44	3.84	4.36	3.75
2100	3.53*	3.37	3.88	3.97	3.69
0000	3.39	3.65	4.12	3.20	3.59

* Surface to 575 mb only

pattern of thunderstorm development and dissipation.

4.1.4   Summary of 8 July 1977

The most important trigger in this case was the passage of the fronts through the raingage network and the study area. All the synoptic, subsynoptic and small-scale features were associated with the movement of these fronts.

A precipitation volume of 66,095 acre-ft, heaviest among four case-study days, was collected from rainfall during the hours the front passed through the study area. A rain band structure was clearly detectable in the precipitation and was oriented parallel to the front. This rain band structure was detected both in the M-33 PPI displays at Snyder and in the satellite imagery. The rain areas, especially the heavy rain area, were located under the brightest clouds (with albedos greater than 0.63) having the highest cloud tops (with cloud tops cooler than -50 C, corresponding to a 12-km height).

Two individual times when the rain band passed through the study area on this day were selected to study RHI cross sections of the M-33 data. In each case, a comparison was made between cloud tops inferred from the radar echoes and from satellite infrared data. Rainfall estimates from a Z-R relationship were also compared to those recorded by the raingages. The agreement of these

two comparisons was found to be quite good.

Small-scale features on this day provided worthwhile information on thunderstorm development and dissipation associated with movement of the fronts. The soundings showed that the atmosphere was almost saturated and there was a large positive area for free convection at 1800 GMT when the thunderstorms developed. The diamond shape found in the sounding at 2100 GMT enlarged by 0000 GMT 9 July, and could be associated with the dissipating stages of the thunderstorms.

4.2 Case study of 22 June 1977

Three separate data sets, satellite, radar and raingage, were available for study and comparison on this day. The following discussion concentrates on the results of a composite presentation of satellite and raingage data. The WSR-57 radar at Midland provided radar information in the form of precipitation patterns near the ground. As in the previous case study, synoptic and sub-synoptic features are discussed on this day.

4.2.1 Review of Synoptic Conditions

A high pressure center was located over the Great Lakes and two stationary fronts extended from a weak low pressure center in the Texas Panhandle at 1500 GMT on 22 June (Figure 4-18a). One front extended through the
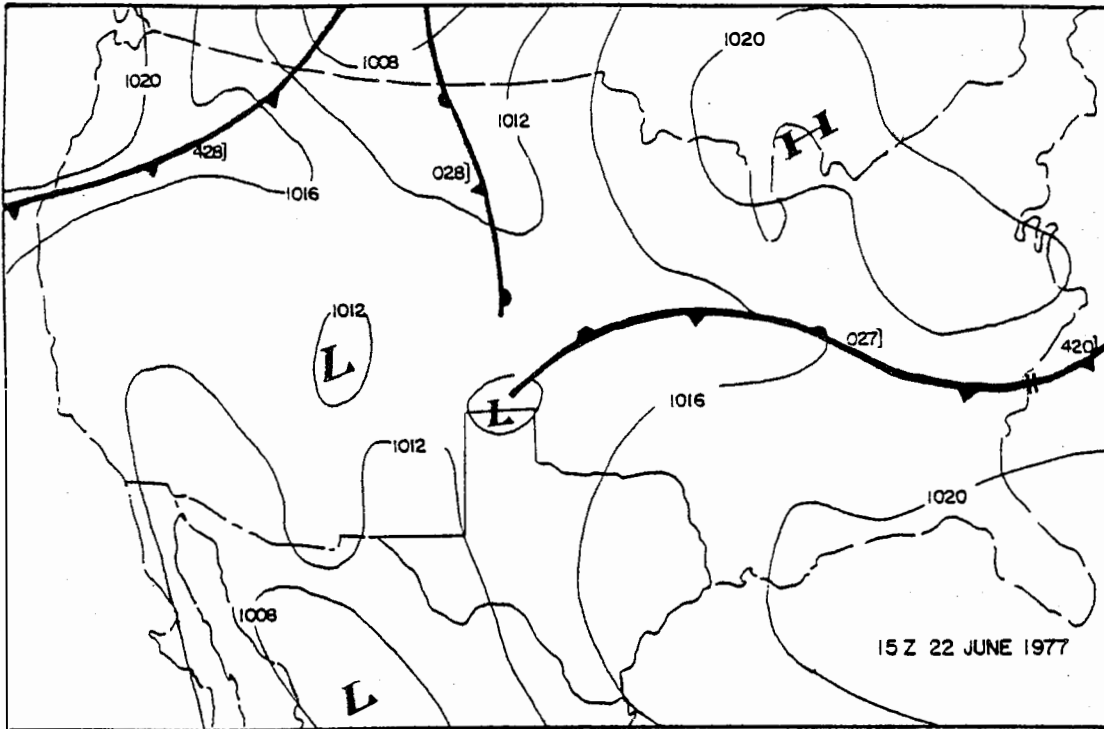
(a)
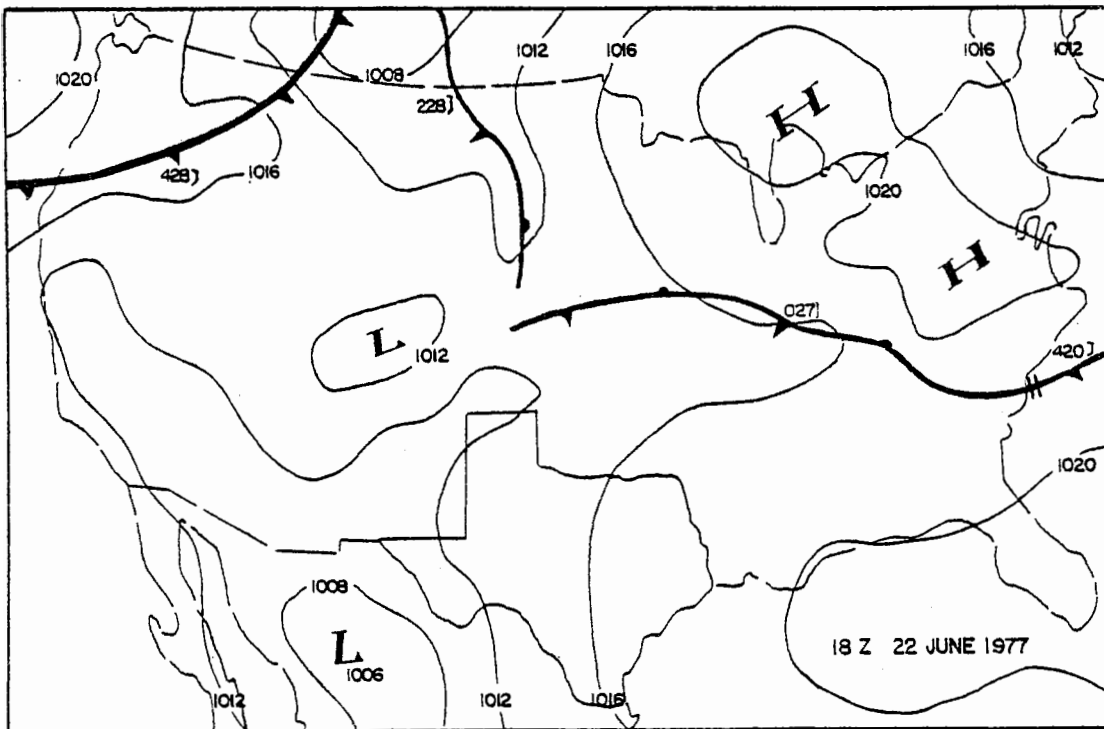
(b)

Figure 4-18   Surface synoptic charts on 22 June 1977.

(c)

21 Z 22 JUNE 1977

(d)

00 Z 23 JUNE 1977

Figure 4-18 Continued

central United States to the Atlantic Ocean, while the
other reached towards Canada. The weak low pressure
center disappeared and both fronts moved slowly to the
north, three hours later. Meanwhile, the high pressure
center remained over the Great Lakes area, and a new one
developed over Virginia. Over the next six hours
(Figure 4-18c and d) a slow movement of the frontal
systems continued toward the northeast.

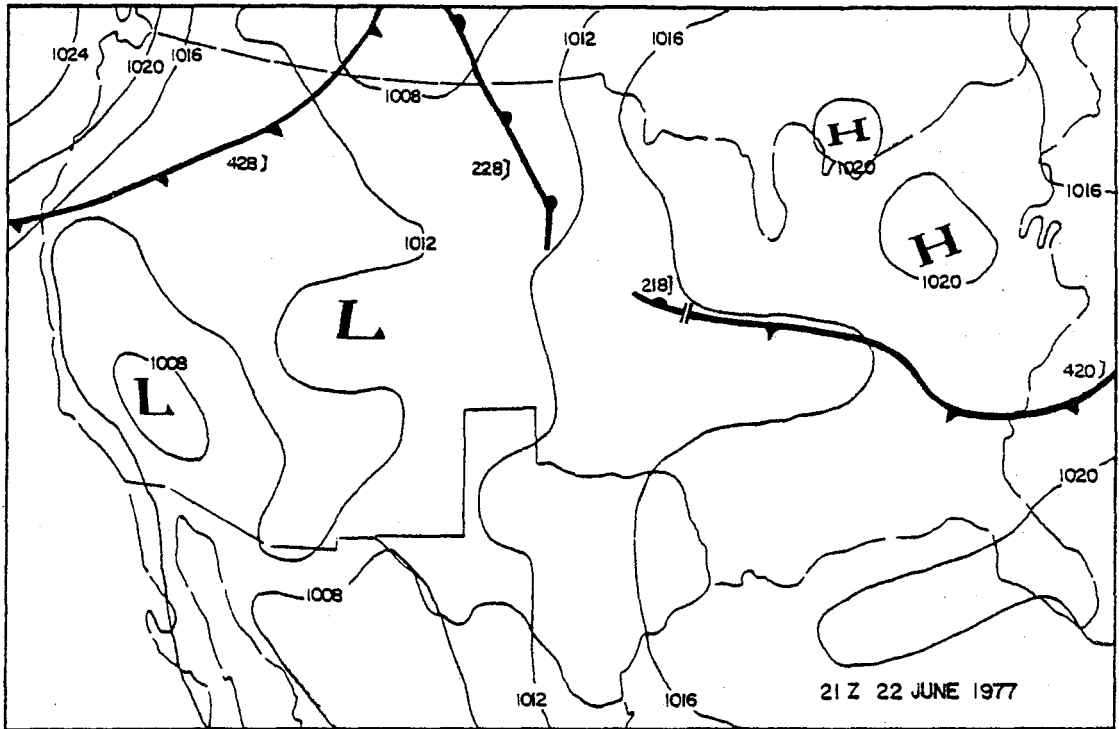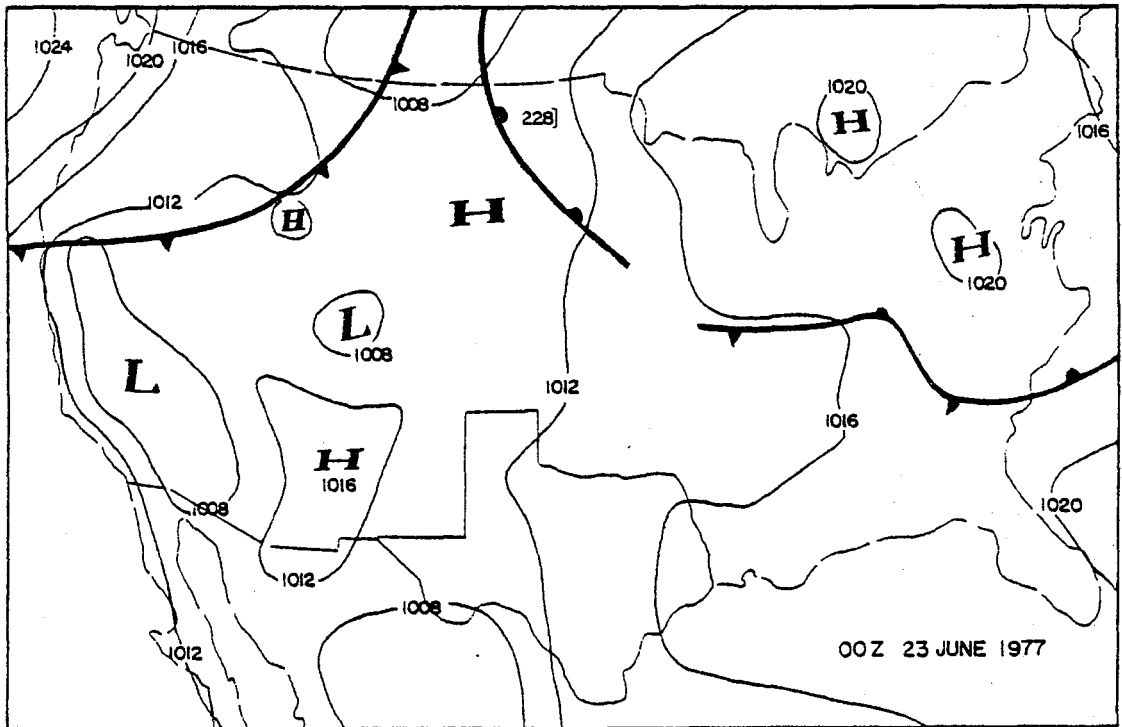The 500-mb pattern at 1200 GMT 22 June shows a cold
region over Louisiana (Figure 4-19a). The 5820 and 5880
gpm contours steered the flow into the study area from
central America. A weak trough passed through Colorado
and Arizona toward the northern High Plains with warm air
advection from south of the study area. The trough moved
slowly and the air flow into the study area continued from
the south at 0000 GMT 23 June (Figure 4-19b). The
temperature and contour patterns are quite similar at the
times considered.

4.2.2 Subsynoptic Features

4.2.2.1 Precipitation Analysis

Surveying the available data from the raingage
network, the precipitation on 22 June was separated into
three periods for discussion: 0400-0600 GMT, 1800-2030 GMT
and 2030-0000 GMT. The rainfall intensity increased from
period 1 to period 3 and then decreased rapidly after
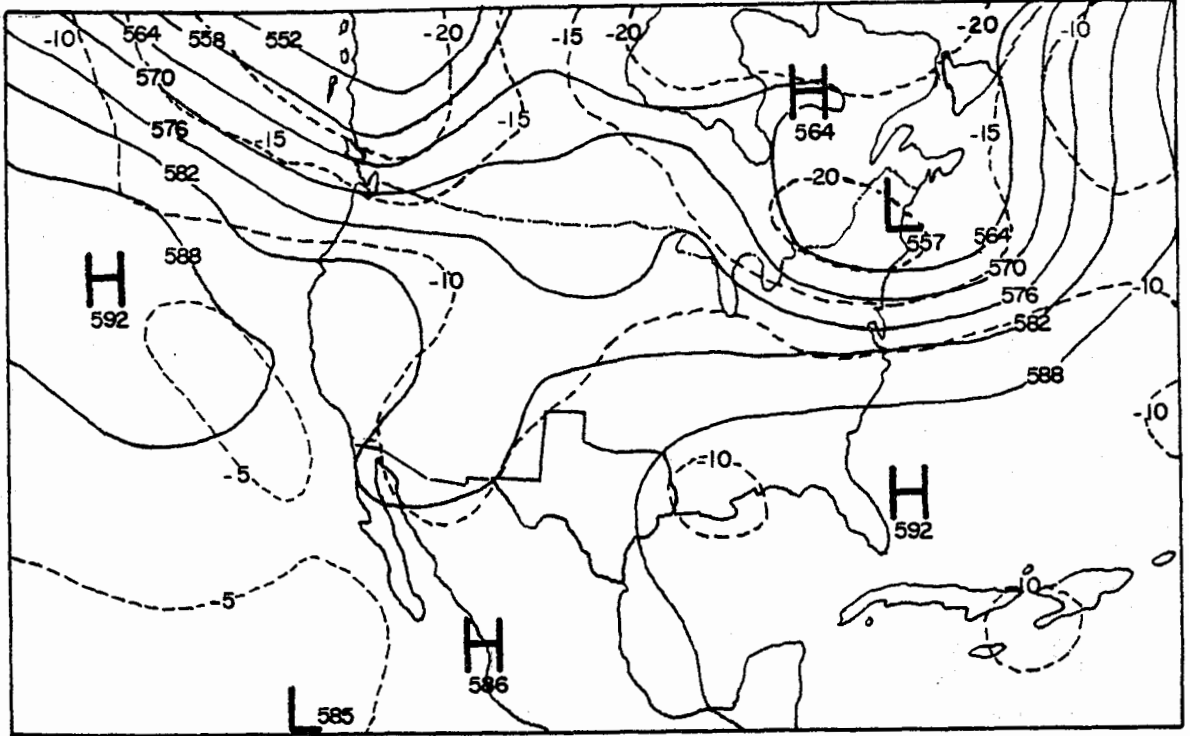
(a) 500 mb   12 Z   22 JUNE   1977
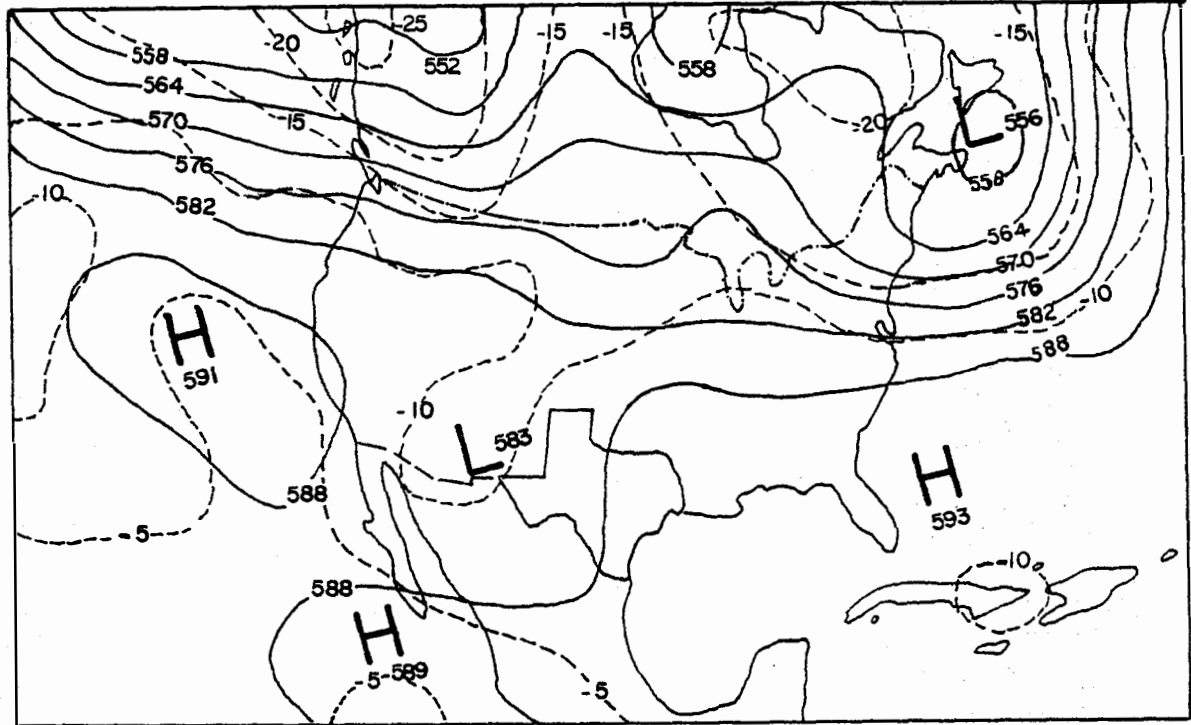
(b)   500 mb   00 Z   23 JUNE   1977

Figure 4-19   500-mb charts on 22 June 1977.   Codes
are the same as Figure 4-2.

period 3. Because both visible and infrared satellite
data were available for the period from 1800 to 0000 GMT,
the analysis of rainfall on 22 June considered periods 2
and 3 only. The variation with time of total precipi-
tation volume on 22 June is shown in Figure 4-20. The
spatial pattern of total precipitation during the period
from 1800 GMT to 0000 GMT 23 June shows that the rainfall
intensity increased from southwest to northeast (Figure
4-21). The rainfall distribution indicated that most of
the heavy rain was concentrated in the eastern portion of
the raingage network; a maximum rainfall during the 6-hour
period of 1.69 inches was recorded south of Snyder. The
analysis of raingage data on this day was complicated
because the heavy rain occurred so close to the eastern
edge of the network. The total surface water generated
from precipitation during the analysis period was
estimated to be 52,987 acre-ft (Haragan, et al., 1979).

4.2.2.2 Mesonetwork Observations

An analysis of surface temperatures (Scoggins, et al.,
1979) showed the passage of a squall line occurred within
the study area between 1500 and 2200 GMT. Temperatures on
this day were noticeably cooler because of the reduced
surface heating from cloudiness associated with the squall
line (see Figure 2-3 and Figure 3-1). The analysis also
indicated that centers of surface mixing ratio and
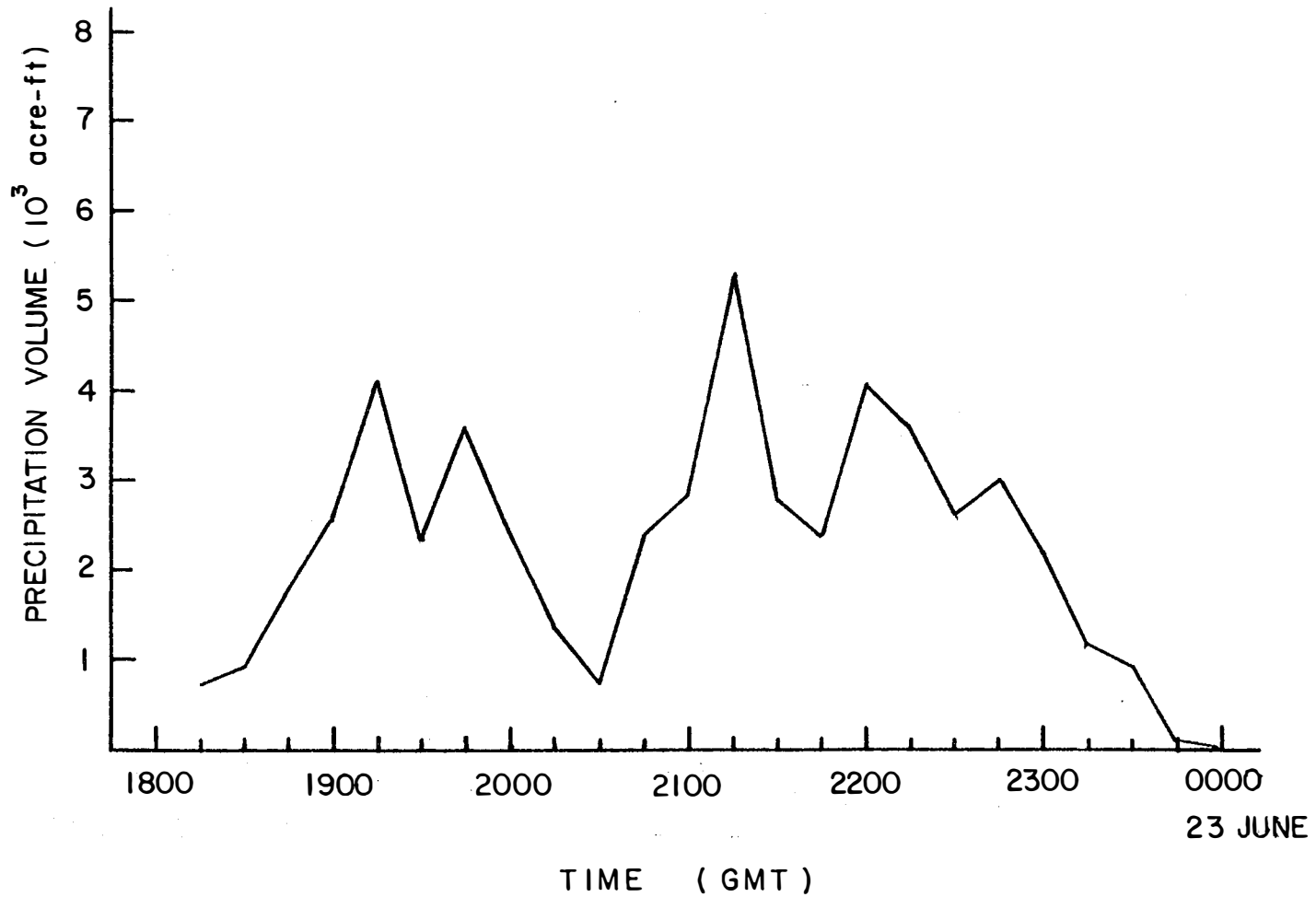equivalent potential temperature were associated with

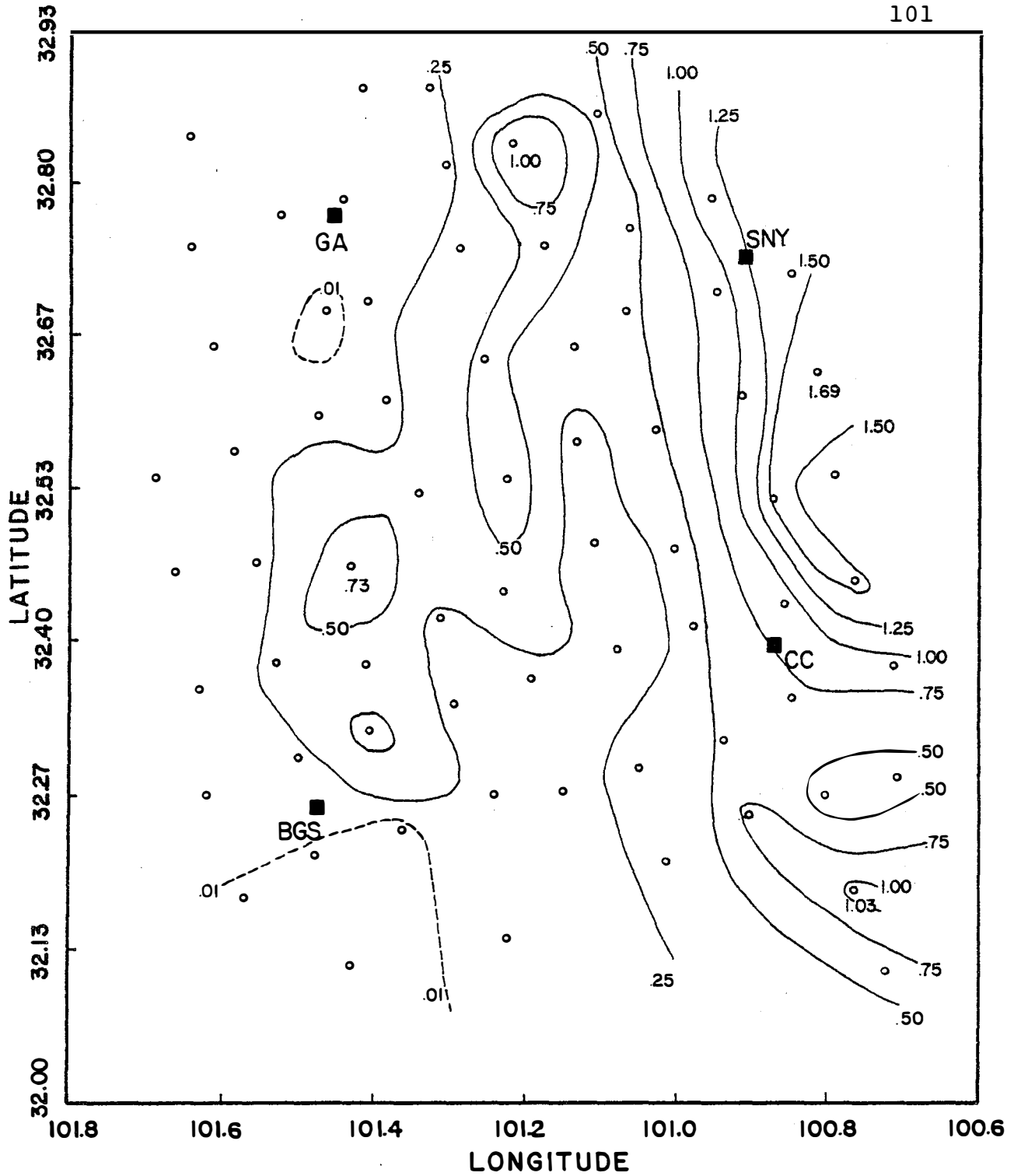Figure 4-20 Variation of total network precipitation with time on 22 June 1977.

Figure 4-21 Same as Figure 4-4 for 22 June 1977.

the squall line. A stream line analysis for 22 June
(Figure 4-22) indicates that surface convergence was also
associated with the squall line. Vertical profiles of
mass divergence, vertical motion, moisture divergence and
the horizontal flux of latent heat energy all indicated
that these features were concentrated within the lowest
300-mb layer. In a study of a squall line which passed
through the mesonetwork of the National Severe storms
Laboratory (NSSL), Ogura and Liou (1979) have pointed out
that the major features at low levels are strong inflow
into the squall line in the front and surface convergence
along the wind shift line. They also observed that the
precipitation rate experienced a sharp maximum near the
surface gust front and precipitation was confined to a
relatively limited area. Reviewing the precipitation
analysis for 22 June, the rain area movement approximately
followed the rear edge of the squall line. It is signifi-
cant that the precipitation observed on 22 June was
produced by the line of convective clouds associated with
the squall line.

4.2.2.3 Discussion of Midland Radar
         PPI Displays

The National Weather Service WSR-57 radar observations
from Midland were available to verify the information
derived from the satellite radiance data and raingage
measurements (Figure 4-23). The precipitation analysis
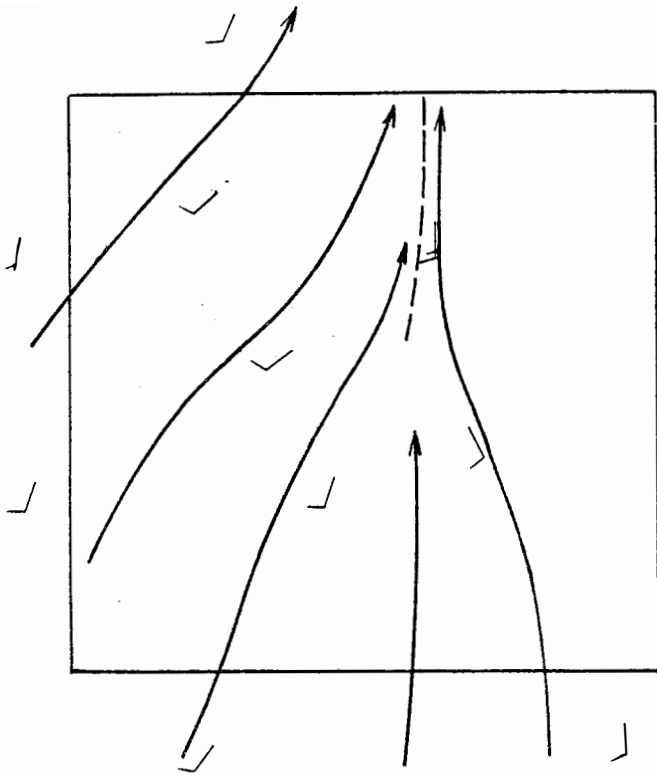
(a) 1900 GMT
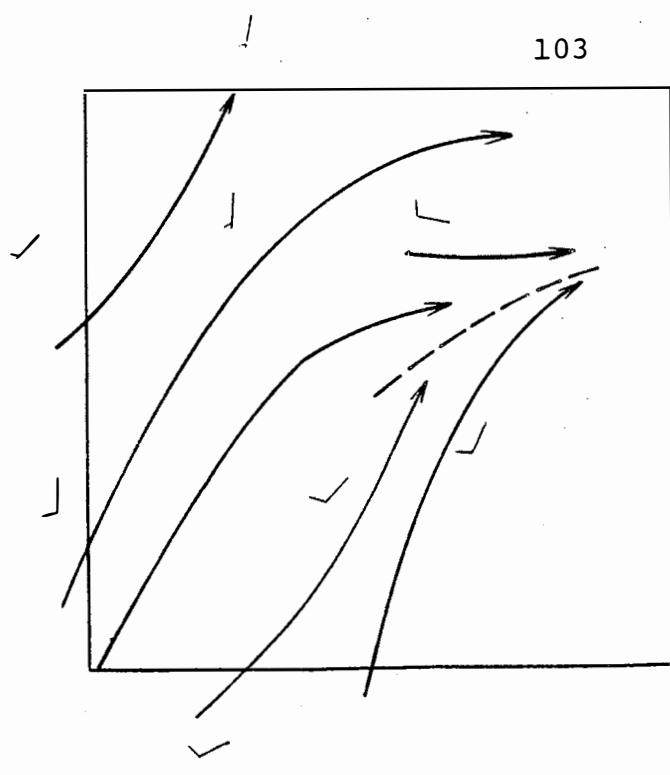
(b) 2000 GMT
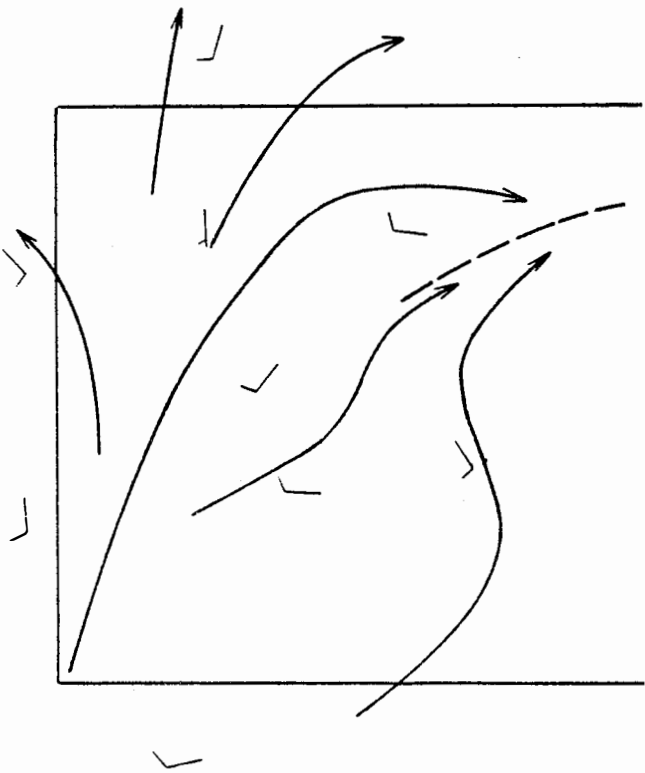
(C) 2100 GMT
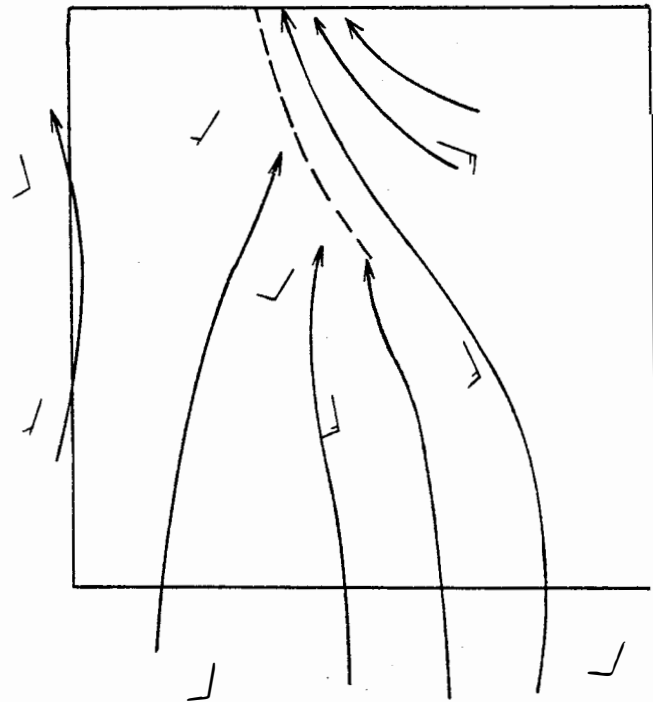
(d) 2200 GMT

Figure 4-22 Surface stream line analysis on 22 June
1977. The boundary indicates the extent
of the raingage network, while dashed
lines indicate lines of convergence.
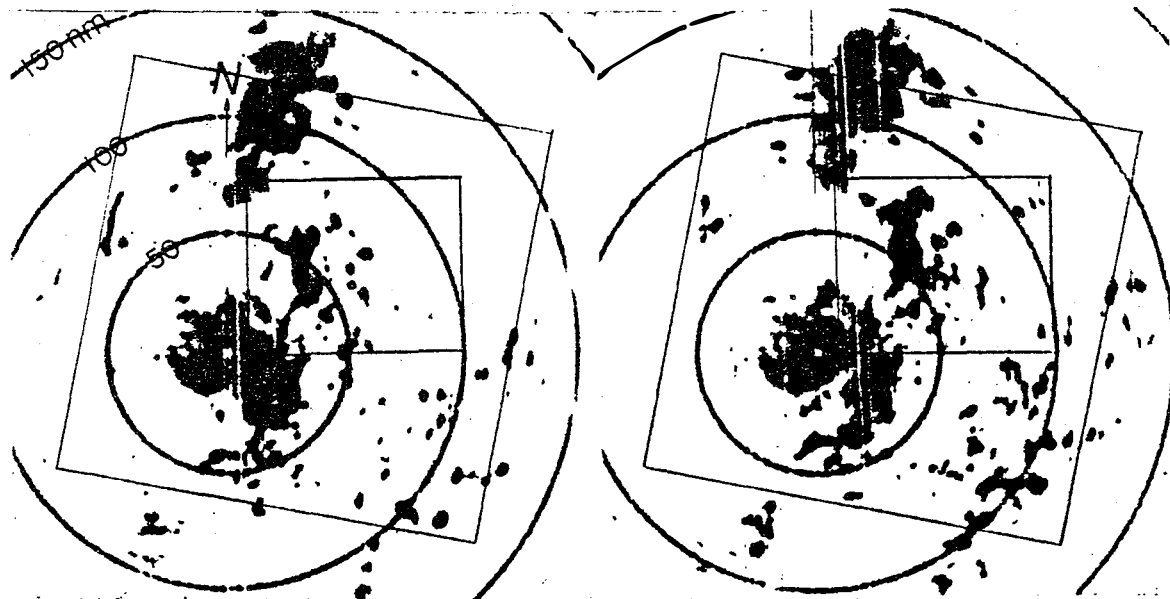
(a)   1815 GMT

(b)   1845 GMT
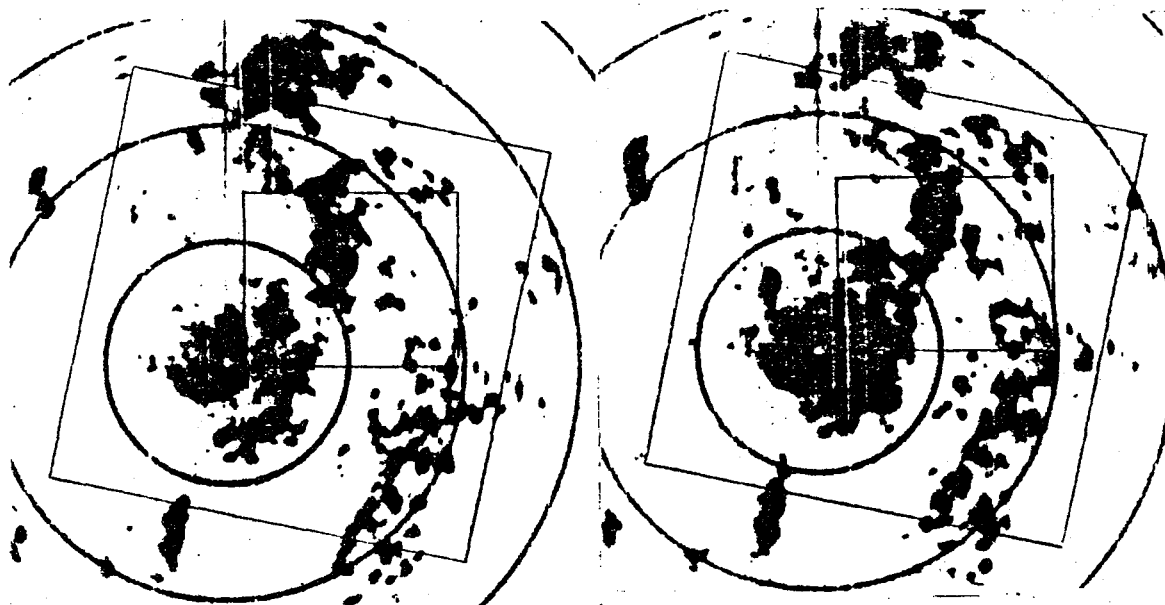
(c)   1915 GMT

(d)   1945 GMT

Figure 4-23   PPI displays on 22 June 1977 from the
National Weather Service radar at Midland.
The outside square boundary designates the
study area, while the inner box marks the
raingage network.
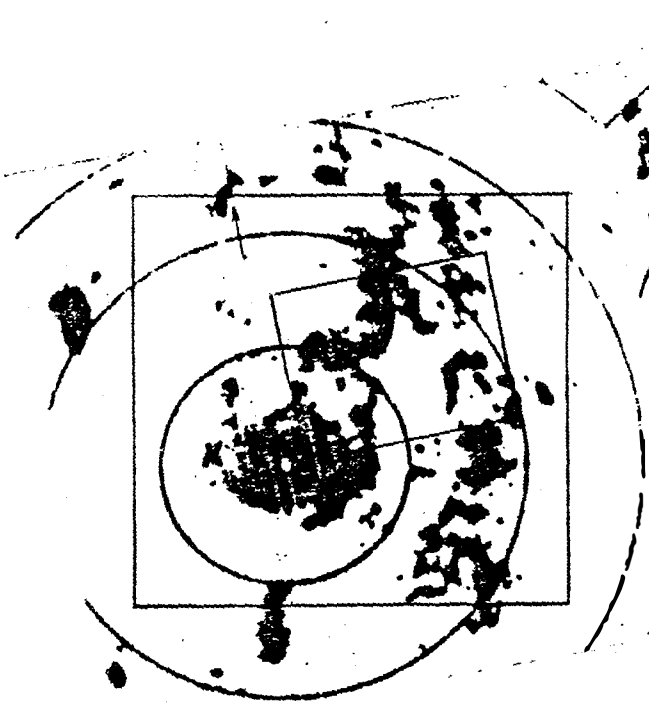
(e) 2015 GMT

(f) 2045 GMT
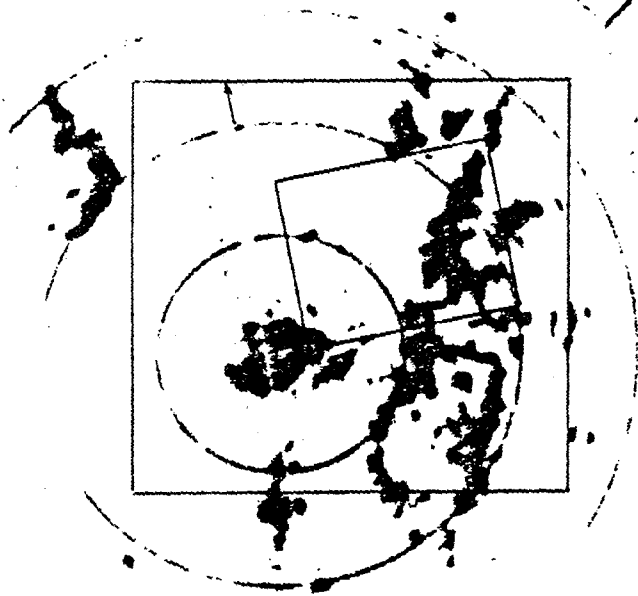
(g) 2115 GMT
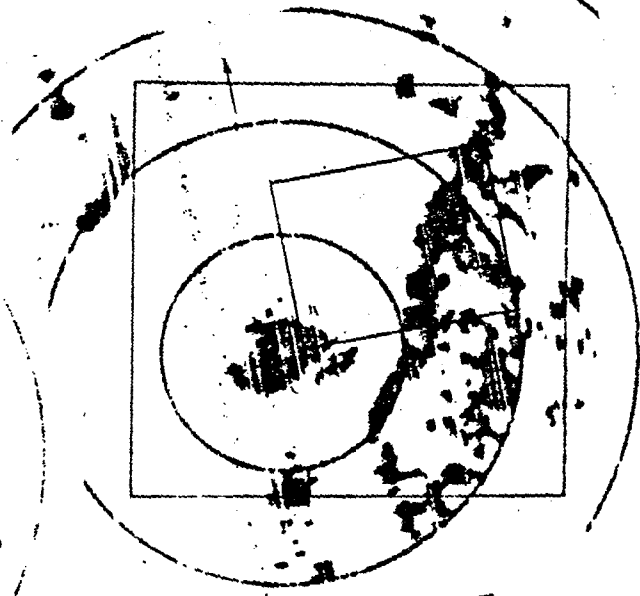
(h) 2145 GMT

Figure 4-23 Continued

for 22 June (Figure 4-20) indicated that rain began at 1800 GMT, reached peak intensity at 1915 GMT and then decreased until 2015 GMT. During this period, most of the radar echoes occupied the western portion of the raingage network. A check of individual raingage records showed that the secondary maximum of rainfall shown in Figure 4-21 in the western portion of the raingage network was associated with this maximum rainfall intensity occurrence. It is noteworthy that the primary echoes within that portion of the raingage network changed in size and intensity in phase with the time-variation of rainfall amount. Figure 4-20 also showed that the rainfall began to increase again at 2045 GMT and reached another peak at 2115 GMT. Rain continued, but decreased in intensity toward zero by 0000 GMT 23 June. The sequence of PPI radar displays during this period (Figure 4-23 e, f, g, h) shows that the primary echoes had now moved into the eastern portion of the raingage network and study area. Rainfall data for raingages in the eastern portion of the network showed maximum rainfall intensities occurred during this later period. Thus, the large isohyet values found in Figure 4-21 along the eastern edge of the raingage network corresponded to the late afternoon precipitation maximum. As should be reasonable to expect, the images of visible and infrared radiance data displayed on the ADVISAR showed this portion

was covered by both high and bright clouds.

4.2.2.4 Visible and Infrared Radiance Data Combined with Rainfall Records

From the sequence of diagrams in Figure 4-24, it can be seen that much of the study area was occupied by bright clouds, larger than 0.63 albedo, with high cloud-tops above 10 km. Note that only the coldest or two coldest isotherms are shown in any given frame in this figure. The precipitation analysis located the rain area in the northwestern corner of the raingage network, nearly beneath the bright and high-topped clouds at 1815 GMT. The cloud system then moved to the north and, as the cloud tops grew higher, the area of bright cloud and high cloud tops enlarged. At the same time, the rain area enlarged and the intensity became stronger, attaining the precipitation peak for the second period of 22 June at 1915 GMT (Figure 4-20). The rain intensity then weakened, as the bright and high-topped clouds moved out of the raingage network. By 2030 GMT the rain had reached a minimum intensity because the bright or high-topped clouds had left the network.

The precipitation intensity began to increase again at 2045 GMT. The rain area had now shifted to the eastern edge of the raingage network because a new storm cell had entered the network from the southeast. Meanwhile, the third precipitation period of 22 June had started and the
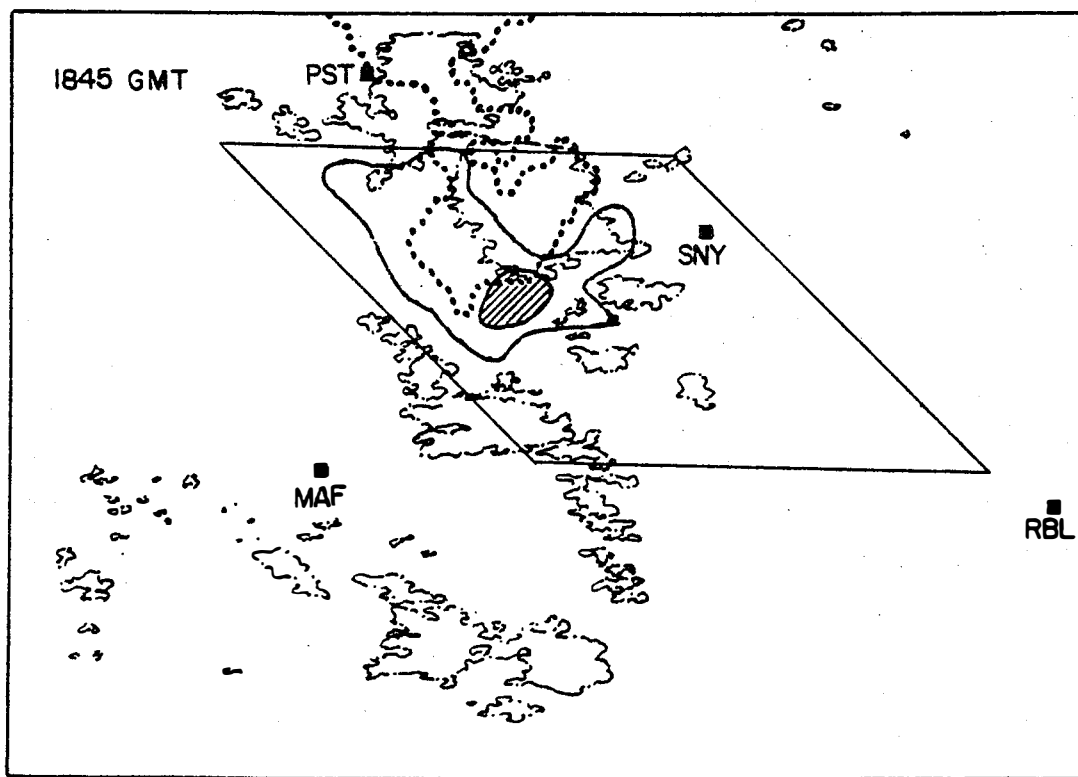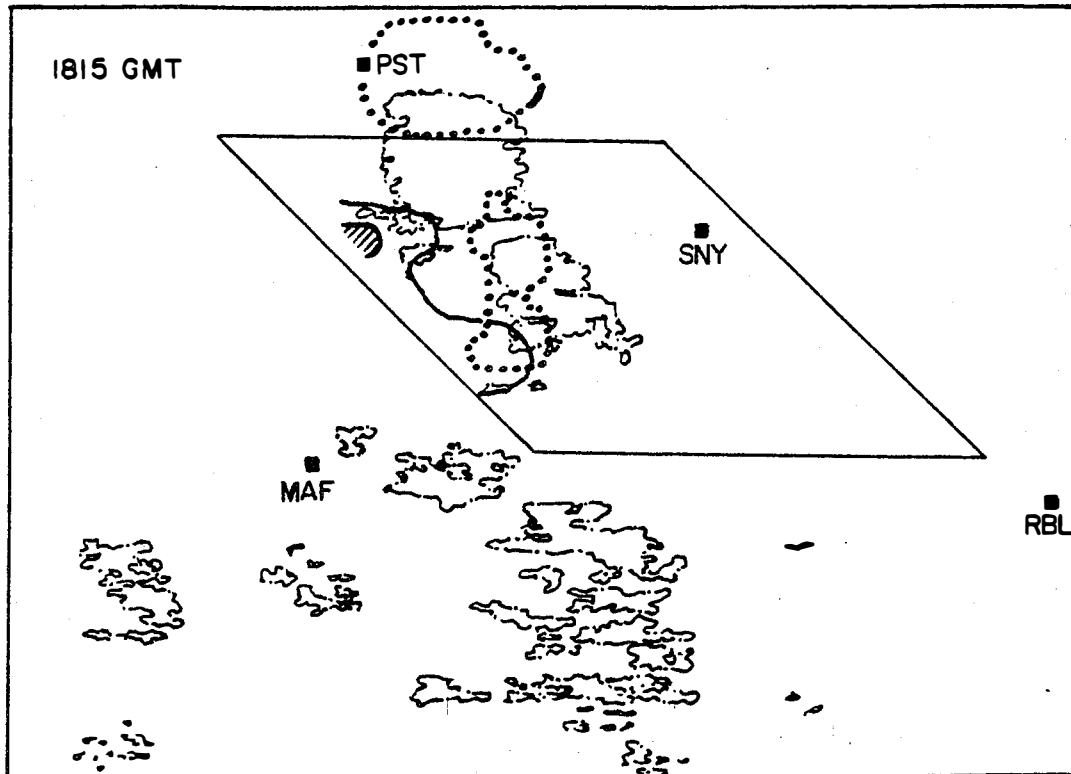
Figure 4-24   Cloud albedo, cloud top temperature and
             rainfall intensity on 22 June 1977. The
             explanatory code is given in Figure 4-6.

1915 GMT

PST

SNY

MAF

RBL

1945 GMT

PST

SNY

MAF

RBL

Figure 4-24   Continued

2015 GMT
PST
SNY
MAF
RBL

2045 GMT
PST
SNY
MAF
RBL

Figure 4-24   Continued

2115 GMT

PST

SNY

MAF

RBL

2145 GMT

PST

SNY

MAF

RBL

Figure 4-24   Continued

2215 GMT
PST
SNY
MAF
RBL

2245 GMT
PST
SNY
MAF
RBL
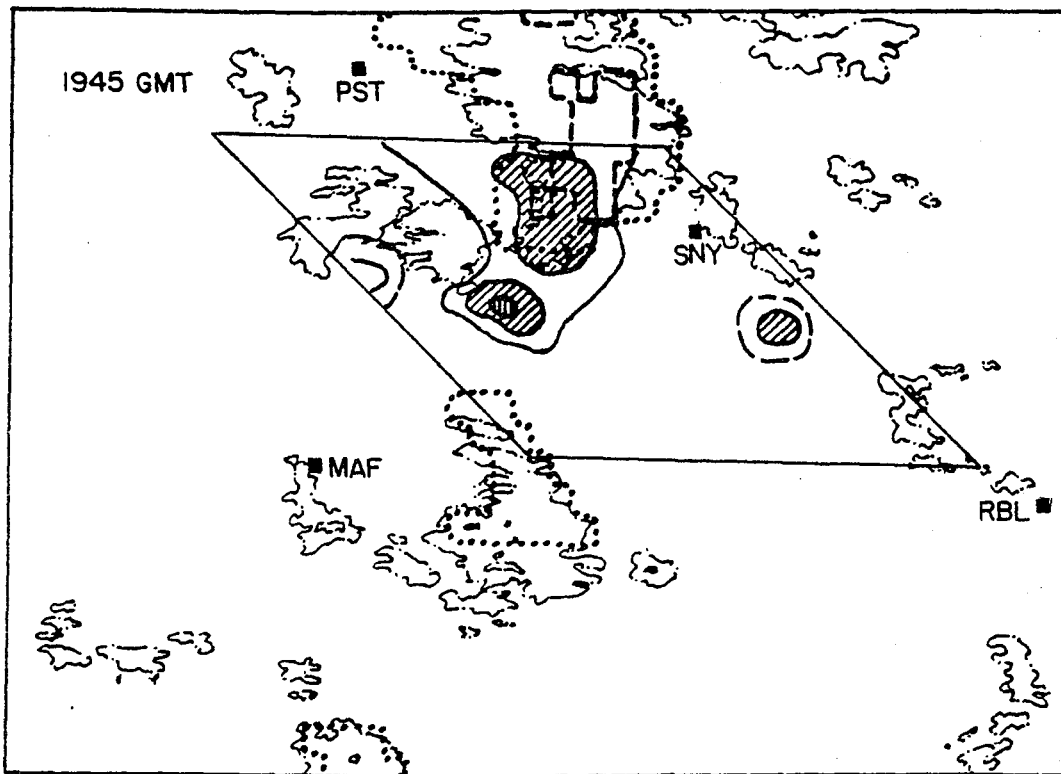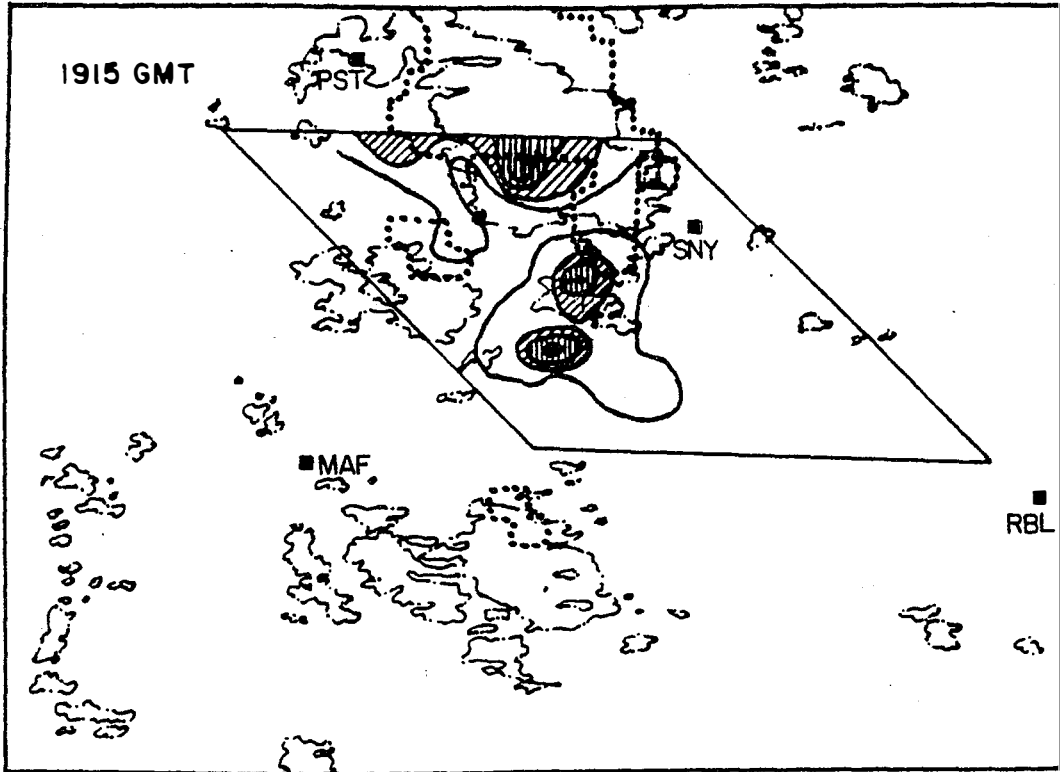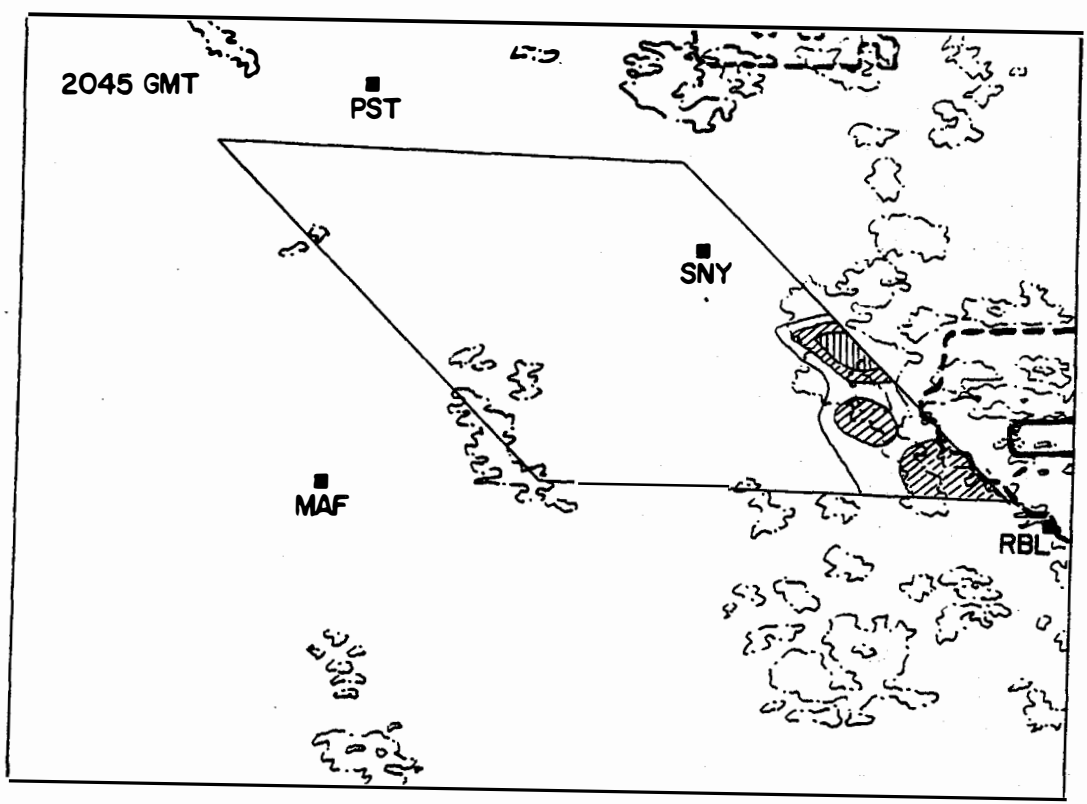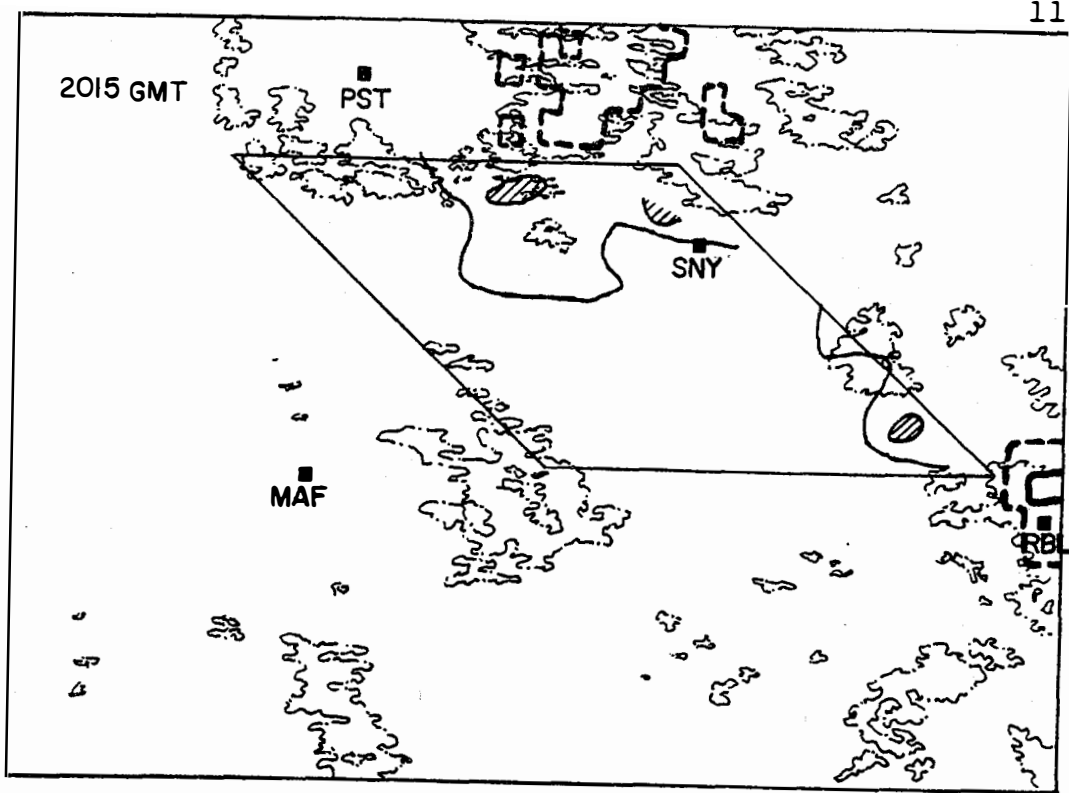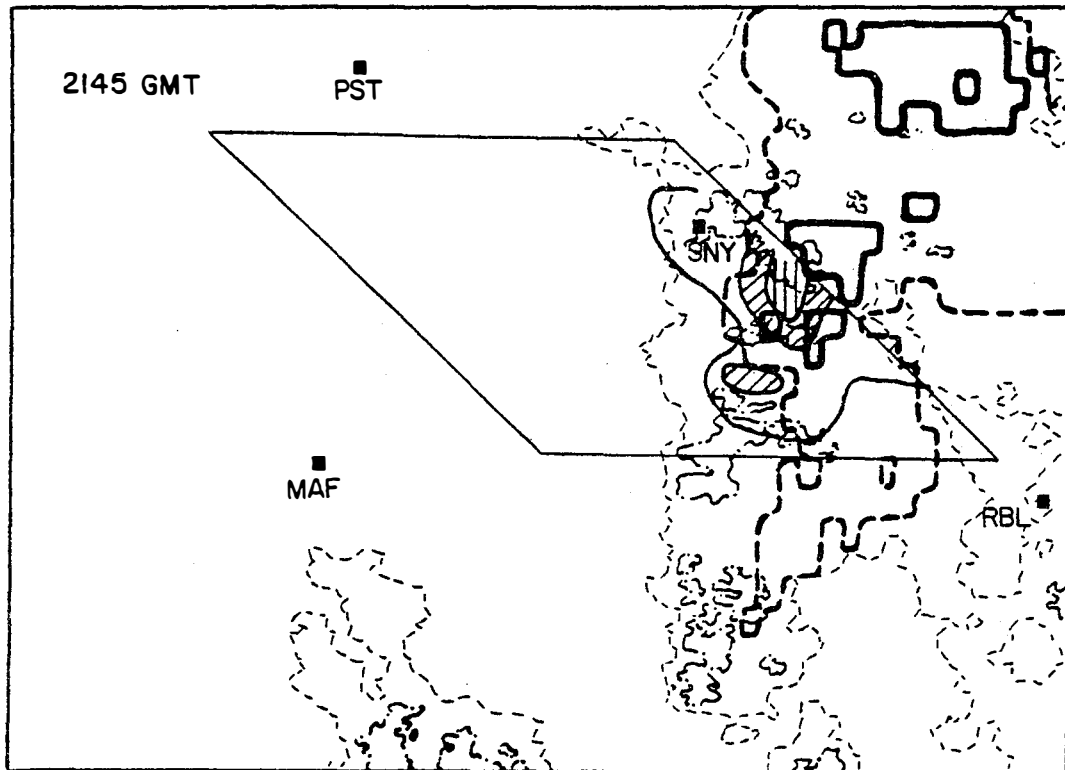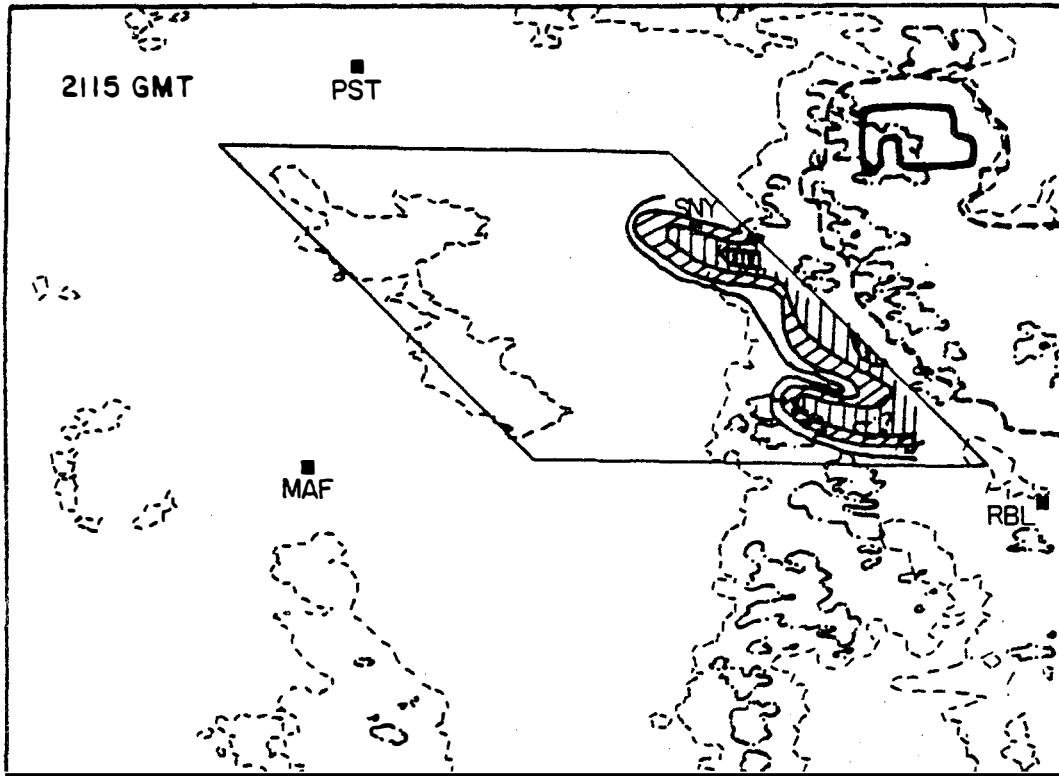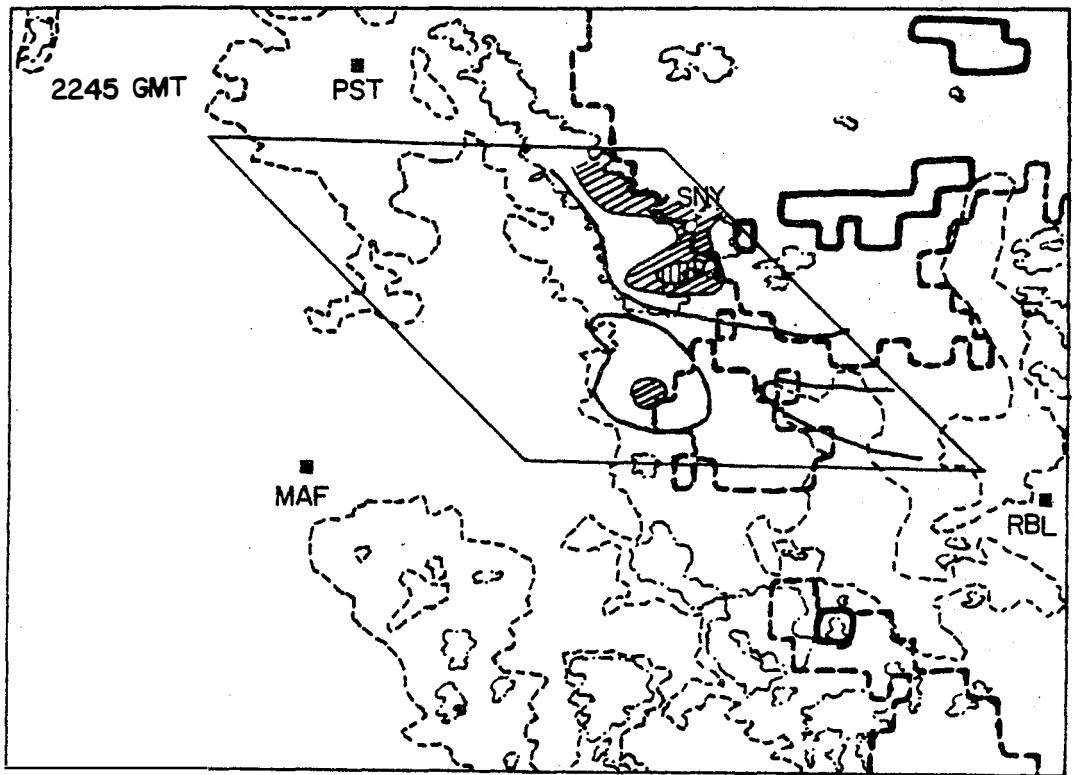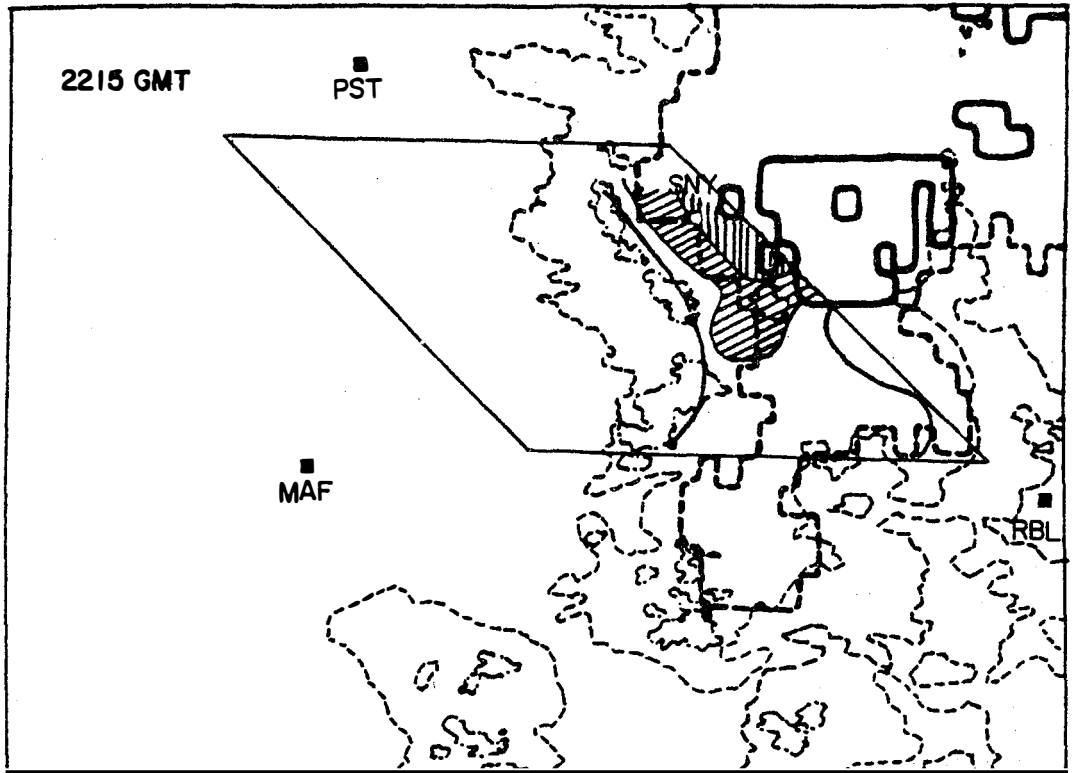
Figure 4-24   Continued

precipitation maximum recorded at 2115 GMT was 0.52 inch
for the previous 15 minutes. This peak rainfall can be
matched to a cloud with vertical development higher than
14 km just beyond the eastern boundary of the raingage
network. The extent of the raingage network is quite
limited, and it is probable that more precipitation.
occurred under that portion of the high cloud-top region
which was outside the network, as the rainfall pattern
at 2115 GMT implies. The precipitation decreased after
the bright and high-topped cloud moved and became wide-
spread. During this late afternoon period on 22 June, the
precipitation area was still under the high and bright
clouds, although the rainfall intensity was not as strong
as at the peak of 2115 GMT.

4.2.3 Small-scale Features

  4.2.3.1 Review of Soundings

    Figure 4-25 shows the Big Spring soundings on 22 June.
At 1500 GMT there was a small negative area indicating
stable conditions; but, instability developed as the
surface temperature rose in the afternoon. The lowest
500-mb layer was nearly saturated and there was a large
positive area and no negative area by 1800 GMT; free
convection was now most likely. The atmosphere had become
somewhat drier at upper levels and the surface temperature
was cooler by 2100 GMT. The increased stability at this
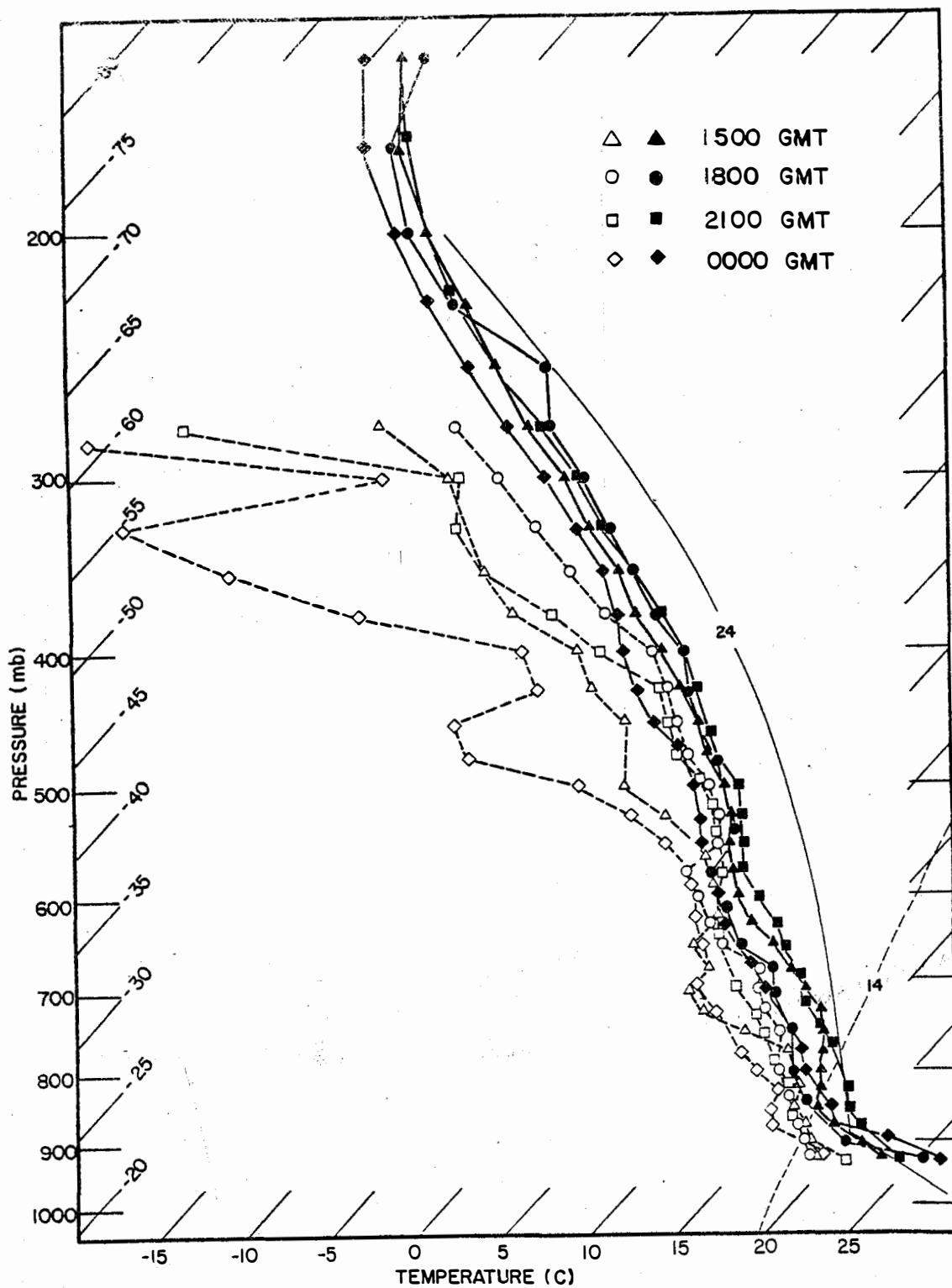
Figure 4-25 Atmospheric soundings taken at Big Spring
on 22 June 1977. Codes are the same as
Figure 4-17.

time was a result of the precipitation observed during the preceding several hours. By 0000 GMT 23 June unstable conditions were again observed, indicating that surface temperatures had recovered somewhat.

4.2.3.2 K-index and Precipitable Water Values

The K-indices calculated from sounding data, the corresponding suggested thunderstorm probabilities and the precipitable water within the layer from the surface to 500 mb are listed in Table 4-3. The values of K-index were greater than 35 in most cases, and close to 40 in some instances, with an overall average of 36. The high probability of thunderstorm occurrence meant that extensive convective activity was expected on this day. The average value of precipitable water for all four stations on this day was 3.83 cm, even greater than the 3.64 cm average value noted earlier for 8 July 1977. In fact, values of water vapor remained high in the lower layers throughout the day, indicating the presence of convective activity (Scoggins, et al., 1979).

4.2.4 Summary of 22 June 1977

The synoptic conditions did not provide a strong mechanism for the generation of precipitation, but the passage of a squall line through the study area produced precipitation on 22 June. The rainfall on 22 June was

Table 4-3

K-indices, suggested thunderstorm probabilities
and precipitable water on 22 June 1977.

Time (GMT)	Midland K-index	Midland Prob.(%)	Post K-index	Post Prob.(%)	Robert Lee K-index	Robert Lee Prob.(%)	Big Spring K-index	Big Spring Prob.(%)
1500	36	60-80	38	80-90	31	60-80	31	60-80
1800	39	80-90	34	60-80	36	80-90	36	80-90
2100	34	60-80	36	80-90	-	-	35	60-80
0000	33	60-80	39	80-90	37	80-90	34	60-80

	Precipitable Water (cm)	Precipitable Water (cm)	Precipitable Water (cm)	Precipitable Water (cm)
1500	3.95	3.96	3.42	4.08
1800	3.87	3.69	3.92	3.97
2100	3.64	3.82	3.69	4.00
0000	3.53	3.99	4.18	3.57

less intense and persisted for a longer time when compared with 8 July. The mechanism of precipitation generation on this day was quite different from that on 8 July, which was caused by the passage of fronts.

The satellite and radar information showed close agreement on the location of rainfall. Both data sets also showed that the first rainfall peak was produced by the cells in the western portion of the raingage network, while the second rainfall peak was produced later by cells in the eastern portion.

The sequence of diagrams in Figure 4-24 followed the variation of precipitation with time on this day. The diagrams also showed the location of rainfall areas with respect to the brightest and highest clouds. The rain areas, especially the most intense ones, were located under the bright and cold-top clouds, similar to the case on 8 July. The large albedo area (greater than 0.63) was more narrow on this day, representative of the mesoscale squall line, than the broader pattern of 8 July when the activity was generated by the slow-moving fronts.

The small-scale features such as the atmospheric soundings at Big Spring, the K-index and precipitable water values were similar to those on 8 July. A small negative area existed in the 22 June morning sounding and free convection developed as the surface temperature rose in the afternoon. However, the diamond shape

observed in the lower layer of the 8 July soundings did
not appear on this day. Both the K-indices and the
precipitable water values were as high as those on 8 July.

4.3 Case Study of 24 June 1977

4.3.1 Review of Synoptic Conditions

A mid-latitude cyclonic system dominated the weather
over the United States on 24 June 1977. An occluded front
was located north of the Great Lakes area, while fronts
extended from this point through the central and eastern
United States (Figure 4-26a). A trough from Iowa passed
through Kansas into Texas, north of the study area at
1500 GMT. Both the occlusion and trough had disappeared
by 1800 GMT and the cold front moved closer to the Texas
area (Figure 4-26b). The warm front remained nearly
stationary while the cold front moved southeastward and
reached the Panhandle of Texas at 0000 GMT 25 June (Figure
4-26c and d). In addition, a line of instability was
located between the cold and warm fronts at 0000 GMT
25 June. The percent cloud cover in the study area
increased rapidly during the late afternoon on 24 June,
as discussed in Chapter 3; this occurred as thunderstorms
which developed to the south moved into the study area.

The upper level pattern at 1200 GMT 24 June showed
a cold region over the Arizona area (Figure 4-27a). The
air flow entered the study area along the 5880 gpm contour.
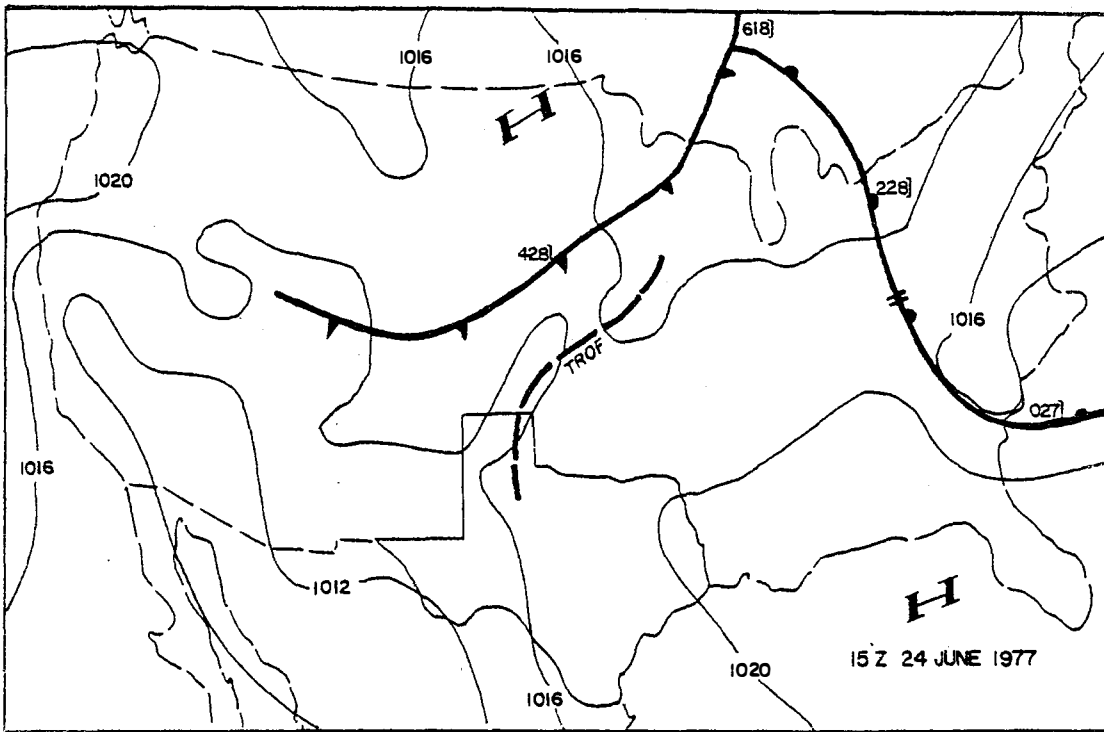
(a)
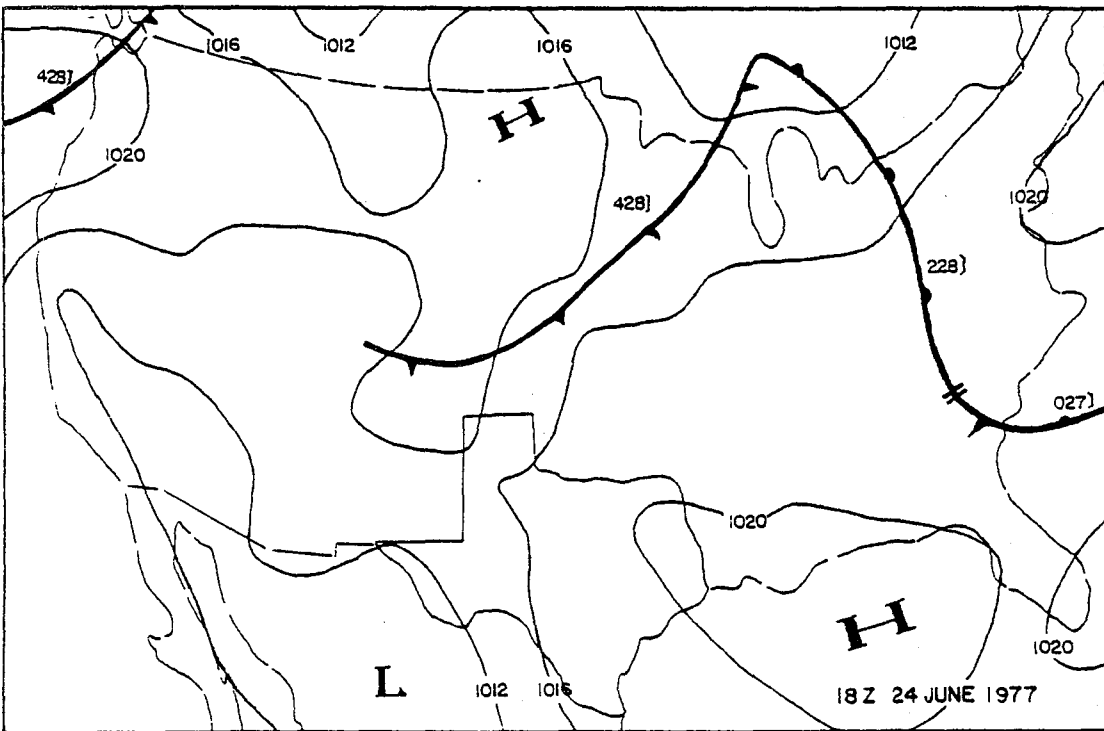
(b)

Figure 4-26   Surface synoptic charts on 24 June 1977.

(c)

(d)

Figure 4-26 Continued
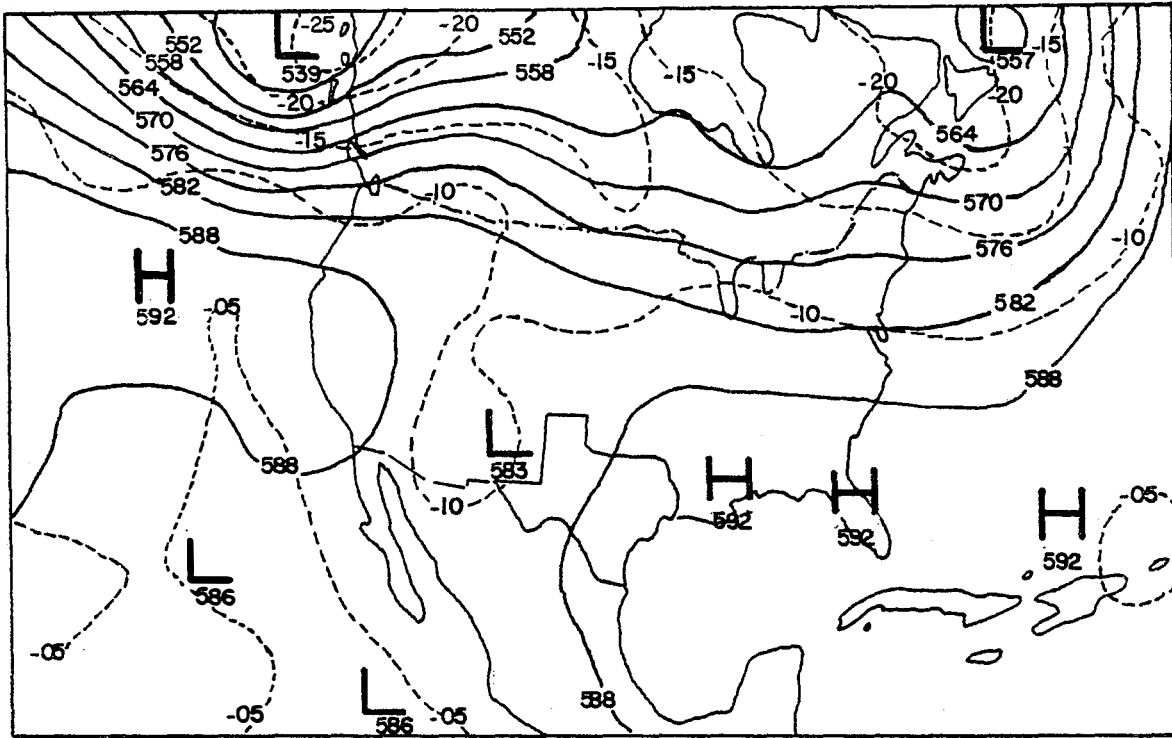
(a)   500 mb   12 Z   24 JUNE   1977
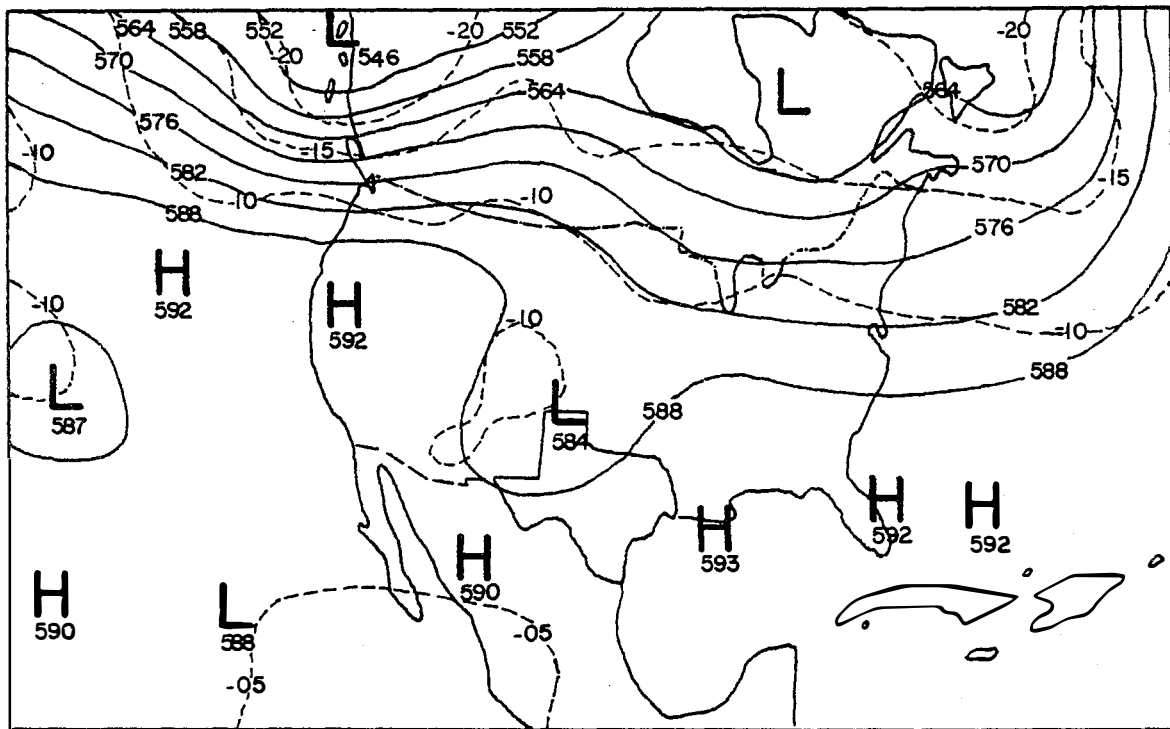
(b)   500 mb   00 Z   25 JUNE   1977

Figure 4-27   500-mb charts on 24 June 1977.   Codes
are the same as Figure 4-2.

By 0000 GMT 25 June, two 5880 gpm contours had connected to form a new east-west contour and air flow passed through the study area along this new contour (Figure 4-27b). A warm area (-5 C) located off the western coast of California at 1200 GMT had moved southward into Mexico by 0000 GMT 25 June. There was a low pressure center over the Texas Panhandle area and a trough extended to another low pressure region over Canada.

4.3.2 Subsynoptic Features

4.3.2.1 Precipitation Analysis

Only four stations within the raingage network recorded rainfall from 1800 GMT to 0000 GMT 25 June 1977 (Figure 4-28). The estimate of total precipitation for this period is 1,617 acre-ft, only 2% of what was collected on 22 June and 8 July. The subsequent discussions show that a thunderstorm entered the study area in the late afternoon, but did not pass through the raingage network.

4.3.2.2 Discussion of Midland Radar Displays and Satellite Imagery

The precipitation echoes observed by the WSR-57 radar at Midland show that a thunderstorm cell moved into the study area from the southwest after 2145 GMT (Figure 4-29). There was no apparent thunderstorm activity inside the raingage network during this period. Both visible and
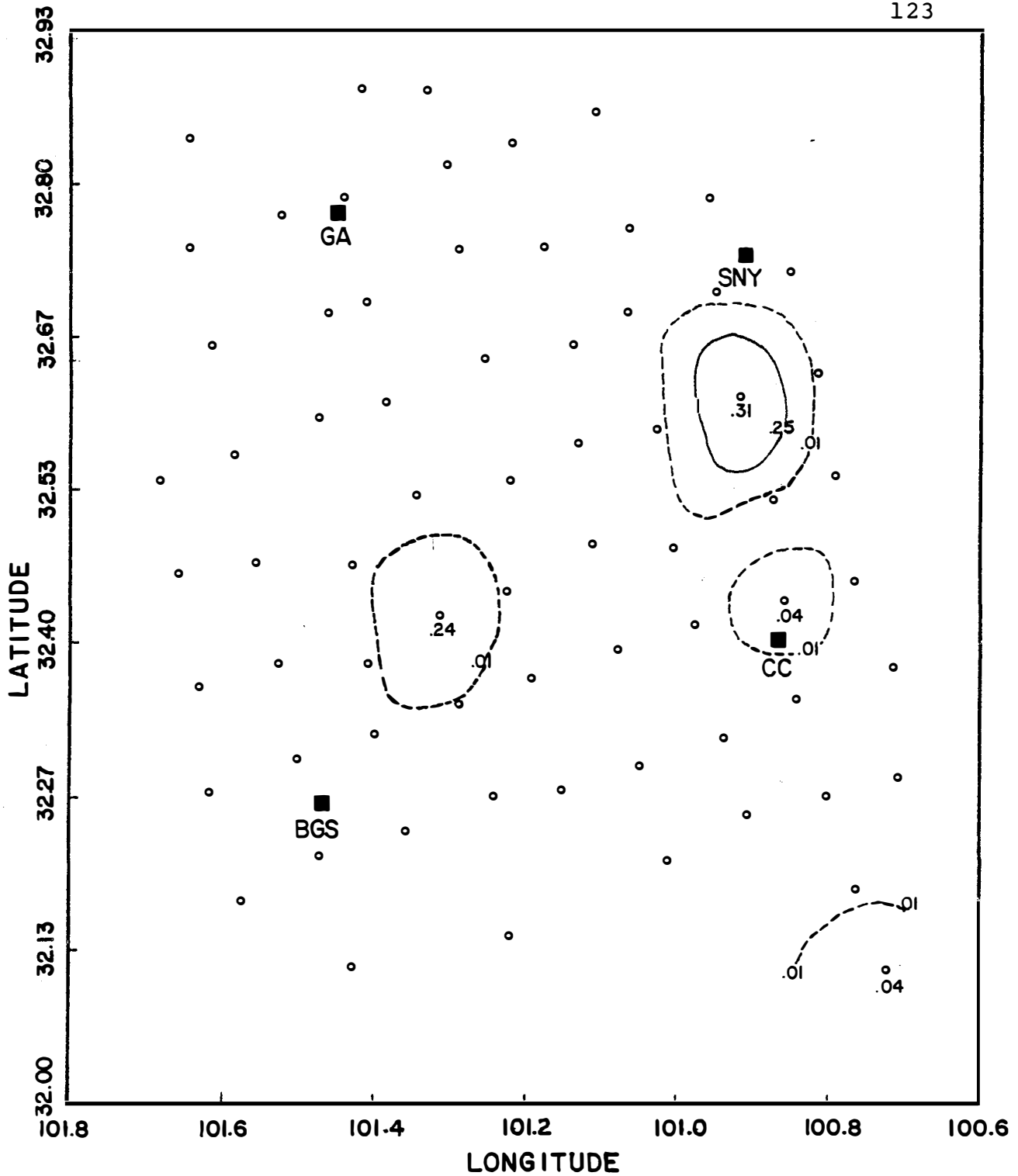
Figure 4-28   Same as Figure 4-4 for 24 June 1977.
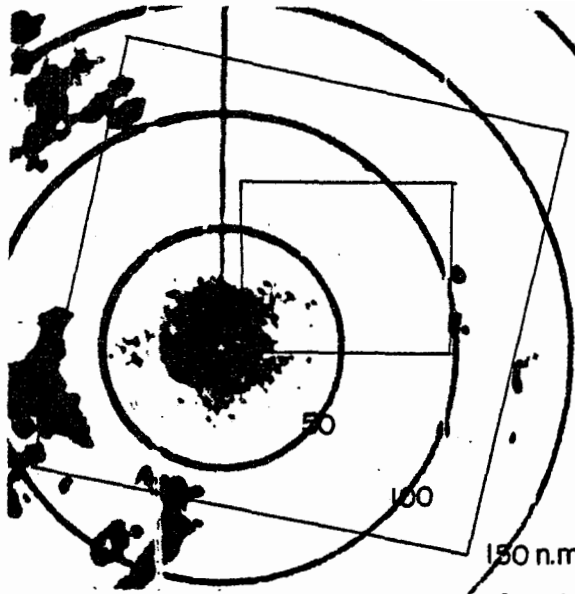
(a) 2145 GMT
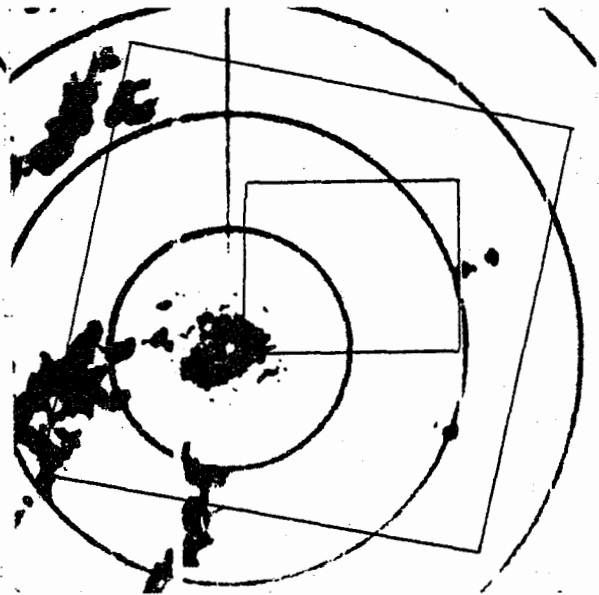
(b) 2215 GMT
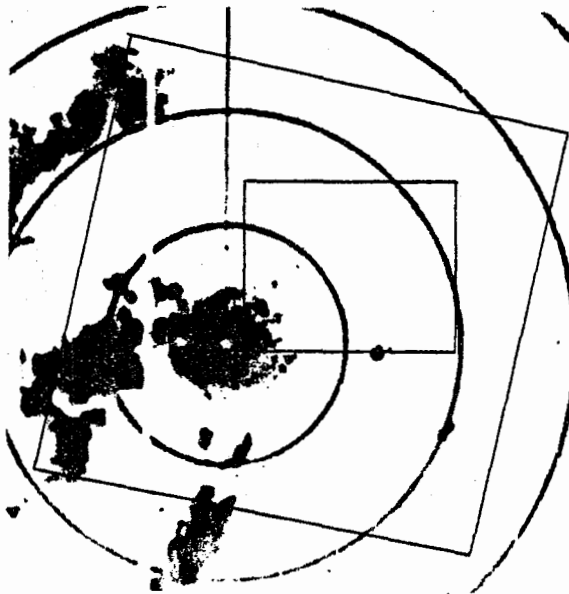
(c) 2245 GMT

(d) 2315 GMT

Figure 4-29   PPI displays on 24 June 1977 from the
National Weather Service radar at Midland.
The boundaries are the same as Figure 4-23.

infrared satellite data offered evidence that a thunder-
storm cell migrated into the study area at this time
(Figure 4-30). The vertically-developed storm cell with
cloud top temperatures between -50 and -60 C,
corresponding to a 12.5 km height, dominated the study
area cloud cover in the late afternoon. The cloud cover
was larger than 80% during this period (Figure 3-1).

4.3.2.3 Mesonetwork Observations

The mesonetwork surface temperature data revealed
that an intense line of convective activity formed near
the southwestern corner of the study area after 2100 GMT
on 24 June (Scoggins, et al., 1979). Thunderstorm
activity increased rapidly by 0000 GMT 25 June and strong
centers of convergence and divergence were observed in
association with the thunderstorm. No thunderstorm
activity was observed by the mesonetwork before 2100 GMT
on this day.

4.3.3 Small-scale Features

4.3.3.1 Review of Soundings

The soundings on 24 June were drier compared to those
on 8 July and 22 June (Figure 4-31). At 1500 GMT a
shallow moist layer near the surface was capped by a weak
temperature inversion at 850 mb with dry conditions above
the inversion. As afternoon temperatures rose in the
lower layers, the opportunity for free convection
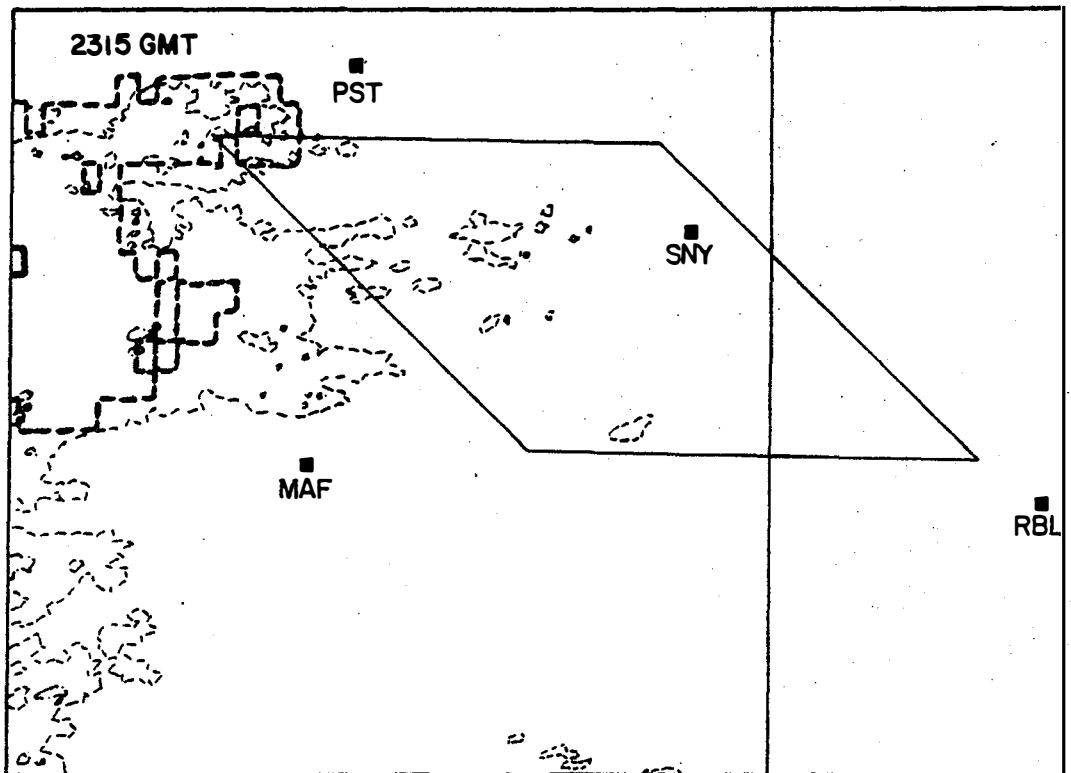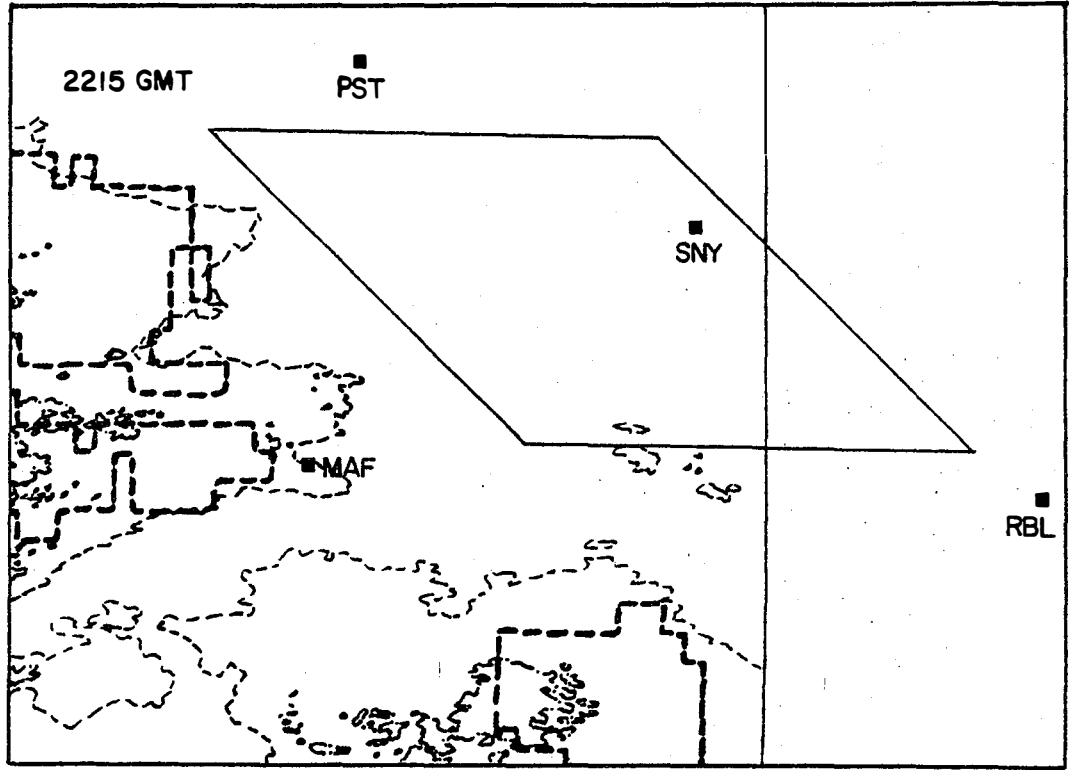
Figure 4-30   Cloud albedo and cloud top temperature
              at 2215 and 2315 GMT on 24 June 1977. The
              explanatory code is given in Figure 4-6.
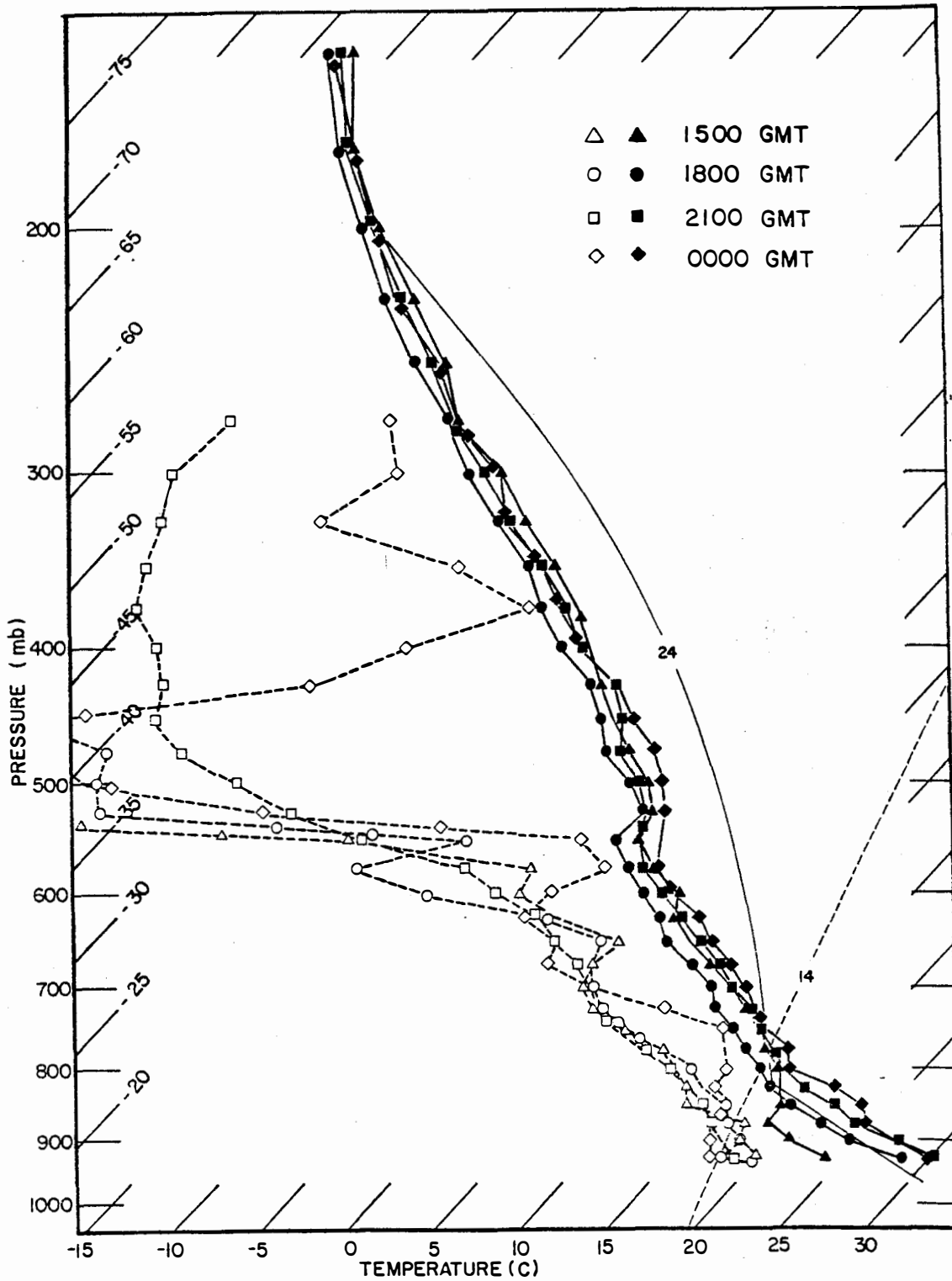
Figure 4-31 Atmospheric soundings taken at Big Spring on 24 June 1977. Codes are the same as Figure 4-17.

128

improved. However, the very dry conditions led to the need for considerable lifting before the potential instability could be released. The large negative area at 0000 GMT 25 June, for example, required 45 mb of lifting above the LCL before free convection could take place.

4.3.3.2 K-index and Precipitable Water Values

The K-indices calculated from sounding data, the corresponding suggested thunderstorm probabilities and precipitable water values are listed in Table 4-4. The high values of K-index and corresponding thunderstorm occurrence probabilities, especially during the late afternoon and at the more southerly stations of the study area, again indicated that extensive convective activity was expected on this day. Most of the precipitable water values calculated from the surface to the 500-mb level were greater than 3 cm on this day. However, the four-station average precipitable water value of 3.37 cm was substantially lower than the corresponding values for either 8 July or 22 June.

4.3.4 Summary of 24 June 1977

The weather features in this case were quite different from those on 8 July and 22 June. Although a thunderstorm did enter the study area in the late

Table 4-4

K-indices, suggested thunderstorm probabilities
and precipitable water on 24 June 1977.

Time (GMT)	Midland		Post		Robert Lee		Big Spring	
	K-index	Prob.(%)	K-index	Prob.(%)	K-index	Prob.(%)	K-index	Prob.(%)
1500	34	60-80	33	60-80	35	60-80	29	40-60
1800	39	80-90	34	60-80	38	80-90	35	60-80
2100	40	80-90	32	60-80	39	80-90	35	60-80
0000	37	80-90	33	60-80	37	80-90	34	60-80

Time	Precipitable Water (cm)	Precipitable Water (cm)	Precipitable Water (cm)	Precipitable Water (cm)
1500	2.85	3.31	3.83	3.15
1800	3.25	3.30	4.07	3.13
2100	3.24	2.92	3.79	3.06
0000	3.39	3.11	4.15	3.43

afternoon, no significant synoptic or subsynoptic conditions existed to produce rain on this day. Both radar and satellite information established that the thunderstorm entered the study area, but did not pass through the raingage network. The soundings were drier on this day than for the two earlier cases, the K-index remained high and the average precipitable water was lower than on 8 July and 22 June.

4.4 Case Study of 27 June 1977

It was seen in Figure 3-1 that the sky was clear until 1915 GMT and that percent cloud cover began to increase after 2015 GMT on 27 June. The discussion of this day proceeds in a manner similar to the previous cases, except for the important absence of a precipitation analysis, because there was just 0.05 inch of rain collected at a single station on this day.

4.4.1 Review of Synoptic Conditions

A cold front stretched from the central United States through Lake Superior into Canada, while a warm front extended into the Atlantic Ocean at 1500 GMT (Figure 4-32a). The fronts moved slowly to the north by 1800 GMT and then remained stationary until 2100 GMT. Over the Texas HIPLEX area, clear skies dominated into the early afternoon of 27 June. Weather conditions became unstable
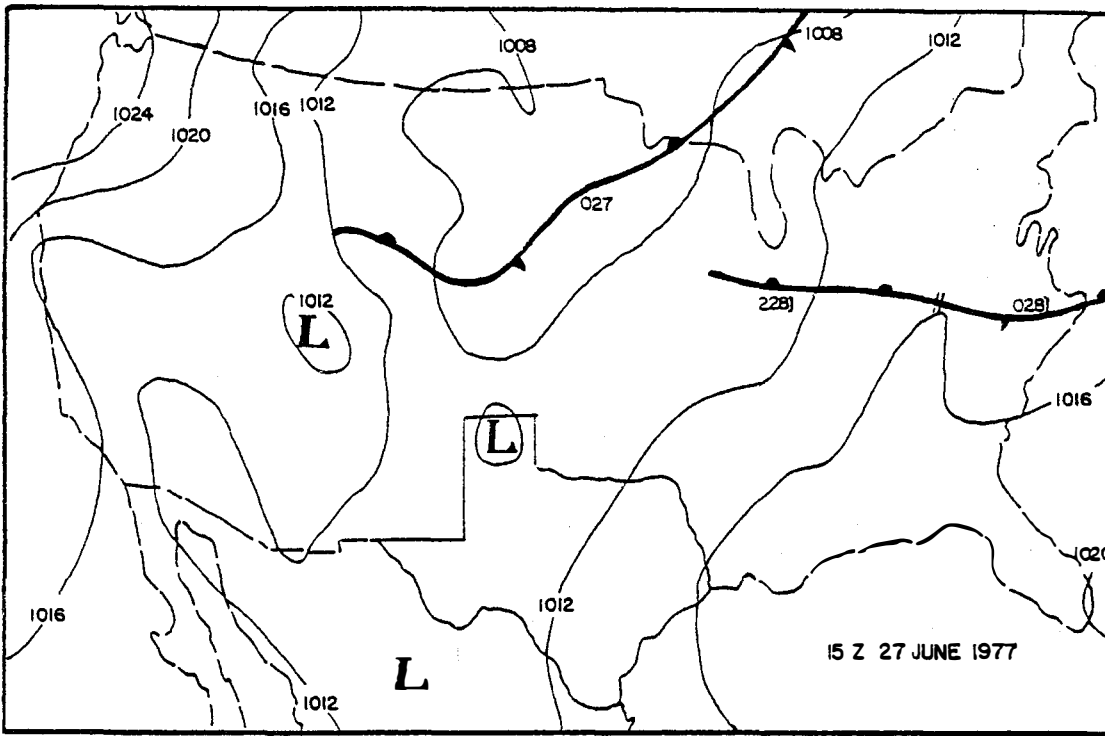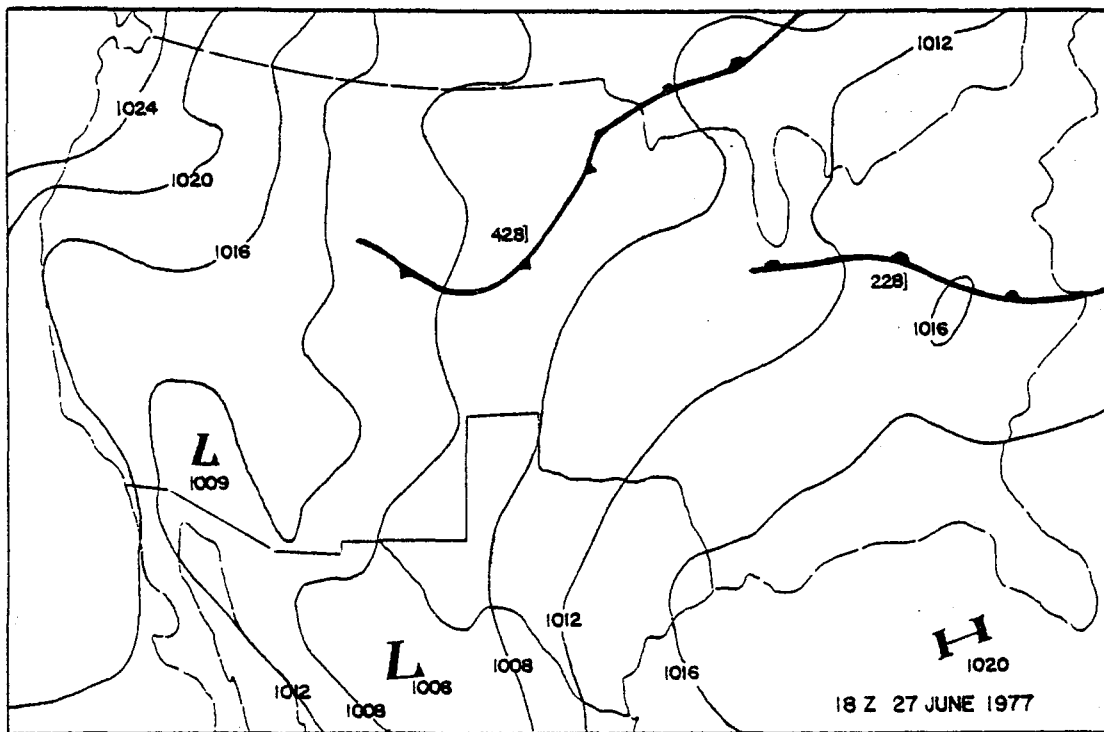
Figure 4-32   Surface synoptic charts on 27 June 1977.
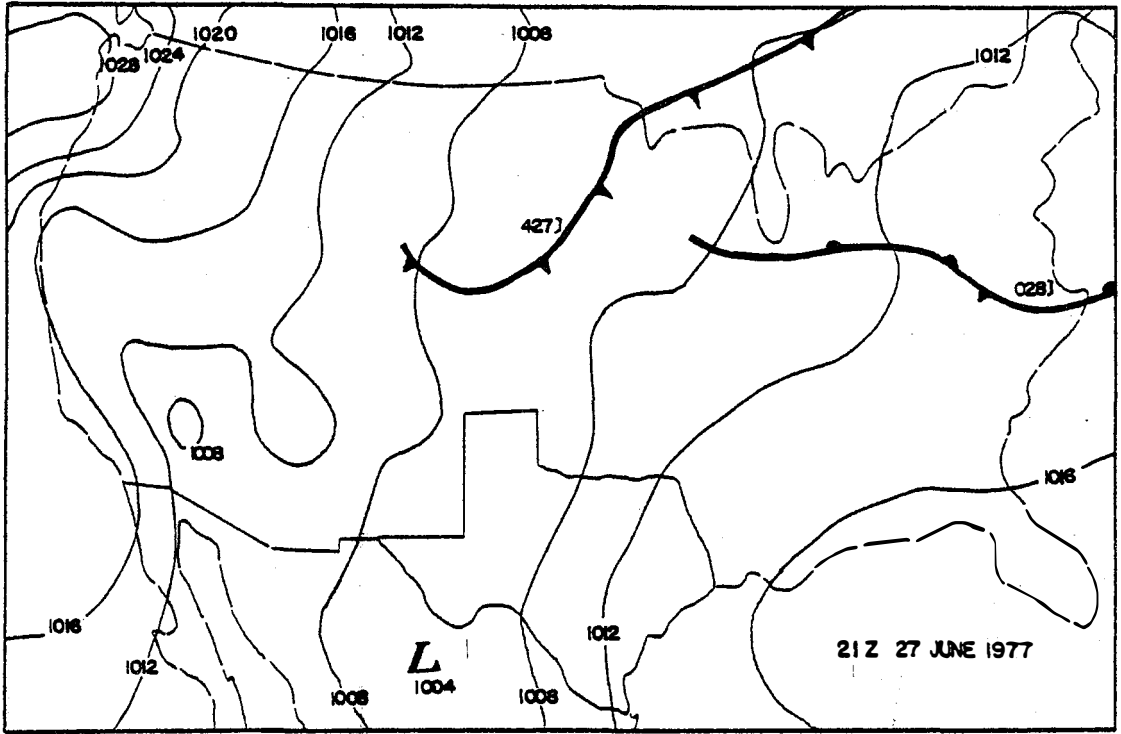
(c)
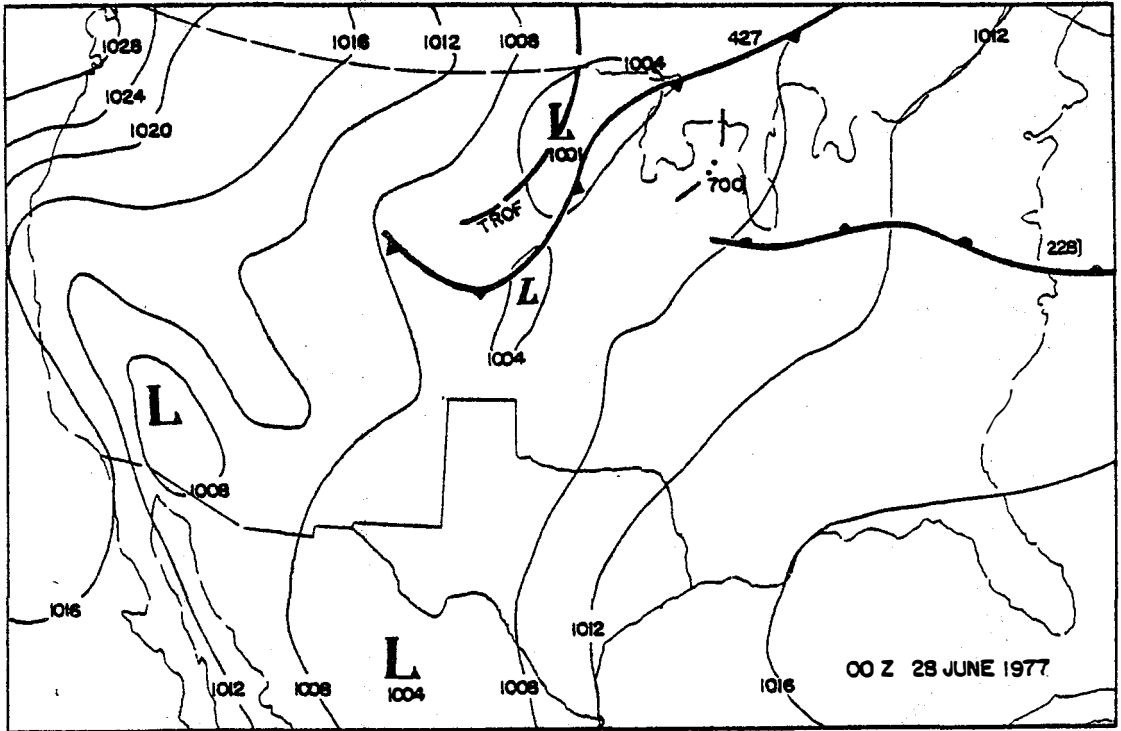
(d)

Figure 4-32   Continued

in the north central United States as low pressure and a trough developed behind the cold front and an instability line appeared between the fronts (Figure 4-32d).

The 500-mb pattern at 1200 GMT 27 June showed the 5880 gpm contour passing through Texas as the air flow into the study area occurred along this contour (Figure 4-33a). There was a weak trough through central Texas at 1200 GMT which moved slowly eastward by 0000 GMT 28 June (Figure 4-33b). A warm region of -5 C temperature remained stationary west of the Mexican coast throughout the day. No significant synoptic features occurred within the study area during this day.

4.4.2 Subsynoptic Features

4.4.2.1 Discussion of Midland Radar Displays and Satellite Imagery

The Midland WSR-57 radar observed a precipitation echo which increased in size although it overlapped with the ground clutter after 2015 GMT (Figure 4-34). The echoes were located in the southwestern portion of the study area, just reaching the southwest corner of the raingage network. Both the visible and infrared ADVISAR images showed that the thunderstorm cell migrated into the study area (Figure 4-35), confirming the WSR-57 radar observations. The satellite and radar displays further showed that the main cell of the thunderstorm did not
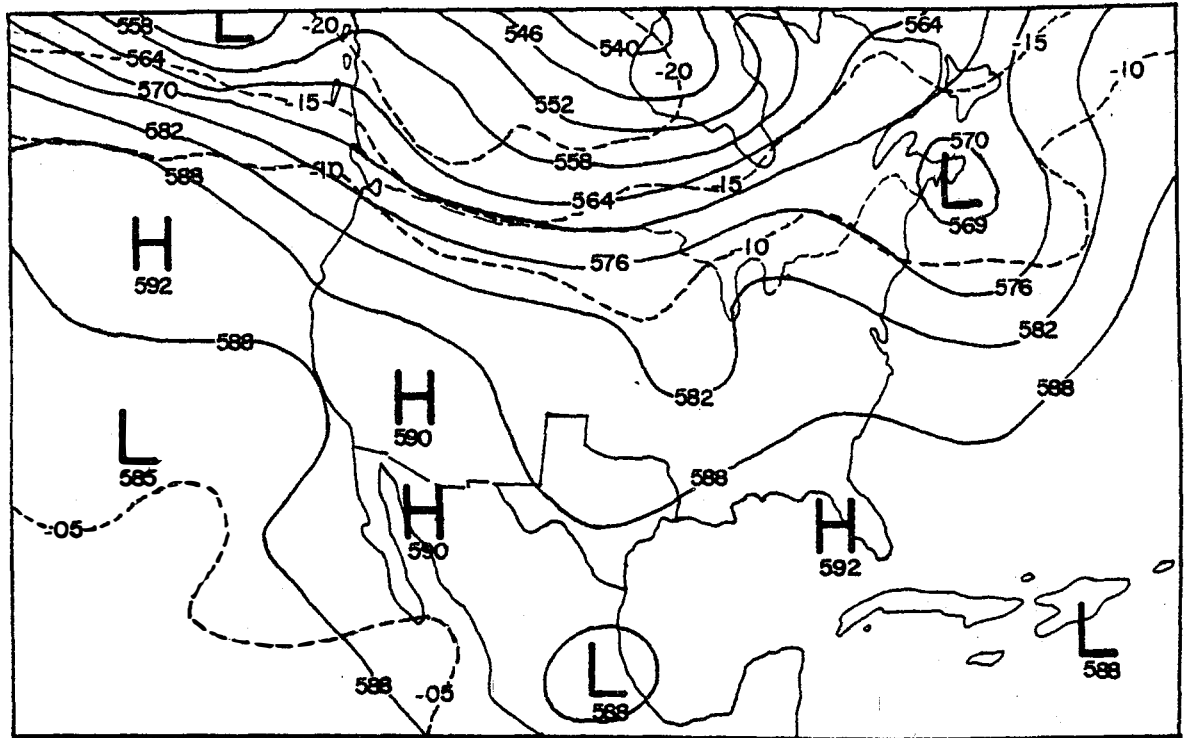
(a) 500mb 12Z 27 JUNE 1977
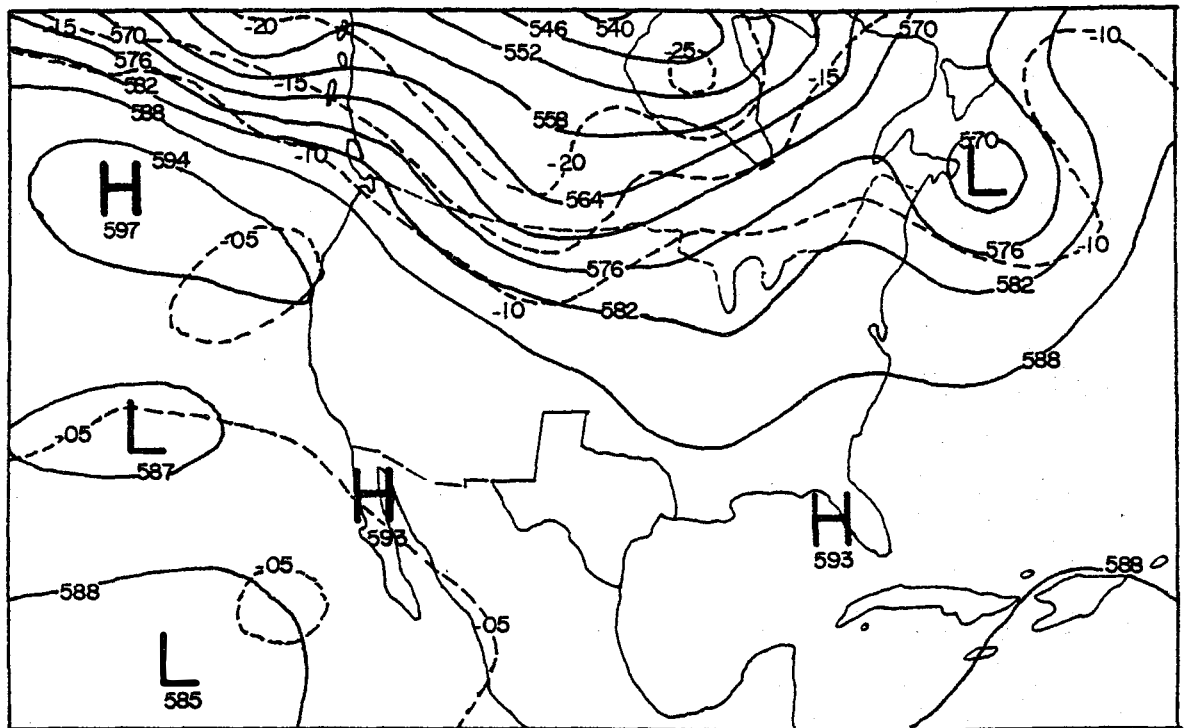
(b) 500 mb OOZ 28 JUNE 1977

Figure 4-33 500-mb charts on 27 June 1977. Codes
are the same as Figure 4-2.
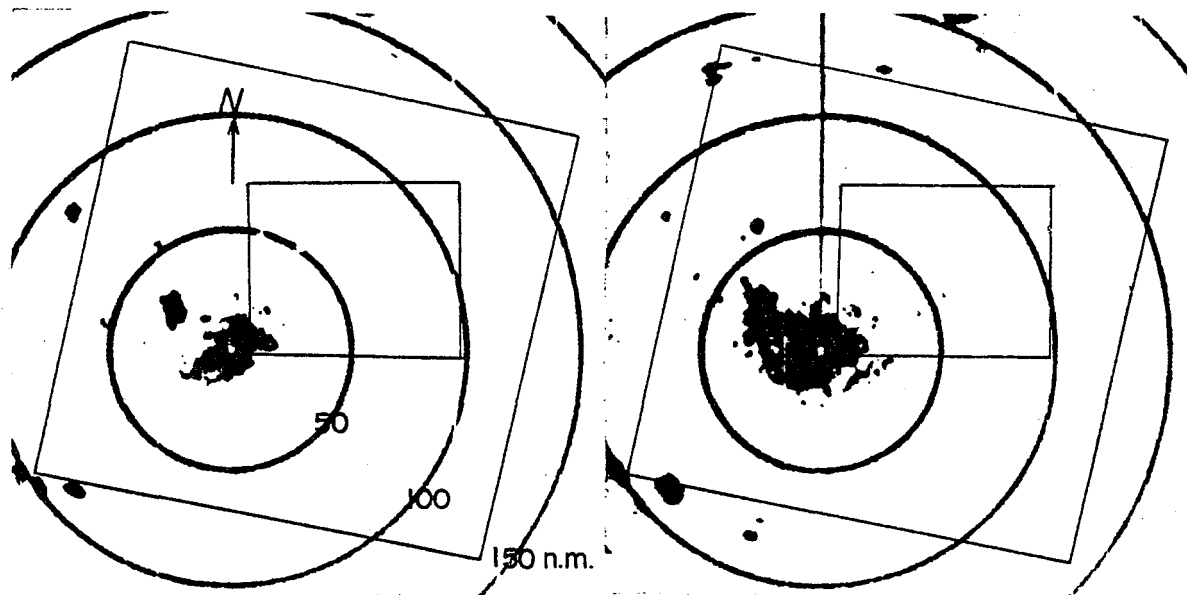
(a) 2045 GMT

(b) 2115 GMT
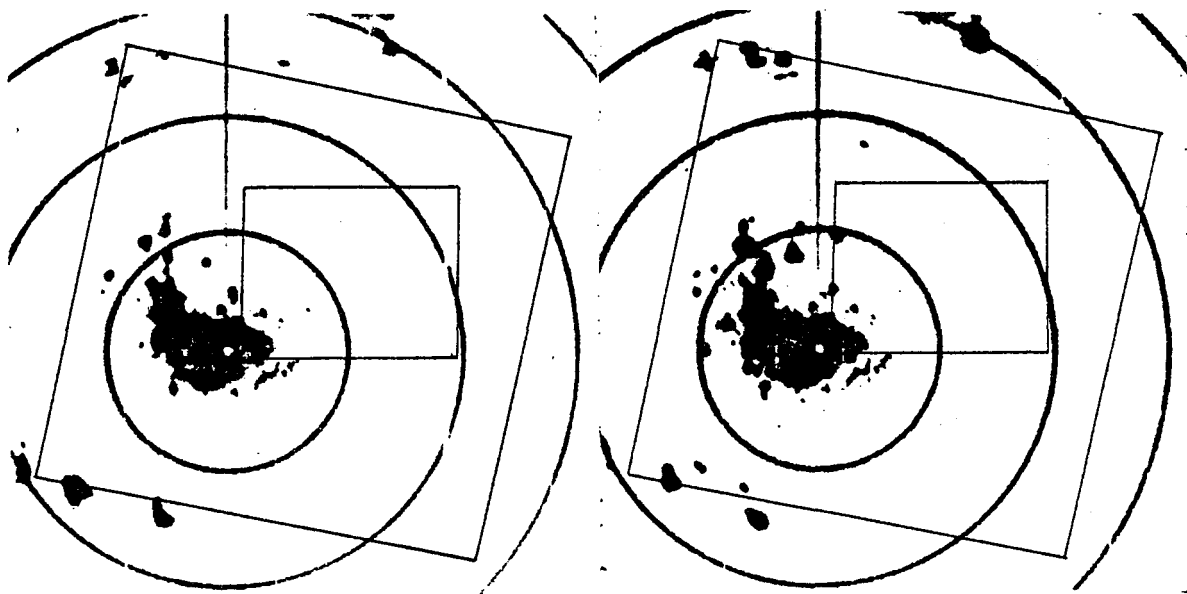
(C) 2145 GMT

(d) 2215 GMT

Figure 4-34   PPI displays on 27 June 1977 from the
National Weather Service radar at Midland.
The boundaries are the same as Figure 4-23.
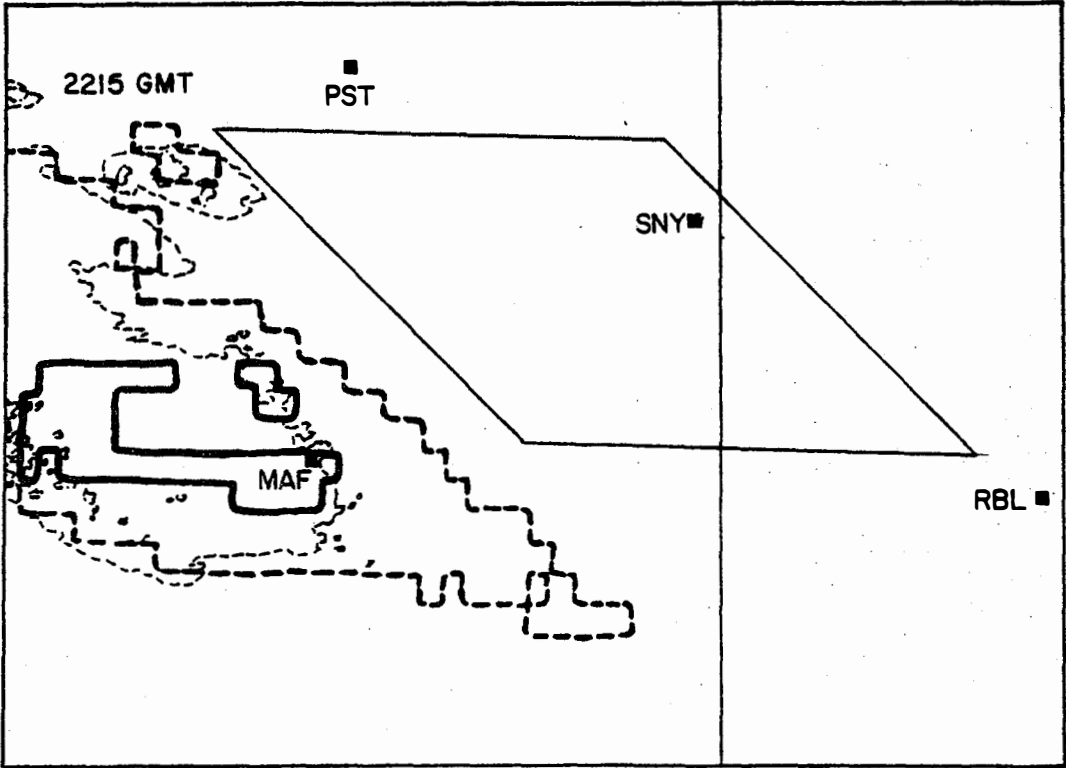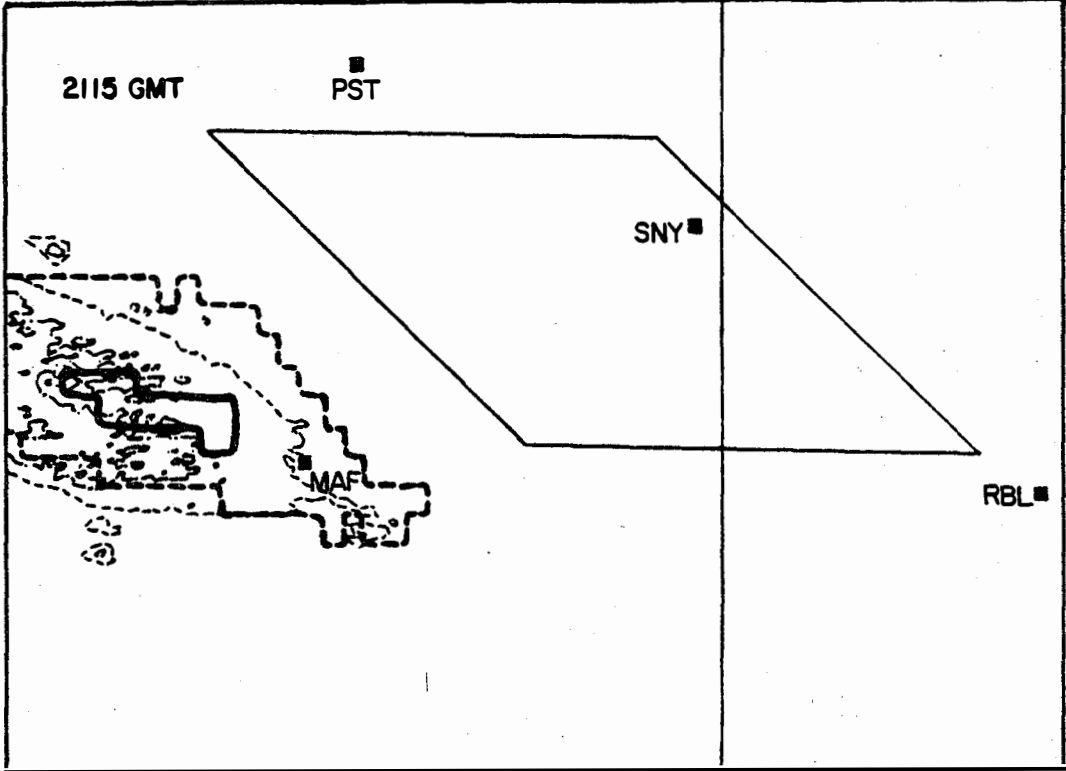
Figure 4-35   Cloud albedo and cloud top temperatures at
               2115 and 2215 GMT on 27 June 1977. The
               explanatory code is given in Figure 4-6.

reach the raingage network during the 27 June study period. The deep vertical development of this thunderstorm was identified by sharp gradients of cloud brightness and cloud top temperature (height) (see Figure 3-10). It is possible that heavy rain may have occurred beneath the core of the bright storm cell with high cloud tops, but no raingage data were available for confirmation.

4.4.2.2 Mesonetwork Observations

Surface temperature fields observed by the mesonetwork indicated the influence of the convective activity in the northwest part of the study area on the development of a minimum temperature region after 2100 GMT on this day (Scoggins, et al., 1979). Also, the patterns of horizontal mass divergence showed persistent divergence at mid levels throughout this period and areas of slight surface divergence occurred in the vicinity of the observed radar echoes.

4.4.3 Small-scale Features
4.4.3.1 Review of Soundings

The dry conditions on 27 June are obvious from Figure 4-36 and indicate a situation similar to that on 24 June. There was a strong temperature inversion near the surface with dry conditions above at 1500 GMT on the morning of 27 June. The temperature inversion weakened
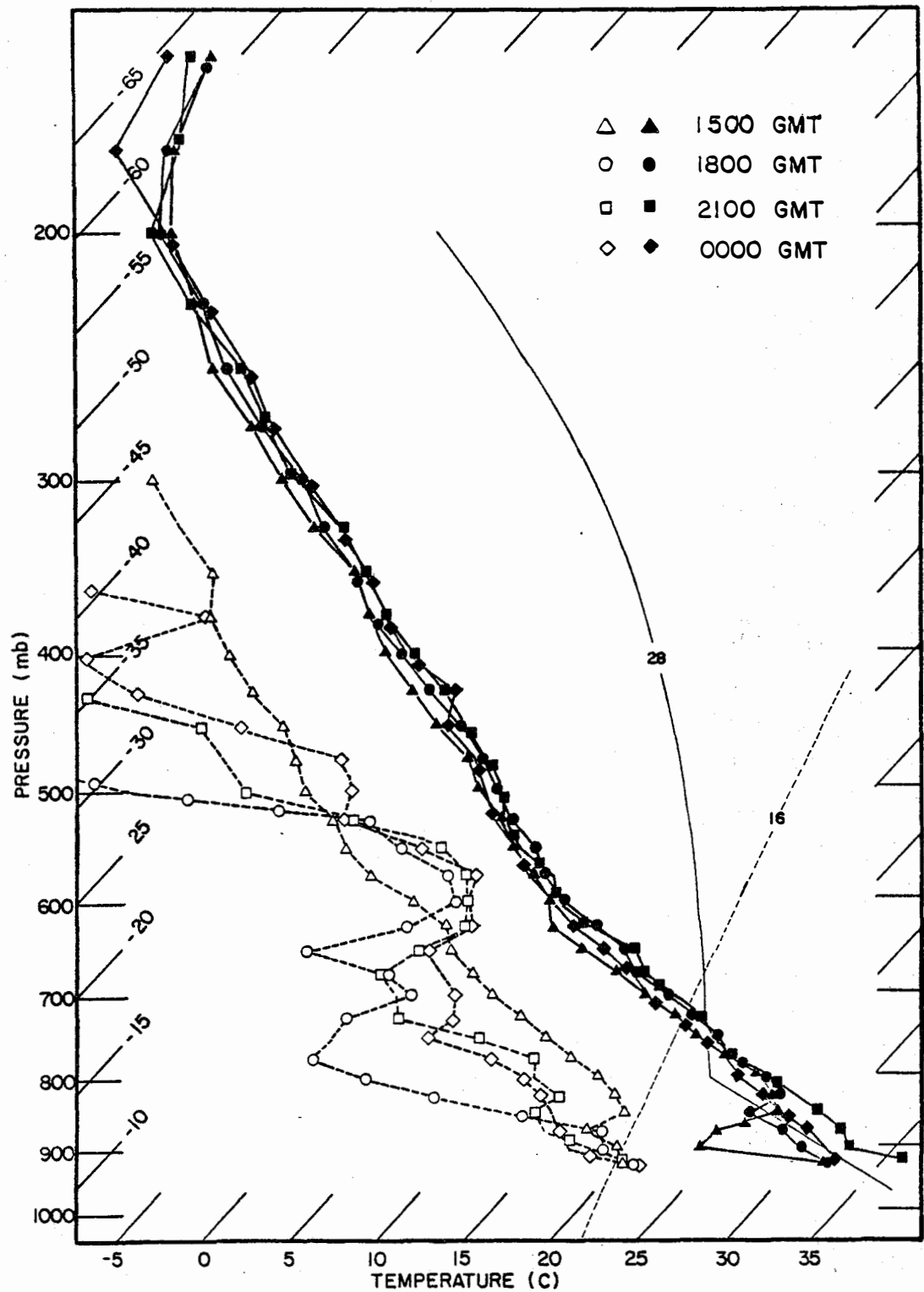
Figure 4-36   Atmospheric soundings taken at Big Spring
on 27 June 1977.   Codes are the same as
Figure 4-17.

by 1800 GMT and had disappeared at 2100 GMT as the
temperature of the surface and lower layers rose. The
temperatures above 850 mb did not vary significantly with
time and the LCL remained near 800 mb throughout the day.
A lifting of approximately 70 mb above the LCL was
required for free convection to occur throughout this
day.

4.4.3.2 K-index and Precipitable Water Values

The K-indices, corresponding thunderstorm probabili-
ties and precipitable water calculated from the sounding
data are listed in Table 4-5. The values of the K-index
were again quite high, averaging 35 for all observations
on this day. The K-index at Midland increased
significantly when the thunderstorm moved into the study
area from the west after 2015 GMT. Precipitable water
totals derived from the soundings were lower on this
day than any of the preceding case study days, averaging
3.14 cm. It is noteworthy that the average value
calculated at Robert Lee, in the eastern portion of the
study area, was much less than those at the other stations,
and that the values at Midland increased with the
thunderstorm development over that portion of the study
area.

Table 4-5

K-indices, suggested thunderstorm probabilities
and precipitable water on 27 June 1977.

Time (GMT)	Midland		Post		Robert Lee		Big Spring	
	K-index	Prob.(%)	K-index	Prob.(%)	K-index	Prob.(%)	K-index	Prob.(%)
1500	28	40-60	36	80-90	33	60-80	43	~100
1800	32	60-80	36	80-90	-	-	-	-
2100	41	~100	40	80-90	-	-	32	60-80
0000	40	80-90	42	~100	28	40-60	37	80-90

	Precipitable Water (cm)	Precipitable Water (cm)	Precipitable Water (cm)	Precipitable Water (cm)
1500	2.62	3.18	2.73	3.68
1800	2.89	3.17	2.90*	3.66
2100	3.55	3.08	-	3.12
0000	3.32	3.24	2.90	3.13

* Surface to 625 mb only

4.4.4 Summary of 27 June 1977

There were no significant synoptic features near the study area on 27 June, as observed on surface and 500-mb charts. Both satellite and radar information showed that a thunderstorm entered the study area after 2045 GMT, but did not pass through the raingage network. The soundings were quite dry, similar to those on 24 June. Variation of the K-index and precipitable water with time reflected the thunderstorm activity inside the study area near Midland, where the storm cell passed after 2045 GMT. The average precipitable water, 3.14 cm, on this day was the smallest one among four case study days.

4.5 Comparison of the Case Study Days

Reviewing all the information derived from satellite, radar and raingage data, the results derived from the several observational systems were found to correlate closely on the four case study days. The rainfall areas, especially those with heavy intensities, occurred under the brightest and highest clouds. Usually, the rainfall area was located under clouds with albedo greater than 0.44 and cloud tops higher than 10 km, as derived form the satellite data. In a case study on 25 May 1976 at Miles City, Montana, Reynolds and Smith (1979) concluded that rainfall did tend to occur under regions of higher albedos (greater than 0.65) and colder cloud tops (less

than -30 C, corresponding to about 9.5 km in this study).
There were no rain areas found under clouds with albedos
less than 0.24 on either 22 June or 8 July. Cumulonimbus
clouds are usually identified as heavy and dense clouds,
with considerable vertical extent, in the form of a
mountain or huge towers. In the satellite radiance data
those clouds which were widespread, with large albedo and
high cloud tops near the core, could be identified as
cumulonimbi. The late afternoon on 27 June was a good
example of this situation, when a storm cell entered the
study area from the west. Cumulonimbus clouds were also
present at 1915, 1945, 2015, 2115 and 2145 GMT on 22 June
as well as 1945 and 2015 GMT on 8 July. The cumulonimbi
contributed most of the cloud cover in these cases. Both
location and intensity of the rainfall changed following
the movement and size variation of the cumulonimbus
clouds on 22 June and 8 July.

Comparing the patterns of precipitation-intensity
variation on 22 June and 8 July, the mechanisms of
precipitation generation on these two rain days were
quite different. The synoptic situation on 8 July showed
that a cold front passed through the study area between
1500 and 1800 GMT, and then moved out of the study area
by late afternoon (Figure 4-1). It is clear that the
precipitation resulted from vertical motion caused by
frontal forcing on 8 July. The rain band structure

across the raingage network at 1915, 1945 and 2015 GMT on
8 July established that the line of convective clouds
associated with the front produced the rain on this day.
The rain band occurred underneath bright clouds, having
albedos greater than 0.63. This area of high albedo was
quite extensive over the frontal zone.

On 22 June, a low pressure center was located near
the Panhandle of Texas at 1500 GMT with a cold front
extending eastward from the low pressure region. By
1800 GMT the low pressure center had disappeared and the
front moved eastward far away from the study area before
the rain began in the late afternoon. The surface
analysis discussed in Section 4-2 indicated that a squall
line passed the study area during the afternoon on 22 June.
Convergence of horizontal mass and moisture occurred with
the passage of this line. In addition, the GOES imagery
revealed a line of convective activity moving through the
study area during the late afternoon 'on 22 June. Thus,
the precipitation on 22 June was associated with a
subsynoptic feature.

The satellite-derived cloud top heights were quite
uniform and cold over rain areas. The areas of high cloud
tops occurred above the high radar reflectivity region,
except for a few intense narrow convective radar echoes
which appeared to be averaged away by the low spatial
resolution of the infrared radiance data. Usually, the

satellite-derived cloud tops had shapes similar to the echo tops derived from radar, but were smooth. This smoothness also could be attributed to the spatial resolution of the infrared sensors. When a 3 C uncertainty in cloud top temperature was allowed, the satellite-derived cloud tops matched the radar echo tops better. '

The heaviest rain occurred under the most intense radar reflectivity, larger than 50 dBz, at 1942 and 2018 GMT 8 July. The Z-R relation used in this study permitted approximation of the rainfall intensity from radar reflectivities. The rain band structure associated with the fronts on 8 July was particularly noticeable on the digital PPI displays at 1915, 1942 and 2018 GMT, defining not only the rain area, but also locating the region of most intense precipitation.

The K-index indicated high probabilities of thunder- storm occurrence on all four case study days, although the raingage network recorded little rain on 24 June and almost no rain on 27 June. Thunderstorms did occur in the late afternoon on both 24 and 27 June, but the core of the storm cells did not enter the raingage network between 1800 and 2359 GMT on these days as they migrated into the study area.

The unstable soundings measured within the target area also offered strong indications for thunderstorm

occurrence on the four case study days. The large positive areas above the LCL indicated that cloudy skies should dominate the study area during the afternoon after surface temperature rose sharply. However, the very dry conditions on 24 and 27 June presented a substantial barrier to widespread convective activity. As a result, deep convective development did not occur within the study area on these two days. On both 22 June and 8 July, however, ample moisture was available and precipitation forcing mechanisms presented themselves. The passage of the mesoscale convective line on 22 June and of the synoptic scale cold fronts on 8 July led to significant precipitation events on the two days.

CHAPTER 5

SUMMARY AND CONCLUSIONS

The work described here is a set of case studies of cloud properties and precipitation phenomena in the High Plains of Texas. The primary objective of this study was to determine the cloud features using visible and infrared data from geostationary satellites, and to verify the results with radar reflectivity and precipitation patterns.

This research has been conducted to develop analysis techniques for Geostationary Operational Environmental Satellite (GOES) radiance data, while utilizing both digital radar data and raingage measurements for verification of the results. Forty four sets of simultaneous visible and infrared satellite data on 22 June, 24 June, 27 June and 8 July 1977 were selected for study. One of the principal results is the set of satellite-derived cloud properties, such as numbers of clouds in several size categories, brightness, albedo, cloud top temperature and their relation to the prevailing synoptic situation.

Comparing the satellite radiance data and photographic imagery, the agreement between derived percent cloud cover values was found to be better than the isolated and widespread cloud count results. This result is reasonable because percent cloud cover is an

146

integrated cloud parameter and should not be subject to as much variability as individual cloud counts. The agreement between either isolated or widespread cloud numbers as derived from the radiance data and according to the imagery was better in the middle or late afternoon than earlier. During the early afternoon hours, higher frequencies of isolated small clouds occurred, while in the later hours organization of the convection led to fewer clouds of larger sizes. Because the computer summary program treated small clouds as a single cloud as long as the individual clouds were linked together, at even a single point, the computer-based cloud counts were underestimated in the early afternoon. Overall, close agreement existed in the number of clouds and percent cloud cover derived from the two different forms of satellite data for the four case study days.

The percent cloud cover was found to be closely related to the weather events on these four case study days. Percent cloud cover was large and quite constant with time on 22 June and 8 July, especially during the rainfall periods. The small percent cloud cover observed before 2045 GMT on 24 June and 27 June increased as storms entered the study area late on these two days.

Synoptic, subsynoptic and small-scale features were utilized to follow the development of thunderstorm activity, as well as to offer evidence regarding the

mechanisms of precipitation formation during the several case study days. Convective clouds caused by the cold front, a synoptic feature, on 8 July and caused by the passage of a squall line, a mesoscale feature, on 22 June produced the observed significant precipitation. There were no significant features to cause rainfall inside the raingage network on 24 and 27 June, although thunderstorms did migrate into the study area in the late afternoon on both days.

The sequence of Figures 3-3 to 3-6 indicated that the distributions of cloud brightness values could be separated into two catagories. For the patterns on both 8 July and 22 June the brightness population modal values were located within the cloud region, especially during the period when heavy rain was occurring within the raingage network. In contrast, for the brightness distributions on 24 and 27 June the cloud brightness population modes were located in the non-cloud region; on these days little or no precipitation was measured. It appears that the distribution of visible radiance values may offer a means of identifying regions of precipitation directly from satellite measurements.

Two sources of verification for the satellite-derived results were raingage and radar measurements. The heavy rainfalls observed on 22 June and 8 July occurred under those high albedo and cold cloud top temperature areas of

the cloud systems present. The cloud top heights derived from infrared satellite radiance data and radar echo tops showed realistic correlations, except for those narrow high cells which were averaged out by the large spatial resolution of the infrared sensors. The comparisons made in this study demonstrate the consistency of results derived from satellite radiance measurements with analyses of radar and raingage data, thereby establishing the usefulness of satellite data in the absence of radar or raingage measurements.

A number of factors indicated that convective activity should be expected on each of the four case study days. The K-index of stability was large enough to predict the likely occurrence of thunderstorms each day. Precipitable water values revealed at least average moisture on all four days, although the 22 June and 8 July totals were noticeably higher. The temperature soundings appeared to possess sufficient potential instability to support convective development if it were initiated by low-level instability. The critical element was found to be a forcing mechanism for the precipitation process. In the absence of forcing, vigorous convective activity did not develop within the target area on 24 or 27 June, although some cumulonimbus did advect in.

Further studies are planned to develop objective methods of estimating rainfall from satellite visible and

infrared data. The estimated precipitation volumes could be verified by raingage measurements and digital radar reflectivity data. The rainfall volume estimated by satellite photographic imagery would also be helpful in comparison with those derived from the digital satellite radiance data. Once established, such a method could be applied to thunderstorms outside the raingage network to estimate rainfall volume. This is the long-term goal of the present study. With this development, it should be possible to extend the coverage of programs such as HIPLEX beyond the range of radar and raingage measurements.

The present study has demonstrated the reliability of satellite radiance data when compared with radar and raingage measurements. However, the problem of working with observations from three systems with such different spatial resolution was formidable. The superposition of patterns in this study was performed subjectively by hand. Techniques (Reynolds and Smith, 1979) which utilize an objective computer-based approach are becoming available and should permit more ambitious efforts in the future.

LIST OF REFERENCES

Alexander, W. O., 1979: Private Communication. Texas Dept. of Water Resources.

Charney, J., W. J. Quirk, S. H. Chow and J. Kornfield: A Comparative Study of the Effect of Albedo Change on Drought in Semi-Arid Regions. J. Atmos. Sci., 34, 1366-1385.

Dismachek, D. C., 1977: National Environmental Satellite Service Catalog of Products. NOAA Technical Memorandum NESS 88, U.S. Dept. of Commerce, Washington, D. C., 102 pp.

Gruber, A., 1973: Review of Satellite Measurements of Albedo and Outgoing Long-wave Radiation. NOAA Technical Memorandum NESS 48, U.S. Dept. of Commerce, Washington, D. C., 12pp.

Haragan, D. R., J. Jurica, and C. A. Leary, 1979: Texas HIPLEX Interim Progress Report, April 1 - September 30, 1979, TDWR Contract No. 14-90023. Texas Dept. of Water Resources Publication No. LP-110, 132 pp.

Jurica, G. M. and S. Y. Chi, 1979: Determination of Cloud Properties from Bispectral Satellite Measurements. Final Report TWDB Contract No. 14-80026. Texas Dept. of Water Resources Publication No. LP-92, 102 pp.

Leary, C. A. and R. A. Houze, Jr. 1979: The Structure and Evolution of Convection in a Tropical Cloud Cluster. J. Atmos. Sci., 36, 437-457.

List, R. L., 1966: Smithsonian Meteorological Tables. Sixth Revised Edition, Smithsonian Institution, 527 pp.

Mosher, F. R., 1974: SMS Cloud Height. Space Science and Engineering Center, University of Wisconsin, 25 pp.

Mulvey, G. J., 1978: Private Communication. Meteorology Research, Inc.

Ogura, Y. and M. T. Liou, 1979: The Structure of a Mid-latitude Squall Line: A Case Study. Submitted to the J. of Atmos. Sci.

Park, S. U., D. N. Sikdar, and V. E. Suomi, 1974: Correlation Between Cloud Thickness and Brightness Using Nimbus 4 THIR Data (11.5 μm Channel) and ATS 3 Digital Data. J. Appl. Meteor., 13, 402-410.

Reynolds, D. W. and K. R. Morris, 1978: Use of the ADVISAR in the Analysis of Digital Satellite Data for Operational Seed-no seed Decision Making. Preprints of Fourth Symposium of Meteorological Observations and Instrumentation, Denver, Colorado, pp 212-218.

_____ and T. H. Vonder Haar, 1977: A Bispectral Method for Cloud Parameter Determination. Mon. Wea. Rev., 105, 446-457.

_____ and E. A. Smith, 1979: Detailed Analysis of Composited Digital Radar and Satellite Data. Bull. Amer. Meteor. Soc., 60, 1024-1037.

Rogers, R. R., 1976: A Short Course in Cloud Physics. Pergamon Press. 227 pp.

Scofield, R. A., 1978: Using Satellite Imagery to Estimate Rainfall during the Johnstown Rainstorm, Conference on Flash Floods: Hydrometeorological Aspects, Los Angeles, Calif. pp 181-189.

Scoggins, J. R., 1977: Texas HIPLEX Mesoscale Experiment-Summer 1977 Data Tabulations. Final Report TWDB Contract No. 14-70030. Texas Dept. of Water Resources Publication No. LP-10.

_____, G. S. Wilson and S. F. Williams, 1979: Mesoscale Characteristics of the Texas HIPLEX Area during Summer 1977. Final Report TWDB Contract No. 14-80002. Texas Dept. of Water Resources Publication No. LP-99, 433 pp.

Smith, E. A., 1977: Private Communication, Dept. of Atmospheric Science, Colorado State University.

Smith, W. L., 1969: Statistical Estimation of the Atmosphere's Geopotential Height Distribution from Satellite Radiation Measurements, ESSA Technical Report NESS 48, U.S. Dept. of Commerce, Washington, D. C., 29 pp.

Vonder Haar, T. H., 1970: Application of Simultaneous
    Infrared Radiation Measurements and Cloud
    Photographs from Satellites. J. Appl. Meteor., 9,
    955-958.

Webb, W. L., 1975: Meteorological Satellite Application.
    U.S. Army Electronics Command, 235 pp.

Widger, W. K., 1966: Meteorological Satellites. Holt,
    Rinehart and Winston, Inc.

Zipser, E. J. 1977: Mesoscale and Convective-scale
    Downdrafts as Distinct Components of Squall-line
    Structure. Mon. Wea. Rev., 105, 1568-1589.